Gravitational Wave Studies: Detector Calibration and an All-Sky Search for Spinning Neutron Stars in Binary Systems

by

Evan A. Goetz

A dissertation submitted in partial fulfillment
of the requirements for the degree of
Doctor of Philosophy
(Physics)
in The University of Michigan
2010

Doctoral Committee:

Professor Keith Riles, Chair
Professor Fred C. Adams
Professor Timothy A. McKay
Professor Georg A. Raithel
Professor Kim A. Winick

ACKNOWLEDGEMENTS

This work would not have been possible without the exceptional support I received from my Ph.D. adviser, Prof. Keith Riles. Throughout my time spent working on various projects, Keith has given me a great deal of enthusiasm, thoughtful discussions, and has shown enormous patience as I have charted my path toward my degree. Without a doubt, is has been an absolute pleasure to work for and with Keith at the University of Michigan. I am exceedingly grateful to have spent the past 6 years with an adviser like Keith.

I wish to thank the scientists and staff at the LIGO Observatories for their support of my work over the many summers and two years in residence at the LIGO Hanford site. To summarize, I wish to thank Drs. Richard Gustafson, Keita Kawabe, Michael Landry, Greg Mendell, and Daniel Sigg for allowing me to work and learn from them about gravitational wave detectors and data analysis. Among the staff, Dave Barker, Doug Cook, and Richard McCarthy have provided much assistance whenever I was in need. A number of operators were most generous to not only assist me when needed, but also became good friends. Many thanks to Anamaria Effler, Justin Garofoli, Corey Gray, and Dan Hoak (from LIGO Livingston). The LIGO Calibration team, Prof. Gabriela Gonzalez, Dr. Brian O'Reilly, Dr. Kawabe, and Dr. Landry, have also most graciously supported my research endeavors. Most importantly though, Dr. Richard Savage Jr. at LIGO Hanford has gone out of his way to support my efforts to learn more about gravitational wave detectors, and I have found our work together on calibration efforts to be very insightful into the intricacies of detector operations.

While I was spending time at LIGO Hanford, Rick was like a second adviser, for which I am very grateful.

Writing a complicated new data analysis algorithm that tackles one of the most computationally challenging data analysis tasks in gravitational wave physics is no trivial task, and my efforts came to fruition only because I have stood on the shoulders of those that came before me. I am indebted to the assistance of the Continuous Wave LVC working group, especially the efforts of Drs. Vladimir Dergachev, Chris Messenger, and Reinhard Prix for their valuable contributions and guidance.

During my time as a graduate student, I would not have had the stamina to persevere through many of the daily stresses without my friends both here in Michigan and elsewhere. Berit Behnke, Alejandra Castro, Sarah Feldt, Jonathan and Colleen Kellogg, Jeff Kissel, Matt Largo, Ross and Kate O'Connell, Pinkesh Patel, Matt and Katy Pennington, Eva-Marie and Nick Prozkow, Casey Schnider-Mizell, Nic Smith, Kevin and Autumn Turner, and Kris Yirak are just a few of the many friends who have lent their support, shared many late-night homework sessions, had insightful conversations, or shared a few beers with me along the path toward earning my Ph.D.

Finally, I wish to thank my parents, Robert and Martha, who have always been there for me, even at a great distance living across the United States in Oregon. They have allowed me to follow my own path throughout my education, and gave me many opportunities to succeed. I am very happy they gave me support as I pursued music, sports, outdoor activities, and my education. Without their efforts, I certainly would not have had the many successes throughout my life.

TABLE OF CONTENTS

LIST OF FIGURES

Figure

LIST OF TABLES

Table

ABSTRACT

Gravitational Wave Studies: Detector Calibration and an All-Sky Search for Spinning Neutron Stars in Binary Systems

by

Evan A. Goetz

Chair: Keith Riles

The Laser Interferometer Gravitational wave Observatory (LIGO) Project has constructed three, kilometer-scale gravitational wave detectors in the United States. These detectors have achieved unprecedented levels of differential-length sensitivity in a quest to directly observe the spacetime oscillations produced by gravitational waves from astrophysical sources. These waves can provide new observations and insight into some of the most energetic, exotic, and violent events in the Universe.

Strain calibration of gravitational wave detectors is crucial for waveform reconstruction and source localization. Scientific reach is substantially improved if the calibration uncertainty can be reduced to the level of 1%. Toward this end, we have developed two fundamentally different precision test mass actuator calibration techniques to compare with the traditional calibration method, which measures a critical component of the key interferometer servo control loop that determines the gravitational wave output signal. We have compared our results from the three techniques in order to investigate systematic uncertainties associated with each technique.

A potential class of gravitational wave sources are rapidly spinning neutron stars with non-axisymmetric mass distributions, which generate quasi-monochromatic continuous gravitational waves. While search methods for unknown isolated spinning stars are approaching maturity, there have been no previous searches for unknown spinning stars in binary systems. Current search methods for isolated stars are already computationally limited; expanding the parameter space searched to include binary systems is a formidable challenge. We present a new hierarchical binary search method called TwoSpect, which exploits the periodic orbital modulations of the continuous waves by searching for patterns in doubly Fourier-transformed data. We will describe the TwoSpect search pipeline, including its mitigation of detector noise variations and corrections for Doppler frequency modulation caused by changing detector velocity. Tests on simulated data and on a sample of detector data will be presented.

CHAPTER I

Introduction

Gravitational waves are a consequence of the General Theory of Relativity or other alternative theories of gravity. The acceleration of massive, relativistic astrophysical objects, such as in black hole or neutron star collisions, or in supernova explosions, cause ripples in spacetime to radiate from the objects and propagate nearly unimpeded across the Universe. Gravitational radiation is different from electromagnetic radiation in that the waves are a consequence of the dynamic motion of the mass distribution of the source, and the quadrupolar nature of the waves tidally distorts spacetime. Physicists and astronomers have predicted the existence of gravitational waves from a variety of astrophysical objects with amplitudes that could be detectable on Earth. Direct measurement of these waves would enable additional tests of General Relativity, or other theories of Gravity, and the waves would provide a direct signal from the engines of some of the Universe's most violent events. At this point, gravitational waves have not yet been directly detected.

The signal produced in Earth-based gravitational wave detectors by radiating astrophysical sources will likely be exceedingly small. Sophisticated data analysis algorithms have been developed over the past decade in order to search for a variety of signals buried in the noise of these detectors. Ever more sophisticated algorithms are under development to search for particular types of sources.

Described here is a new data analysis algorithm designed to find quasi-monochromatic gravitational wave signals from unknown spinning neutron stars in binary systems. Gravitational waves from neutron stars are interesting in part because the waves from such a source give insight into the neutron star equation of state. Different types of neutron star emission mechanisms would produce different gravitational wave signals. Detection of a signal can constrain particular neutron star models. The exotic conditions of a neutron star–extreme gravity, super-dense matter, very high magnetic fields–are particularly hard to model, so a direct observation of the waves from a spinning neutron star should be illuminating. Neutron stars in binary systems are an attractive source because accretion of the companion star's matter onto the neutron star could help to drive gravitational wave emission.

To detect and study gravitational waves, physicists have constructed several kilometer-scale interferometers serving as gravitational wave detectors around the world. The initial goal of these detectors is discovery of gravitational waves, with a further goal to exploit this radiation for gravitational wave astronomy. Three multi-kilometer interferometers have been constructed in the United States by the Laser Interferometer Gravitational wave Observatory (LIGO) Laboratory: two detectors near Hanford, Washington, and a single detector near Livingston, Louisiana. A single, multi-kilometer detector has been constructed near Pisa, Italy by the Virgo Collaboration. Two sub-kilometer detectors have been constructed, one near Hannover, Germany (GEO600), and another near Tokyo, Japan (TAMA). These detectors make up a world-wide network of gravitational wave detectors.

To understand the interferometer response (i.e. the detector sensitivity) to impinging gravitational waves, the detector output must be calibrated against a known length change of the interferometer arms. Since these intricate devices operate in a closed-servo-loop configuration, the calibration must correct for the effect of the servo loop. Detector calibration is a complicated endeavor which requires multiple

measurements of the detector optical parameters and the electronics used for analysis of interferometer optical signals. Two new calibration methods will be presented and contrasted with the traditional less precise method to assess a significant component to the detector calibration uncertainty.

This work is organized as follows: Chapter II summarizes the derivation of the gravitational wave formula from the Einstein equations, the production of waves from accelerating masses, the different types of astrophysical sources of gravitational waves and, in particular, spinning neutron stars, and finally, the current analysis methods to find quasi-monochromatic gravitational wave signals in detector data. Chapter III discusses some of the technical aspects of the LIGO detectors. Chapter IV describes the frequency-domain calibration and three different methods for calibrating the LIGO test mass actuators–a key component to the overall calibration. In Chapters V and VI, the details of a new data analysis algorithm developed to detect spinning neutron stars in binary systems are described and validation of the pipeline on simulated and real LIGO data are presented.

CHAPTER II

Gravitational Waves from Spinning Neutron Stars

2.1 General relativity and gravitational waves

The formal theoretical description of gravitational waves was first proposed by Einstein with his development of the General Theory of Relativity. In this theory, matter and energy warp space, causing it to curve. The curvature is what objects feel when they feel the force of gravity. One result of the acceleration of mass (or energy) in this theory is analogous to a result of the acceleration of charges in electromagnetism– waves propagate away, carrying energy from the source.

Gravitational waves are a special solution of the Einstein field equations,

$$G_{\mu\nu} = \frac{8\pi G}{c^4} T_{\mu\nu} \,. \tag{2.1}$$

in the transverse gauge, where $G_{\mu\nu}$ is the Einstein curvature tensor, G is the gravitational constant, c is the speed of light and $T_{\mu\nu}$ is the stress-energy tensor. One can solve the Einstein field equations in the flat Minkowski metric, $\eta_{\mu\nu} = (-,+,+,+)$, plus a small gravitational wave perturbation, $h_{\mu\nu}$, such that

$$g_{\mu\nu} = \eta_{\mu\nu} + h_{\mu\nu} \tag{2.2}$$

with $|h_{\mu\nu}| \ll 1$. The inverse is given to first order by

$$g^{\mu\nu} = \eta^{\mu\nu} - h^{\mu\nu} \,. \tag{2.3}$$

The Einstein field equations can be computed using this flat metric plus a small perturbation. The equations are analyzed by taking the perturbations to first order in $h_{\mu\nu}$. The derivation of the wave equation from the Einstein field equations roughly follows [55]. The Christoffel symbol, defined as,

$$\Gamma^{\rho}_{\mu\nu} = \frac{1}{2} g^{\rho\sigma}(\partial_\mu g_{\sigma\nu} + \partial_\nu g_{\sigma\mu} - \partial_\sigma g_{\mu\nu}) \tag{2.4}$$

can be determined from the linearized metric to first order in $h_{\mu\nu}$:

$$\begin{aligned}
\Gamma^{\rho}_{\mu\nu} &= \frac{1}{2}(\eta^{\rho\sigma} - h^{\rho\sigma})[\partial_\mu(\eta_{\sigma\nu} + h_{\sigma\nu}) + \partial_\nu(\eta_{\sigma\mu} + h_{\sigma\mu}) - \partial_\sigma(\eta_{\mu\nu} + h_{\mu\nu})] \\
&= \frac{1}{2}(\eta^{\rho\sigma} - h^{\rho\sigma})(\partial_\mu h_{\sigma\nu} + \partial_\nu h_{\sigma\mu} - \partial_\sigma h_{\mu\nu}) \\
&= \frac{1}{2}(\partial_\mu h^{\rho}_{\nu} + \partial_\nu h^{\rho}_{\mu} - \partial^\rho h_{\mu\nu}) + \cdots \,.
\end{aligned} \tag{2.5}$$

The dots $(\cdots)$ indicate terms higher than linear order in $h_{\mu\nu}$ that have been neglected since we have specifically assumed that $h_{\mu\nu}$ is small.

The Riemann tensor is defined as

$$R^{\mu}_{\nu\rho\sigma} = \partial_\rho \Gamma^{\mu}_{\nu\sigma} - \partial_\sigma \Gamma^{\mu}_{\nu\rho} + \Gamma^{\mu}_{\alpha\rho}\Gamma^{\alpha}_{\nu\sigma} - \Gamma^{\mu}_{\alpha\sigma}\Gamma^{\alpha}_{\nu\rho} \tag{2.6}$$

which leads to the Ricci tensor,

$$R_{\mu\nu} = R^{\alpha}_{\mu\alpha\nu} \tag{2.7}$$

$$\begin{aligned} &= \partial_\alpha \Gamma^\alpha_{\mu\nu} - \partial_\nu \Gamma^\alpha_{\mu\alpha} + \Gamma^\alpha_{\beta\alpha}\Gamma^\beta_{\mu\nu} - \Gamma^\alpha_{\beta\nu}\Gamma^\beta_{\mu\alpha} \\ &= \frac{1}{2}\partial_\alpha(\partial_\mu h^\alpha_\nu + \partial_\nu h^\alpha_\mu - \partial^\alpha h^{\mu\nu}) - \frac{1}{2}\partial_\nu(\partial_\mu h^\alpha_\alpha + \partial_\alpha h^\alpha_\mu - \partial^\alpha h_{\mu\alpha}) + \cdots \\ &= \frac{1}{2}(\partial_\mu \partial^\alpha h_{\nu\alpha} + \partial_\nu \partial^\alpha h_{\mu\alpha} - \Box h_{\mu\nu} - \partial_\mu \partial_\nu h) + \cdots \end{aligned} \tag{2.8}$$

where $\partial_\alpha h^\alpha_\mu = \partial^\alpha h_{\mu\alpha}$, $h \equiv \eta^{\mu\nu} h_{\mu\nu}$, and the d'Alembertian operator is defined as

$$\Box \equiv \partial_\alpha \partial^\alpha = -(1/c^2)\partial_t^2 + \partial_x^2 + \partial_y^2 + \partial_z^2 \,. \tag{2.9}$$

As before, terms higher than first order in $h_{\mu\nu}$ have been neglected.

The Ricci scalar is given by

$$R \equiv g^{\mu\nu} R_{\mu\nu} \tag{2.10}$$

$$\begin{aligned} &= \frac{1}{2}(\eta^{\mu\nu} - h^{\mu\nu})(\partial_\alpha \partial_\mu h^\alpha_\nu + \partial^\alpha \partial_\nu h_{\mu\alpha} - \Box h_{\mu\nu} - \partial_\mu \partial_\nu h^\alpha_\alpha) \\ &= \partial^\nu \partial^\alpha h_{\nu\alpha} - \Box h + \cdots \,. \end{aligned} \tag{2.11}$$

Henceforth, because every equation is evaluated to first order in $h_{\mu\nu}$, the dots which indicate higher order terms will not be appended to the end of equations.

Equations (2.8) and (2.11) are inserted into the Einstein field equations, $G_{\mu\nu} = R_{\mu\nu} - \frac{1}{2} g_{\mu\nu} R$, yielding

$$G_{\mu\nu} = \frac{1}{2}[\partial_\mu \partial^\alpha h_{\nu\alpha} + \partial_\nu \partial^\alpha h_{\mu\alpha} - \Box(h_{\mu\nu} - \eta_{\mu\nu} h) - \partial_\mu \partial_\nu h - \eta_{\mu\nu} \partial^\rho \partial^\sigma h_{\rho\sigma}] \tag{2.12}$$

which can be compacted by defining

$$\bar{h}_{\mu\nu} \equiv h_{\mu\nu} - \frac{1}{2}\eta_{\mu\nu} h \,, \tag{2.13}$$

whose inversion is given by

$$h_{\mu\nu} = \bar{h}_{\mu\nu} - \frac{1}{2}\eta_{\mu\nu}\bar{h}\,. \tag{2.14}$$

Inserting equation (2.14) into equation (2.12),

$$\begin{aligned} G_{\mu\nu} = \frac{1}{2}[&\partial_\mu\partial^\alpha(\bar{h}_{\nu\alpha} - \frac{1}{2}\eta_{\nu\alpha}\bar{h}) + \partial_\nu\partial^\alpha(\bar{h}_{\mu\alpha} - \frac{1}{2}\eta_{\mu\alpha}\bar{h}) - \\ &\Box(\bar{h}_{\mu\nu} - \frac{1}{2}\eta_{\mu\nu}\bar{h} + \eta_{\mu\nu}\bar{h}) + \partial_\mu\partial_\nu\bar{h} - \eta_{\mu\nu}\partial^\rho\partial^\sigma(\bar{h}_{\rho\sigma} - \frac{1}{2}\eta_{\rho\sigma}\bar{h})] \\ = \frac{1}{2}[&\partial_\mu\partial^\alpha\bar{h}_{\nu\alpha} + \partial_\nu\partial^\alpha\bar{h}_{\mu\alpha} - \Box\bar{h}_{\mu\nu} - \eta_{\mu\nu}\partial^\rho\partial^\sigma\bar{h}_{\rho\sigma}]\,. \end{aligned} \tag{2.15}$$

With gauge freedom, we can choose the Lorentz gauge[1],

$$\partial^\nu\bar{h}_{\mu\nu} = 0\,, \tag{2.16}$$

which is analogous to the Lorentz gauge in electromagnetism, $\partial_\mu A^\mu$. With this condition, the linearization of the Einstein field equations reduces to a simple wave equation,

$$\Box\bar{h}_{\mu\nu} = -\frac{16\pi G}{c^4}T_{\mu\nu}\,. \tag{2.17}$$

This general formula can be set to zero because we wish to study the radiation away from the source. Therefore,

$$\Box\bar{h}_{\mu\nu} = 0\,. \tag{2.18}$$

The Lorentz gauge condition of equation (2.16) does not completely fix the gauge of $\bar{h}_{\mu\nu}$. The transverse-traceless gauge, or TT gauge, is now used to fix the gauge completely with the conditions,

$$\bar{h}_{\mu\nu} = h_{\mu\nu}\,, \qquad h^{0\mu} = 0\,, \qquad h^a_a = 0\,, \qquad \partial^b h_{ab} = 0\,. \tag{2.19}$$

[1]In an interesting bit of history, the "Lorentz gauge" was first used by *L. V. Lorenz* in 1867. This mis-naming has entered into broad usage, so this work will conform to this nomenclature.

Using the TT gauge conditions and equation (2.18), plane wave solutions can be obtained in the form

$$h_{\mu\nu}^{\mathrm{TT}} = e_{ab} e^{ik_\sigma x^\sigma} \,, \tag{2.20}$$

where e_{ab} is the polarization tensor, a constant, symmetric (0,2), traceless, purely spatial tensor that describes the amplitudes of the two polarizations of the wave; k^σ is the wave vector $(\omega/c, k^1, k^2, k^3)$. By choosing the wave to propagate along the z-axis, $k^\sigma = (\omega/c, 0, 0, k^3) = (\omega/c, 0, 0, \omega/c)$, one can write the solution in the form,

$$h_{\mu\nu}^{\mathrm{TT}} = \begin{pmatrix} 0 & 0 & 0 & 0 \\ 0 & h_+ & h_\times & 0 \\ 0 & h_\times & -h_+ & 0 \\ 0 & 0 & 0 & 0 \end{pmatrix} . \tag{2.21}$$

Here, h_+ and $h_\times$ are the "plus" and "cross" polarization amplitudes of the wave in the TT gauge. In summary, by imposing the Lorentz gauge, the symmetric $h_{\mu\nu}$ tensor reduced from 10 degrees of freedom to 6 degrees of freedom, and by choosing the TT gauge–essentially a choice of the coordinate system–the number of degrees of freedom has been reduced from six to two, consistent with a purely transverse wave.

The gravitational wave strain amplitude of one of the polarizations, say h_+, is related to the amplitude of the varying distance between "freely-falling" test particles and, in the long-wavelength approximation with a wave traveling in the z-direction, can be written as,

$$h_+ = \frac{L_x - L_y}{L} = \frac{\Delta L}{L} \tag{2.22}$$

where L_x and L_y are the lengths of the test particle separation in orthogonal directions, and L is the average length (see figure 2.1). It will be shown in section 2.3 that the strongest expected amplitude of astrophysically-produced gravitational waves impinging on Earth-based detectors is $\lesssim 10^{-21}$. For a kilometer-scale detector to detect

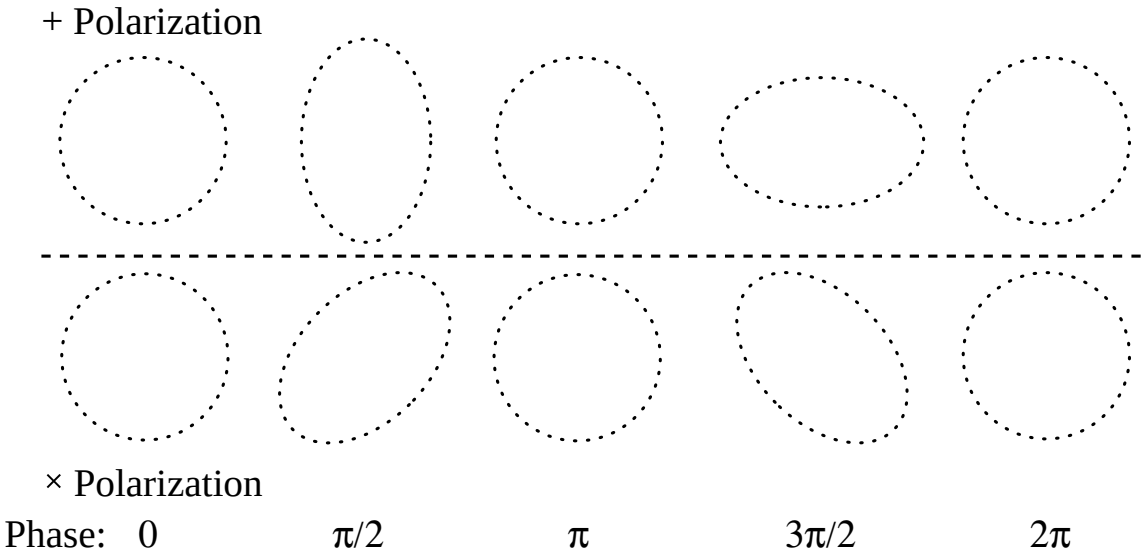

Figure 2.1: A ring of test particles appears to be stretched and compressed as a gravitational wave propagating in the z-direction, into or out of the plane of the page, stretches and compresses space-time. The two polarizations, h_+ and $h_\times$, are depicted in the upper and lower halves. Note the 45 degrees of rotation between the plus and cross polarizations.

gravitational waves directly, ΔL measured by the detector is thus $\lesssim 10^{-18}$ meters. Chapter III describes how such sensitive measurements are possible using the LIGO detectors.

2.2 Production of gravitational waves

Equation (2.17) has a solution that can be obtained by using a Green function, analogous to that in electromagnetism. The Green function, $G(x^\sigma - y^\sigma)$ for the d'Alembertian operator, $\Box$, is a solution to the wave equation in the presence of a 4-dimensional delta-function source [24],

$$\Box_x G(x^\sigma - y^\sigma) = \delta^{(4)}(x^\sigma - y^\sigma)\,, \tag{2.23}$$

where $\Box_x$ signifies the d'Alembertian operator acts on coordinates x^σ. Then, the Green's function can be used to find a solution to equation (2.17) with the form,

$$\bar{h}_{\mu\nu}(x^\sigma) = -\frac{16\pi G}{c^4}\int G(x^\sigma - y^\sigma)T_{\mu\nu}(y^\sigma)\, d^4y\,. \tag{2.24}$$

Similar to the case for electromagnetism [45], our interest is in the retarded Green's function with the form,

$$G(x^\sigma - y^\sigma) = -\frac{1}{4\pi|\mathbf{x}-\mathbf{y}|}\delta(|\mathbf{x}-\mathbf{y}| - (x^0 - y^0))\,, \tag{2.25}$$

where bold-faced variables indicate the spatial vectors with indices (1,2,3). Then, equation (2.25) can be inserted into equation (2.24) and integrated over y^0 to find,

$$\bar{h}_{\mu\nu}(x^\sigma) = \frac{4G}{c^4}\int \frac{1}{|\mathbf{x}-\mathbf{y}|}T_{\mu\nu}\left(t - \frac{|\mathbf{x}-\mathbf{y}|}{c}, \mathbf{y}\right) d^3y\,. \tag{2.26}$$

It proves useful to take Fourier transformations of equation (2.26) and make the approximations that the source is located far away from the observer, that the distribution of the stress-energy tensor of the source is small compared with the distance to the source, and that the source is slowly moving (i.e. the light travel time across the source is much faster than the motion of the source). This reduces equation (2.26) to [24]

$$\widetilde{\bar{h}}_{\mu\nu}(\omega, \mathbf{x}) = \frac{4G}{c^4}\frac{e^{i\omega r}}{r}\int \widetilde{T}_{\mu\nu}(\omega, \mathbf{y})\, d^3y \tag{2.27}$$

where the tilde denotes a Fourier transform and r is the distance to the center of the source. Since the Lorentz gauge has been imposed, the space-like terms are the terms of interest since the time-like terms can be computed from $\widetilde{\bar{h}}^{0\nu} = i\partial_a\widetilde{\bar{h}}^{a\nu}/\omega$, which is simply a restatement of the Lorentz gauge in the Fourier domain. We use the sub- or superscript indices a and b to denote the spatial terms (1,2,3). Thus, using the

Fourier transform and the approximations stated above,

$$\bar{h}_{ab}(t, \mathbf{x}) = \frac{2G}{rc^4} \frac{\partial^2}{\partial t^2} I_{ab}(t - r/c) \tag{2.28}$$

where I_{ab} is the quadrupole moment tensor of the energy density of the source. This is defined by

$$I_{ab} \equiv \int \rho(t, \mathbf{x}) \left(x_a x_b - \frac{1}{3} r^2 \delta_{ab} \right) d^3x \,. \tag{2.29}$$

It should be noted that these approximations enabled the derivation of the leading order contribution to gravitational radiation. Lower order terms, for instance, the monopole moment and dipole moments, are forbidden by conservation of energy and conservation of linear and angular momentum. Thus, the leading order term in gravitational radiation is a time-varying quadrupole moment of inertia, and higher-order terms are diminished by factors of c^{-1}. These higher-order terms are usually neglected when considering the emitted gravitational waves from simple models of radiating sources. In electromagnetism, there is no conservation law forbidding a time varying dipole moment of charge distribution, so to first order, electromagnetic waves are typically produced from the dipole moment.

2.3 Astrophysical sources of gravitational waves

Gravitational radiation is inherently weak due to the tiny coupling of gravity to matter, or, stated alternatively, space-time is extremely rigid. To generate detectable amplitudes of gravitational waves in the frequency band of Earth-based detectors, large, compact masses must be rapidly accelerating. Massive bodies in the Universe, such as black holes, neutron stars, or massive stars undergoing supernova explosion, are natural generators of strong gravitational radiation. It is hoped that with the next generation of gravitational wave detectors coming on-line in a few years, physicists will directly detect these waves. Direct observations and waveform measurements

will allow: new tests of General Relativity; insight into the engines that drive some of the Universe's most violent and energetic astrophysical events; population studies as larger numbers of sources are detected; improved understanding of super-dense matter such as that inside neutron stars; and perhaps discovery of entirely unexpected phenomena.

In 1973, Russell Hulse and Joseph Taylor discovered the binary pulsar PSR 1913+16. Observations over subsequent decades revealed that the orbital period of the two neutron stars was slowly decreasing at the rate predicted by Einstein's General Relativity [79] due to gravitational radiation. By observing the energy loss of the binary system, it provides indirect evidence for gravitational waves. Hulse and Taylor were awarded the Nobel Prize in Physics for their work in 1993. In roughly 300 million years, the orbit of PSR 1913+16 will decrease to the point where the system coalesces into a single compact object. To date, nine more double neutron star systems have been discovered, and five of the total will result in a merger within the age of the Universe due to the energy lost by gravitational wave emission [53].

As the gravitational waves carry energy away, the orbit of the binary system continues to decay and the gravitational wave amplitude increases, further carrying away more energy. The result is a "chirp" waveform, increasing in frequency and amplitude as a function of time. The instantaneous amplitude of the waves at an earth-based detector is [55]

$$h_0 \simeq 2 \times 10^{-21} \left(\frac{f}{1\,\mathrm{kHz}}\right) \left(\frac{r}{10\,\mathrm{Mpc}}\right)^{-1} \left(\frac{m_1}{1.4M_\odot}\right) \left(\frac{m_2}{1.4M_\odot}\right) \left(\frac{M}{2.8M_\odot}\right)^{-1/3} \quad (2.30)$$

where f is the gravitational wave frequency (twice the binary orbital frequency), r is the distance to the source, m_1 and m_2 are the masses of the compact objects in the binary, and M is the total mass of the binary system. The gravitational wave frequency, f, has a maximum value which is dependent on the masses of the

compact objects in the binary system. For a pair of neutron stars, the maximum gravitational wave frequency is $f_{max} \sim 1$ kHz while for a pair of $\sim$3 stellar mass black holes $f_{max} \sim 100$ Hz. At this point, no coalescing sources have been detected [14], largely because the rate of coalescing binaries is small ($\sim$100 Myr^{-1} per Milky Way Equivalent Galaxy, although plausible estimates range from 1 Myr^{-1} MWEG^{-1} to 1000 Myr^{-1} MWEG^{-1}). The most recent estimates give a range of 2×10^{-4} to 0.2 detectable events per year for the initial LIGO-Virgo interferometers, with 0.02 events per year the most likely rate. In advanced detectors, the most likely detectable event rate is 40 per year [2]. The increase in detectable event rate is due to an increased volume of the Universe able to be sampled by the detector by lower noise levels in advanced interferometers.

Compact objects in coalescing binary systems provide merely one type of gravitational wave signal which might be observed by ground-based gravitational wave detectors. Waveforms of gravitational radiation can be roughly divided into four classes: sources with a well-modeled, short-lived signal like a coalescing binary system whose signal lasts a few seconds in the detector; an unmodeled, short-lived signal, a so-called "burst" of gravitational waves like that from a supernova explosion which would emit a brief burst of waves; a well-modeled, long-lived signal such as a spinning neutron star whose nearly sinusoidal continuous signal may last for many years; and an unmodeled, long-lived signal such as a generic stochastic background of gravitational waves which may be continuously present in the detector.

Gravitational waves from bursting sources can be caused by supernovae, gamma-ray bursts (GRBs), flares from soft gamma-ray repeaters (SGRs), or other short, extremely energetic events. Unlike the inspiral class of sources, there is no indirect evidence for gravitational wave emission from this type of source. However, given the violent nature of these events, large asymmetries are likely, leading to a time-varying quadrupole moment of inertia. Although the waveform is unknown, the amount of

energy contained in the radiation can be quantified by, h_{rss}, the root-sum-square of the gravitational wave strain in both polarizations over an interval of time. Recent "blind" searches have determined the h_{rss} sensitivity of initial detectors to simulated waveforms is $6 \times 10^{-22}\,\mathrm{Hz}^{-1/2}$ to $2 \times 10^{-20}\,\mathrm{Hz}^{-1/2}$, and a prediction of less than 2.0 events per year with a confidence of 90% [1].

Spinning compact objects can produce quasi-monochromatic gravitational waves if they are non-axisymmetric about the spin axis. The archetypical source for these waves are neutron stars. Rotational energy of the star is lost due to gravitational (and electromagnetic) emission. Thus, the instantaneous sinusoidal signal from an isolated star will decrease in frequency over long timescales. The expected amplitude of gravitational waves generated by such deformations is very small (see section 2.4). Fortunately, since these sources produce long-duration waves of nearly stable frequency, one can, in principle, observe the source for a long time ($\sim$1 year) to build up the signal from the noise floor of the instrument. For example, a two-year observation of the Crab pulsar using the LIGO detectors has found the spindown loss due to gravitational radiation to be less than 2% of the total energy loss ($\approx 4.4 \times 10^{31}$ W using $\nu = 29.78$ Hz and the principal moment of rotational inertia $10^{38}\,\mathrm{kg\,m^2}$) which corresponds to an upper limit of the gravitational waves emitted by the Crab pulsar to be less than 1.9×10^{-25} with 95% confidence [15].

Finally, the stochastic class of gravitational waves refers to uncorrelated, random sources. Stochastic sources can be galactic or cosmological. Galactic sources could include signals from the numerous white-dwarf binaries in our galaxy. Cosmological sources could include vast populations of collapsed black holes, cosmic strings, or even sources from the inflationary period of our universe's origin. It is thought that a fraction of the total energy density of the universe is due to gravitational wave energy. Recent measurements from correlating the outputs of the LIGO detectors have placed upper limits on gravitational wave contributions to the total energy density to be less

than 6.9×10^{-6} in a frequency band around 100 Hz, beating indirect limits from Big Bang nucleosynthesis and cosmic microwave background [27]. This upper limit is $\sim$8 orders of magnitude higher than plausible inflationary models predict for a cosmological gravitational wave background.

2.4 Gravitational waves from spinning neutron stars

Gravitational wave emission mechanisms from neutron stars, or other exotic compact objects, can provide insight into the nature of the extremely dense, ultra-high magnetic field nuclear matter. While the structure of exotic matter (e.g. quark matter) compact objects may be considerably different from the neutron star "standard-model," which is primarily neutron-rich matter, the term *neutron star* will be used to describe any compact object in this class of sources. Characterizing the emission strength and dynamics of continuous gravitational waves probes the structure of neutron stars. Additionally, all-sky surveys can be used to place constraints on population models and birth rates of neutron stars.

There are at least three emission processes of continuous gravitational waves from neutron stars with frequencies in the LIGO frequency band: 1) non-axisymmetric distortions of the solid part of the star, 2) r-mode oscillations of the fluid part of the star, and 3) free precession of the entire star [6, 21]. There are many different physical mechanisms which may produce asymmetries in the neutron star moment of inertia (see e.g. [64] for a recent review). Accretion onto a neutron star in a binary system is a natural way to produce an asymmetry of the moment of inertia. The asymmetry of the neutron star may remain for a long time even if the accretion flow shuts off [21].

The distortions that break a neutron star's axial spin symmetry are sometimes referred to as "mountains," and could be supported by the neutron star crust, or magnetic fields [21]. When a non-axisymmetric neutron star rotates about one of its principal moment of inertia axes, for the sake of argument the I_{zz} axis, with spin

frequency ν, the gravitational wave amplitude, h_0, emitted due to the time-varying quadrupole moment of inertia is [6, 8, 55]

$$h_0 = \frac{4\pi^2 G}{c^4}\frac{\epsilon I_{zz} f^2}{r}\,, \tag{2.31}$$

where the frequency of the gravitational waves is $f = 2\nu$ and the dimensionless ellipticity parameter, ϵ, is defined by the three principal moments of inertia,

$$\epsilon \equiv \frac{I_{xx} - I_{yy}}{I_{zz}}\,. \tag{2.32}$$

The propagating waves carry the two wave polarizations, h_+ and $h_\times$, as described in section 2.1. An observer whose line-of-sight makes an angle ι with the spin axis of the star will observe the gravitational waves with polarization amplitudes

$$h_+ = h_0\frac{1+\cos^2\iota}{2} \tag{2.33}$$

$$h_\times = h_0\cos\iota\,. \tag{2.34}$$

The ellipticity of a neutron star is dependent on the structure and makeup of the star, its magnetic field, or accretion from a companion star. Recent simulations of dense nuclear matter in neutron stars [43] indicate that an upper bound for normal nuclear matter of the star's crust would yield a breaking strain $\sigma_{max} \simeq 0.1$. The maximum ellipticity of a normal neutron star is related to the breaking strain by [63]

$$\epsilon \leq 3.4\times10^{-7}\left(\frac{\sigma_{max}}{0.01}\right)\left(\frac{M_{NS}}{1.4M_\odot}\right)^{-2.2}\left(\frac{R}{10\,\mathrm{km}}\right)^{4.26}\left[1+0.7\left(\frac{M_{NS}}{1.4M_\odot}\right)\left(\frac{10\,\mathrm{km}}{R}\right)\right]^{-1} \tag{2.35}$$

where M_{NS} is the neutron star mass and R is the neutron star radius. Thus, the maximum ellipticity of a canonical neutron star could be as high as $\epsilon \lesssim 2\times10^{-6}$.

Using the maximum ellipticity value, the amplitude of the gravitational waves

impinging on a earth-based detector from a galactic neutron star is estimated to be,

$$h_0 \lesssim 2 \times 10^{-24} \left(\frac{\epsilon}{2 \times 10^{-6}}\right) \left(\frac{I_{zz}}{10^{38}\,\mathrm{kg \cdot m^2}}\right) \left(\frac{f}{1\,\mathrm{kHz}}\right)^2 \left(\frac{r}{1\,\mathrm{kpc}}\right)^{-1} . \qquad (2.36)$$

To detect waves with an amplitude of 4×10^{-24}, requires observations of a signal of the order of weeks to years in order to confidently observe a signal buried in the noise of a gravitational wave detector.

Recent models of the neutron star structure predict that the interior could be made of strange quarks or a hybrid of normal baryonic matter with some quark matter. These models predict the shear modulus of the material could support large ellipticities, perhaps several orders of magnitude larger than normal baryonic matter [63, 64].

If the spin axis of an isolated neutron star is not aligned with a principal axis of the moment of inertia, then the neutron star will freely precess about its spin axis. The precession causes the quadrupolar moment of inertia to vary with time as the star "wobbles." A large-amplitude wobble of a star with rotation rate ν would produce waves with strain amplitude a distance r from the source,

$$h_0 \sim 10^{-27} \left(\frac{\theta_w}{0.1}\right) \left(\frac{r}{1\,\mathrm{kpc}}\right)^{-1} \left(\frac{\nu}{500\,\mathrm{Hz}}\right)^2 \qquad (2.37)$$

where θ_w is the wobble angle between the spin axis and the symmetry axis amplitude in radians. The frequencies of gravitational wave emission are predicted to be at approximately the spin frequency and twice the spin frequency. Mechanisms which could produce free precession and also damp the free precession are discussed in [47].

A third process by which neutron stars could emit continuous gravitational waves are the r-mode instabilities that might be present in young, rapidly spinning neutron stars [66]. The r-mode instabilities can be generated in a fluid star if the mode of oscillation is counter-rotating in the rotation frame of the star, but in the frame of

a distant observer the oscillation mode coincides with the rotating frame. This can happen if the counter-rotation rate of the mode is lower than the rotation rate of the star. The fundamental (f-mode) and pressure (p-mode) oscillation instabilities would be important for only compact stars spinning close to the break-up limit. On the other hand, unstable r-mode oscillations, toroidal fluid oscillations where the Coriolis force of the spinning star is the primary restoring force, could develop in the known millisecond pulsars, since they have sufficient rotation rates. The amplitude of the r-mode oscillations probes the neutron star equation of state and the mechanisms which an isolated neutron star spins down. Recent estimates for r-mode maximum amplitudes are spin-down or age-based for isolated neutron stars or based on x-ray flux for accreting neutron stars in binary systems. These estimates give a range of amplitudes from $\sim 5.1 \times 10^{-6}$ for accreting neutron stars to $\sim$0.14 for young, isolated neutron stars [65].

For accreting neutron stars in binary systems, the magnetic field of neutron star guides the accretion flow to "hot spots" which might build-up the ellipticity close to the maximum breaking strain of the crust. Alternatively, magnetic fields can sustain mountains built up from the high-conductivity accreted material, depending on the magnetic field configuration [21]. All-sky surveys of actively accreting millisecond pulsars have found that no neutron stars are spinning close to their predicted break-up frequency ($\nu \sim 1400$ Hz). Since the observed spin frequency range of accreting millisecond pulsars is $270\,\mathrm{Hz} \lesssim \nu \lesssim 600\,\mathrm{Hz}$, there may be a competing mechanism preventing the spin-up of the neutron star from reaching the break-up frequency. It has been postulated that there exists a torque balance between the accretion spin-up and the gravitational emission spin-down that is causing the star to lose energy [22, 67, 78]. Those neutron stars accreting at the highest rates should have the highest gravitational wave emissions. Using this relation to balance spin-down of gravitational wave emission with x-ray luminosity (a measure of the accretion rate), the gravitational

wave amplitude is given by,

$$h_0 \approx 5 \times 10^{-27} \left(\frac{300\,\mathrm{Hz}}{\nu}\right)^{1/2} \left(\frac{F_\mathrm{x}}{10^{-8}\,\mathrm{erg\,cm^{-2}\,s^{-1}}}\right)^{1/2} \tag{2.38}$$

where F_x is the x-ray flux detected at the Earth.

The brightest x-ray source in the sky, Scorpious X-1 (Sco X-1), should also be the brightest gravitational wave emitter if the above argument holds true. Assuming torque balance equilibrium, the gravitational wave amplitude at the Earth is [6]

$$h_0 \approx 3 \times 10^{-26} \left(\frac{f}{540\,\mathrm{Hz}}\right)^{-1/2} . \tag{2.39}$$

Accretion provides a natural method to break the axial symmetry of the neutron star which therefore makes any accreting compact object a primary interest for detection of continuous gravitational waves [22].

2.5 Population of neutron stars in binary systems

The current favored model among astronomers to explain the formation of a binary system with a neutron star has several possible avenues depending on the observed state of a given system [53]. In summary, one starts with a binary system that has at least one high-mass star. The higher-mass star undergoes a supernova explosion resulting in a neutron star. The system is either disrupted by the impulsive "kick" caused by the supernova or the system may survive the explosion. If the system survives and the initially lower mass companion overfills its Roche Lobe during its stellar evolution, then the system could be observed as a source of x-ray emission during that epoch. During this mass transfer, the spin frequency of the neutron star increases because of the accreted matter delivering angular momentum to the neutron star. If the now evolved companion is still of sufficient mass to undergo a supernova,

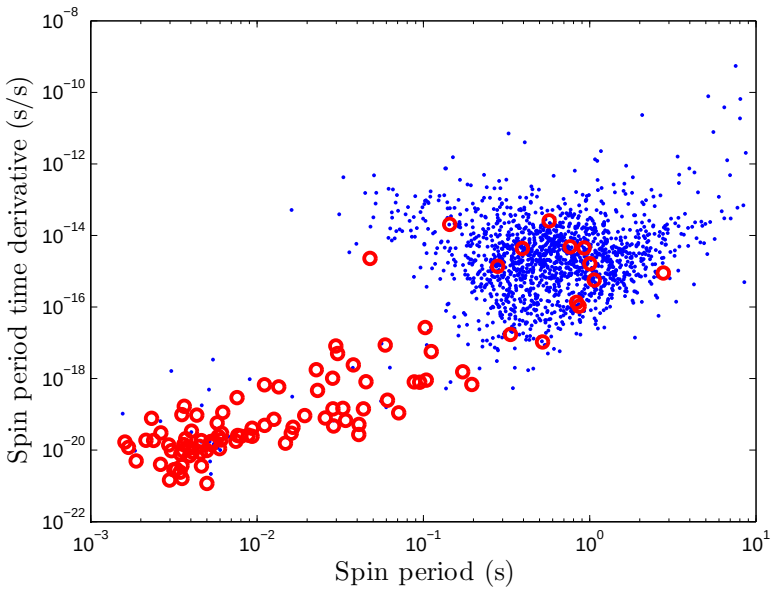

Figure 2.2: The spindown rate of known pulsars plotted against their spin periods. Two populations are clearly visible, the isolated pulsars (dots) and pulsars in binary systems (circles).

then the end result will be either a surviving double neutron star binary system or a disrupted system with a young pulsar and a pulsar whose spin frequency has possibly increased due to past accretion. Finally, if the companion does not have the mass to undergo a supernova, then the system remains bound as a high-frequency pulsar and a white dwarf companion.

Observational selection effects limit our ability to reliably estimate the number of neutron stars in our galaxy from existing surveys alone. The surveys typically rely on radio telescope data, but recently, the Fermi/LAT satellite has found several radio-quiet γ-ray pulsing neutron stars. There have been recent advances in overcoming these obstacles, however, using new radio and γ-ray detectors, new analysis techniques, and better correction for dispersion and small-number biases. At the same time, population synthesis models continue to evolve and refine our understanding of neutron star demographics.

Currently, pulsar astronomers have identified 1880 radio pulsars (see figure 2.2) [56][2] and some sources have been detected as gamma-ray pulsars [68]. Of the known radio pulsars, 163 are located within binary systems. The companions to these pulsars in binary systems range from main sequence stars, to white dwarfs, to other neutron stars. Neutron star-black hole binary systems are predicted to exist, but astronomers have not yet observed such a system. A few pulsars have recently been detected to have planetary systems. Observational evidence shows that, in general, binary systems with low-mass (below $0.7M_{\odot}$) companions have nearly circular orbits ($e \lesssim 0.01$) while higher-mass companions have more eccentric orbits ($0.15 \lesssim e \lesssim 0.9$) [53].

All-sky surveys to detect radio pulsars carried out in the 1990s have allowed astronomers to derive the characteristics of the pulsar population by observing pulsars within 1.5 kpc of the Sun. To accomplish this, astronomers use a scale factor that can be used to estimate the true population of pulsars based on the observation of nearby pulsars. Since the pulsars are located nearby, selection effects, such as dispersion or pulse beaming, can be quantified more accurately than more distant pulsars. Radio astronomers have determined that the local area density of pulsars in the galactic plane (in both binary and isolated systems) is 38 ± 16 kpc^{-2} [53].

The local pulsar population can be scaled up to the whole Milky Way if one has knowledge of the Galactocentric radial distribution. A potential strategy is to assume the pulsar population has the same radial distribution of other stellar populations. Integrating over the entire Galaxy, this model predicts $\sim$160 thousand isolated pulsars and about 40 thousand millisecond pulsars. Many of these 40 thousand millisecond pulsars would still have their evolved, white-dwarf companions [53, 73].

An alternative method to empirical modeling is to construct a population of primordial binary systems with different distributions of parameter functions: orbital period, binary mass ratio, orbital eccentricity, etc. These populations are evolved,

[2]The Australian National Telescope Facility keeps a database of all known radio pulsars and is reachable on the web via http://www.atnf.csiro.au/research/pulsar/psrcat/.

and a number of different end-state distributions are determined. These distributions are then compared with the observed or inferred populations from empirical estimates to determine the underlying distribution functions of the galactic binary population. Observing a population of neutron stars emitting gravitational waves will assist by including additional constraints on the population models.

Direct measurements of gravitational waves from a spinning neutron star can help constrain the neutron star equation of state in a complementary way to electromagnetic observations. One way to constrain the equation of state using electromagnetic observations alone is simply observation of at least one neutron star with a spin rate greater than 1 kHz [53]. Gravitational wave emission might prevent neutron stars to reach such rotation rates, however, making it possible that the equation of state will be constrained by observation of these waves instead. Observation of higher-order relativistic orbital effects in double-neutron star systems can help to measure the neutron star moment of inertia which would also be extremely valuable to constrain the equation of state [51].

2.6 Current analysis techniques for detection of continuous gravitational radiation

Many types of data analysis algorithms have been developed to search for gravitational waves from isolated neutron stars. The PowerFlux, StackSlide and Hough search algorithms carried out the first semi-coherent all-sky searches for unknown isolated neutron stars using LIGO data [4, 8, 11]. These algorithms search over sky position, frequency, spindown and–PowerFlux only–gravitational wave polarization. These methods use 30-minute-long Fourier transforms (SFTs) and sum power from the transformed data according to particular templates and weights. Unfortunately, these algorithms have not been optimized to search for sources in binary systems.

Adding the Doppler modulation due to the binary orbit would cause these searches to become cost prohibitive from a computational standpoint.

The Einstein@Home all-sky algorithm [10, 12] has been designed to increase the length of the Fourier transform coherence time as long as feasible, while keeping the entire search computationally tractable. This is possible because Einstein@Home uses the power of distributed computing to share the work of the analysis. Any person can run this analysis on a home or work computer. Small chunks of data are transferred to the local computer, the data is processed, and the results are sent back to be combined with the results of other data chunks. Eventually, the entire data set is analyzed and combined in order to find any potential continuous wave signals.

For known neutron stars, the $\mathcal{F}$-statistic search algorithm has been developed to perform long baseline Fourier transforms when the frequency and location parameters of the search are well defined [46]. Also, time-domain based approaches using a heterodyning scheme have been used to search for known neutron stars [3, 5, 7, 15]. These techniques are so powerful, that they are beginning to beat indirect spin-down limits of some known pulsars [9]. For these searches, it is possible to hunt for gravitational waves from known binary systems when the binary orbital ephemerides are well understood. Unfortunately, these fully coherent methods cannot search over the entire parameter space for unknown isolated pulsars because of computational costs that grow dramatically with total observation time and increasing frequency. Adding in unknown binary orbital parameters makes the computational costs grow even faster.

New all-sky algorithms are being actively developed for the purpose of searching for unknown neutron stars in binary systems. These methods attempt to optimize the trade-offs between computational speed with the sensitivity to gravitational waves. A new method described here takes advantage of the periodic Doppler shift caused by the changing velocity of the spinning neutron star in a binary system. Two successive

Fourier transforms are computed on the detector time series data. The resulting doubly Fourier-transformed data is then processed through a hierarchical pipeline (called *TwoSpect*) which identifies patterns in the data that are indicative of a periodic Doppler shifted signal. TwoSpect measures the period and frequency modulation depth of the Doppler shifted signals, probing every sky position and frequency for potential candidate signals. Any significant candidates found in detector data are then followed-up to identify detector artifacts or potential signals. A more detailed discussion of the TwoSpect algorithm can be found in Chapter V and the first results using the pipeline are discussed in Chapter VI.

CHAPTER III

LIGO detectors

The LIGO detectors are power-recycled Michelson interferometers with Fabry-Perot arm cavities. Interferometers are natural instruments to measure the quadrupolar tidal strain produced by gravitational waves. The arm cavity mirrors act as "freely-falling" test masses that appear to alternately move towards and away from the interferometer beamsplitter as gravitational waves pass the detector. The initial LIGO project has constructed three interferometers at two locations in the United States. One of these sites is near Richland in eastern Washington state and houses two of the three interferometers: the 4-km-long H1 detector and the 2-km-long H2 detector. The third instrument is located in Livingston Parish, Louisiana: the 4-km-long L1 detector. These three interferometers form the network of "initial" LIGO detectors. Recent, modest upgrades to the H1 and L1 detectors form the network of "enhanced" LIGO detectors, and a major upgrade to most of the existing detector hardware in the next few years will form the network of "advanced" LIGO detectors. A detailed description of the initial LIGO detectors can be found in [13]. A summary of these interferometers is given here.

The initial LIGO detectors are designed to be sensitive to gravitational wave frequencies between roughly 40 Hz up to 7 kHz, and having differential *strain* noise approaching 10^{-23} $\mathrm{Hz}^{-1/2}$ near 150 Hz in the H1 and L1 detectors (see figure 3.1).

This means that in a 1 Hz band, the root-mean-square (RMS) differential-length noise of the detector output divided by the arm cavity length of the detector approaches 10^{-23}. This incredible sensitivity is the result of using very long arm cavities, a powerful laser, aggressive seismic isolation, isolating the interferometer in a high-vacuum ($\sim 10^{-9}$ Torr) system, and finely tuned servo loops to suppress noise. The three main limiting sources of noise are 1) seismic noise (below $\sim$40 Hz), 2) suspension thermal noise of the test masses (between $\sim$40 Hz and $\sim$200 Hz), and 3) the Poisson photon counting statistics, or shot noise (above $\sim$200 Hz). For each case, the physical design of the initial LIGO detector sets the theoretical limit on the strain sensitivity (see figure 3.1). In advanced detectors, physical upgrades of different components should allow a factor of 10 improvement in the strain sensitivity across the entire LIGO band and to widen the sensitive frequency band at low frequencies, enabling interesting observations to be made down to $\sim$10 Hz.

The principal optical components of an initial LIGO interferometer are shown in figure 3.2, and are comprised of the $\sim$10.3-kg input (ITM) and end mirrors (ETM) of each arm suspended as pendula by loops of thin steel wire to isolate them from seismic motions and to approximate freely-falling test masses in the horizontal plane, a 50/50 beamsplitter, and a power recycling mirror placed between the laser source and the beamsplitter. The beamsplitter and recycling mirror are also suspended as pendula to isolate them from seismic motion. These core optics and other auxiliary input/output optics are mounted to stacks of masses and springs to further suppress seismic noise.

The interferometer laser is a Nd:YAG pumped source which emits 10-W continuously at 1064 nm [48] the frequency and Gaussian spatial profile of which are stabilized by a thermally and seismically isolated reference cavity, a fused silica pre-mode cleaner triangular cavity, and a $\sim$12-m-long, in-vacuum mode cleaner triangular cavity. These cavities form a nested frequency stabilization servo control loop with

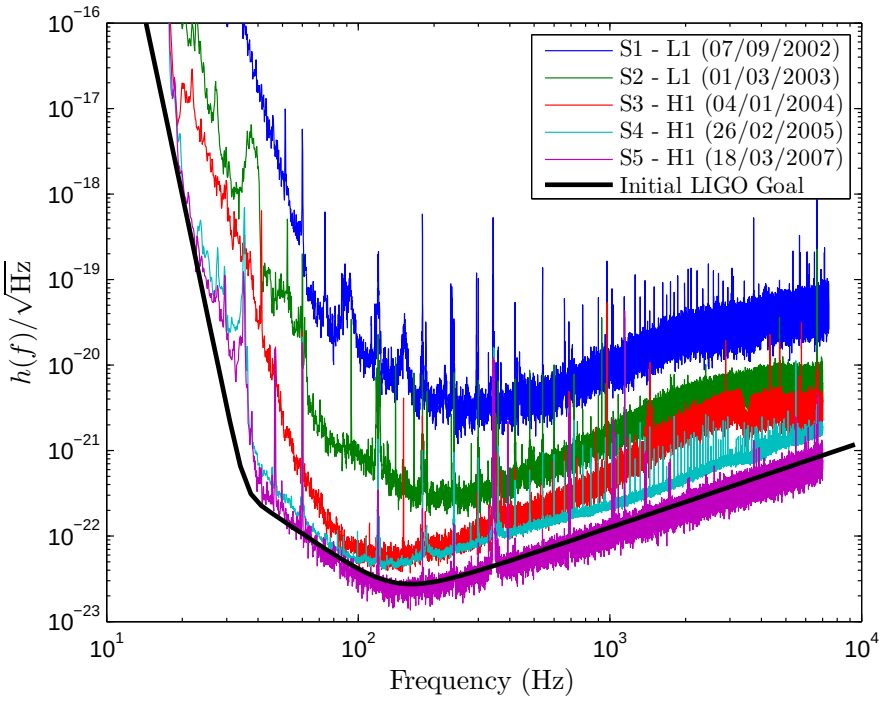

Figure 3.1: Calibrated strain noise spectral densities of the LIGO detectors showing the improvements made to the sensitivity over the course of the five initial LIGO science runs (S1 to S5). The solid black line indicates the sensitivity goal for the initial LIGO detectors.

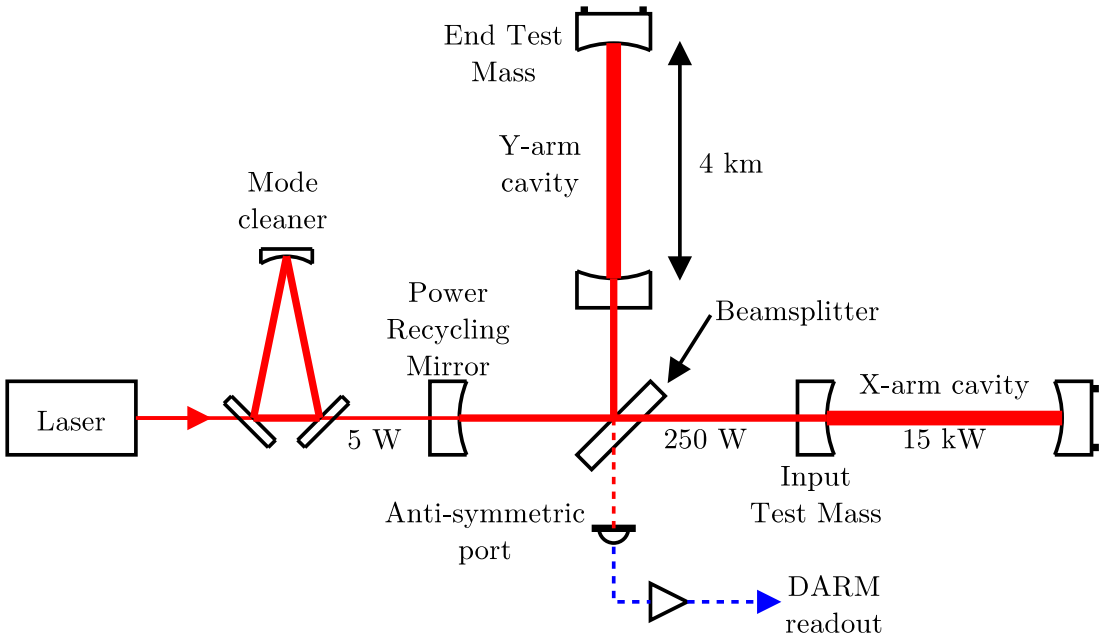

Figure 3.2: Schematic diagram of the 4-km-long initial LIGO detectors.

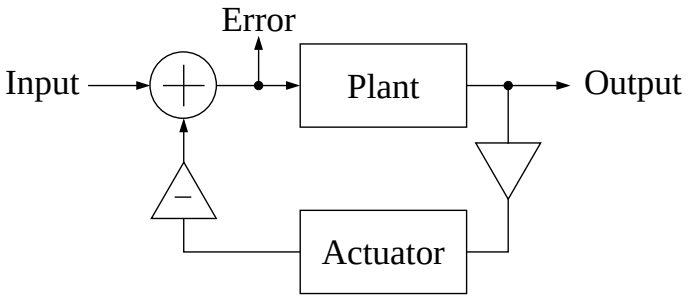

Figure 3.3: Schematic diagram of a servo control loop.

each loop imposing further frequency noise suppression needed for full interferometer servo control. Laser power stabilization is achieved through a simple feedback control loop to actuate the laser power amplifier. The laser light is phase modulated to enable the laser light to resonate in different optical cavities via Pound-Drever-Hall style control scheme [31, 74]

Servo control of interferometer parameters is essential for detector operation. The principle of a feedback servo loop is to control some system, usually called a "plant," which responds to an input stimulus. A sensor measures the response of the plant, a signal passes to an amplifier and filters, then to an actuator which attempts to cancel the response of the plant to the input (see figure 3.3). The transfer functions of the plant, P, the filters, F, and the actuator, A, are related to the open loop transfer function,

$$G = PFA\,. \tag{3.1}$$

Then, the transfer function of input, I, to the "error signal," E, is given by,

$$\frac{E}{I} = \frac{1}{1+G}\,. \tag{3.2}$$

Thus, the signal at the error point is reduced from the original input by a factor of $1/(1+G)$. The output/input relation is $O/I = P/(1+G)$.

Interferometer alignment servo control loops must maintain the 16 principal align-

ment degrees of freedom of the core interferometer optics (pitch and yaw for all 6 mirrors = 12 degrees of freedom); positions of end mirrors, recycling mirror, and beamsplitter (four degrees of freedom); plus the input beam direction (2 additional degrees of freedom). The control of these optics is achieved through nested feedback loops. Mirror specific fundamental oscillation mode damping and optical lever sensors control gross mirror angular misalignments, while more fine-tuned and sensitive global angular control is sensed by so-called "wavefront sensors" [40, 61]. Length control of the end mirrors, recycling mirror, and beamsplitter is achieved through a radio-frequency detection scheme whose variations are sensed by RF photodetectors located at the so-called "anti-symmetric port," a pick-off beam from the recycling mirror, and the reflection from the interferometer recycling mirror [74].

The arms of the LIGO interferometers are designed such that the light is stored for many round trips. Any passing gravitational wave causes a phase difference to build up between the light that is stored in each arm cavity. Power recycling further increases the amount of light circulating in the detector by sending any light that would normally be returned to the laser source back into the interferometer. The phase difference caused by passing gravitational waves is then "read out" by anti-symmetric port RF photodetectors heterodyned at the laser phase modulation frequency.

Interferometers are distinct from most other astronomical telescopes in that the operator of the interferometer is unable to point the observatory to a specific location on the sky. Gravitational wave interferometers have very broad angular resolution, and, since the LIGO interferometers are located on the Earth, their velocity relative to different points on the sky has time dependence. Therefore, even though the detectors cannot be pointed with narrow angular resolution, gravitational wave signals from particular sky locations can still be reconstructed with reasonable accuracy using the time variation in the detector response and the changing detector velocity relative

to different sky locations, or by comparing the time-of-arrival of signals in multiple detectors.

The response of an interferometer to impinging gravitational waves is wave direction and polarization-dependent. In the long-wavelength limit (up to ∼1 kHz) the response of the interferometer is frequency-independent and can be written [8, 46]

$$h(t) = F_+(t, \alpha, \delta, \psi)h_+(t) + F_\times(t, \alpha, \delta, \psi)h_\times(t) \tag{3.3}$$

where t is the time in the detector frame, α and δ are the sky coordinates in right ascension and declination, and ψ is the polarization angle of the wave, and $F_{+,\times}$ are the detector *antenna pattern* response functions to the two gravitational wave polarizations. Figure 3.4 shows the long-wavelength limit of the angular response by the LIGO interferometers to gravitational waves depending on the sky location and polarization of the incoming waves. The antenna pattern for the LIGO detectors can be readily derived in both the long-wavelength limit as well as the more general case for higher frequency gravitational wave searches [69, 76].

The LIGO interferometers are part of a world-wide network of gravitational wave detectors. The GEO600 detector outside of Hannover, Germany, is a 600-m-long detector using a slightly different optical configuration and readout scheme [54]. Near Pisa, Italy, is the Virgo detector; a 3 km interferometer using a similar optical configuration as LIGO, but with a more complicated pendulum suspension system for their core optics [16]. In Japan, near Tokyo, the 300 m TAMA interferometer was one of the first large gravitational wave interferometers and laid the groundwork for future detectors [77].

Following the fifth LIGO science run, the LIGO Laboratory began a series of modest enhancements to the existing detectors to begin commissioning advanced LIGO technology. The primary enhancements included replacing the initial LIGO laser with

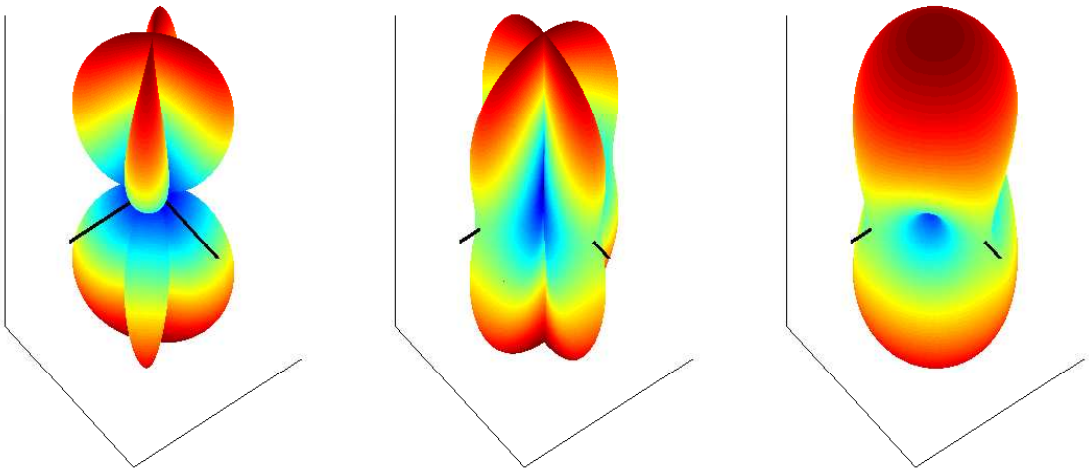

Figure 3.4: The long wavelength approximations to the LIGO detector response (antenna patterns) for the × polarization (left), + polarization (center), and circular polarization (right). The beamsplitter is located at the center of each pattern, with the arms of the interferometer indicated by the black lines. The color and distance from the beamsplitter indicates the relative sensitivity to different sky positions for the different polarizations.

a new, 35-W continuous-wave 1064 nm, Nd:YAG laser; implementing an in-vacuum "homodyne" anti-symmetric port readout scheme; installation and commissioning of a bow-tie configuration output mode cleaner placed between the recombined beam from the interferometer beamsplitter and the anti-symmetric port photodiodes; and a new, in-vacuum, active seismic isolation platform for the readout table to replace the existing passive seismic isolation [17]. These improvements have provided sensitivity improvements of a factor of 2 above ∼200 Hz and more modest improvements below 200 Hz.

In the coming years, the advanced LIGO project will begin a series of major upgrades to the enhanced LIGO detectors: 1) replicate the actively isolated in-vacuum detection table to the other in-vacuum optical tables; 2) upgrade the existing 35-W lasers to 200-W lasers; 3) install new input and core optics with improved optical coatings; 4) installation of a more isolating quadruple-pendulum core optics suspen-

sion design; 5) more massive core optics to compensate for the increased laser power with electrostatic force actuators, as opposed to the current voice coil actuators; 6) adding a seventh core optic component, the signal recycling mirror, which re-injects the gravitational wave signal back into the interferometer for further gain in sensitivity and the ability to "tune" the detector to different frequencies. These improvements should enable the advanced LIGO detectors to be approximately 10 times more sensitive than the initial interferometer design, enabling the reach of the interferometer to extend 10 times further into space, thus providing a 1000-fold increase in the total sampled volume of the Universe [39]. This should enable the first detections of gravitational waves and provide sufficient sensitivity to provide regular observations of different gravitational wave sources.

CHAPTER IV

Calibration of the LIGO detectors

Accurate and precise calibration of the magnitude and phase of a gravitational wave detector's output is essential for coincident detection techniques and waveform reconstruction of gravitational wave signals. A significant effort has been undertaken to determine the differential length response of the LIGO detectors for each of the science runs [18, 49, 50], and ongoing experiments are increasing our understanding of the various terms which enter into the overall detector calibration. In order to take full advantage of the scientific reach afforded by these detectors, continuous calibration with accuracy and precision approaching the 1% level will be required to measure, for example, the waveforms of binary black hole coalescences [52]. Detection of gravitational waves, however, does not require such stringent calibration uncertainties.

Historically, the LIGO project has relied on a calibration method to establish the magnitude of the detector response that requires extrapolation from test mass displacements about twelve orders of magnitude larger than apparent displacements expected from gravitational waves [18]. The purpose of this calibration technique is to determine the test mass actuation functions. While the precision of this method has improved over the more than five years it has been employed, the possibility of a large systematic error has not been eliminated until now.

To search for systematic errors in the LIGO calibration procedure, we have employed three fundamentally different actuator calibration techniques: the traditional *free-swinging Michelson* method [18] that relies on the wavelength of the laser light in the interferometer, the *photon calibrator* method [37] that uses the recoil of photons from an auxiliary laser source to induce calibrated test mass displacements with amplitudes close to the detector sensitivity limit, and the *frequency modulation* method [35] that is based on a calibrated frequency modulation of the laser light to create an apparent length modulation. Our investigations have spanned the frequency range from 90 Hz to 1 kHz and the range of actuation amplitudes from $\sim 10^{-8}$ m to $\sim 10^{-18}$ m.

In this chapter, the basic formalism for detector calibration in the frequency-domain will be described with a focus on methods for test mass actuator calibration that will be described and compared. Our focus on an accurate test mass actuator calibration is of critical importance because the uncertainty of this measurement has historically been the dominant source of uncertainty in the magnitude of the differential length response for each of the LIGO science runs [18, 49, 50].

4.1 DARM servo loop

The differential-arm length (DARM) control system uses a variation of the Pound-Drever-Hall (PDH) radio-frequency locking technique [31, 74] with electromagnetic displacement actuators consisting of voice coils interacting with magnets glued to the back surfaces of the suspended mirrors. The idealized force-to-length transfer function of the actuator is proportional to the inverse of the square of the excitation frequency. The DARM control loop is shown schematically in figure 4.1, and in the context of the interferometer in figure 4.2. The DARM readout signal is amplified, filtered, and then directed to the voice coil actuators on the mirrors at the ends of the arm cavities. These mirrors, together with the input arm cavity mirrors, are the *test masses* for gravitational wave signals.

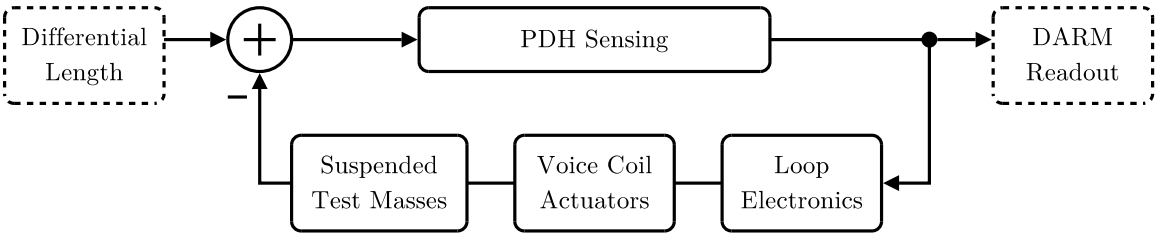

Figure 4.1: Schematic diagram of the differential arm length (DARM) feedback control loop. The Pound-Drever-Hall sensing technique is used to produce the DARM readout signal. This signal is amplified and filtered, then directed to the voice coil actuators which displace the end test masses to maintain the resonance condition in the interferometer.

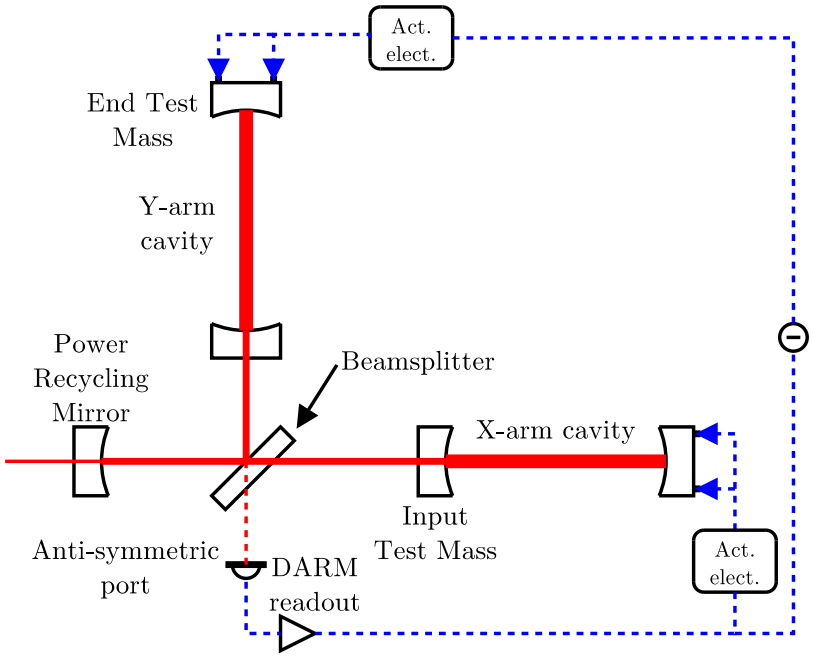

Figure 4.2: Schematic diagram of the LIGO optical configuration showing the DARM feedback control loop that actuates on the ETMs. The difference in arm lengths is sensed at the anti-symmetric port by a photodetector using the Pound-Drever-Hall reflection locking technique. The output voltage is filtered and amplified then directed to the voice coil actuators for each end test mass.

Reconstruction of differential length disturbances from the DARM readout signal requires correcting for the DARM closed-loop response. Measurement of the overall DARM loop transfer function is relatively straightforward. However, measurement of the transfer functions for components of the loop such as the sensing and actuation paths is more difficult. Calibrating the response of the interferometer to differential length variations is directly dependent on the characterization of the actuation function. In addition to the voice coil actuators and the suspended test masses, the actuation path includes actuation electronics that convert the drive voltages to coil currents. These electronics have two modes of operation, a low-noise *Run* mode, and an *Acquire* mode that allows larger drive amplitudes.

As described above, the DARM servo loop consists of a few basic elements. The components are the interferometer PDH sensing, digital filters, and actuation. These are modeled and related by the equation

$$\mathcal{G}(f) = \mathcal{C}(f)\mathcal{D}(f)\mathcal{A}(f) \tag{4.1}$$

where $\mathcal{G}(f)$ is the open loop transfer function as a function of frequency f, $\mathcal{C}(f)$ is the interferometer PDH sensing, $\mathcal{D}(f)$ is a set of digital filters, and $\mathcal{A}(f)$ is the actuation function. Each of these components are complex-valued functions. These components are briefly discussed below.

The sensing function of the interferometer converts the differential-length motion of the Fabry-Perot arm cavities into photocurrent from the output of photodiodes placed at the anti-symmetric port of the interferometer. The photocurrent is converted to a voltage by an amplifier, passes through analog filters, and into the data acquisition system. Digital filters are mathematical, frequency dependent functions which shape the frequency response of the servo loop in order to maintain stability during interferometer operation. The actuation function of the interferometer con-

verts digital counts of the differential-arm length servo control signal into differential length by actuating on the ETMs of the Fabry-Perot arm cavities.

The DARM servo loop suppresses the differential length fluctuations caused by gravitational wave signals or by external noise sources. The variation is recorded at the DARM loop "error point," located after the PDH sensing, and is referred to as the DARM readout signal. The closed-loop response is then deconvolved from the DARM readout in order to recover the differential length variations. This relation defines the *response function*

$$\mathcal{R}(f) \equiv \frac{\Delta L(f)}{R(f)} \tag{4.2}$$

where $\mathcal{R}$ is the response function, ΔL is the differential length variations, and R is the DARM readout. Servo loop algebra (see chapter III) then allows us to compute the form of the response function from the components of the loop,

$$\mathcal{R}(f) = \frac{1 + \mathcal{G}(f)}{\mathcal{C}(f)}\,. \tag{4.3}$$

The dynamics of $\mathcal{R}$ are of critical importance. The instantaneous frequency dependence of the response function is encapsulated in equation 4.3. Temporal variations, however, must be accounted for and are the result of changing interferometer operating conditions and DARM loop parameters. The sensing function varies as a function of time due to the fluctuating alignment of the interferometer optical cavities. This variation can be modeled by a scalar, time-dependent factor, $\gamma(t)$[1]. In general, the digital filters and actuation function do not change as a function of time. However, if the sensitivity of the detector can be improved by adjusting these values, then a new response function must be constructed following this change. The new parameters

[1]More precisely, $\gamma(t)$ is the multiplication of two parameters $\alpha(t)$ and $\beta(t)$, where α is the measured fluctuations of the PDH sensing function due to cavity alignment variations and β is a digital scalar coefficient, before the readout, which attempts to track and correct the loop for variations in α. The combination of these two elements, $\alpha(t) \cdot \beta(t) = \gamma(t)$, provides additional stability for the DARM servo loop. In principle, $\langle \gamma(t) \rangle \simeq 1$.

usually results in a new "epoch" of detector calibration. For a single epoch, a more general response function is written as,

$$\mathcal{R}(t, f) = \frac{1 + \gamma(t)\mathcal{G}(t_0, f)}{\gamma(t)\mathcal{C}(t_0, f)} \tag{4.4}$$

where $\mathcal{G}(t_0, f)$ and $\mathcal{C}(t_0, f)$ are the frequency-dependent open loop transfer function and interferometer sensing function at some initial time t_0.

4.2 Response function uncertainties

To understand the uncertainties involved in equation 4.4, $\mathcal{R}$ is re-written as,

$$\mathcal{R} = \frac{Ae^{i\delta}De^{i\phi}(1 + (\gamma + i\eta)Ge^{i\alpha})}{(\gamma + i\eta)Ge^{i\alpha}} \tag{4.5}$$

where the substitution $\mathcal{C}(t_0, f) = \mathcal{G}(t_0, f)/(\mathcal{D}(f)\mathcal{A}(f))$ has been made and each function is written as a complex-valued magnitude and phase except for $\gamma(t) = \gamma + i\eta$. Importantly, $\gamma(t)$ is a measured value which is determined by computing the Fourier transform of the DARM readout and using the complex Fourier coefficients for a particular sinusoidal injection frequency. This injected sinusoid is continuously present to monitor the DARM loop variations. If the measurement uncertainties in equation (4.5) are uncorrelated, then the uncertainties associated with each measurement are added in quadrature to obtain the overall response function uncertainty. The uncertainties are themselves frequency-dependent quantities.

Typically, the uncertainty in the response function is quoted as an uncertainty in terms of the magnitude and phase[2]. The difference between the true response function, $\mathcal{R}_t$, and the measured response function, $\mathcal{R}$, is $\Delta\mathcal{R} = \mathcal{R}_t - \mathcal{R}$. Normally, the relative error on a measurement of $\mathcal{R}_t$ would be written as $\Delta\mathcal{R}/\mathcal{R}_t$. For $\mathcal{R} \approx \mathcal{R}_t$,

[2]Another detector uncertainty often quoted is the residual timing uncertainty of the detector output. Further details regarding the timing uncertainty can be found in [20, 49].

the relative error can be written as $\Delta\mathcal{R}/\mathcal{R}$. Therefore, the fractional uncertainty is given by

$$\frac{\Delta\mathcal{R}}{\mathcal{R}} = \frac{\mathcal{R}_t - \mathcal{R}}{\mathcal{R}}\,. \tag{4.6}$$

The relative error in the magnitude of the response function is simply

$$\frac{\Delta|\mathcal{R}|}{|\mathcal{R}|} = \frac{|\mathcal{R}_t| - |\mathcal{R}|}{|\mathcal{R}|}\,. \tag{4.7}$$

This equation is solved in terms of $\Delta\mathcal{R}/\mathcal{R}$ with the computation,

$$\begin{aligned}
\frac{\Delta|\mathcal{R}|}{|\mathcal{R}|} &= \left|\frac{\mathcal{R}_t}{\mathcal{R}}\right| - 1 \\
&= \left|\frac{\mathcal{R} + \Delta\mathcal{R}}{\mathcal{R}}\right| - 1 \\
&= \left[\left(1 + \Re\frac{\Delta\mathcal{R}}{\mathcal{R}} + i\Im\frac{\Delta\mathcal{R}}{\mathcal{R}}\right)\left(1 + \Re\frac{\Delta\mathcal{R}}{\mathcal{R}} - i\Im\frac{\Delta\mathcal{R}}{\mathcal{R}}\right)\right]^{1/2} - 1 \\
&= \left[\left(1 + \Re\frac{\Delta\mathcal{R}}{\mathcal{R}}\right)^2 + \left(\Im\frac{\Delta\mathcal{R}}{\mathcal{R}}\right)^2\right]^{1/2} - 1\,.
\end{aligned}$$

The error in the magnitude (and phase) of the response function is expected to be small, $\lesssim$10% (and less than 20 degrees in phase). Therefore, taking terms in the square root to first order in $\Delta\mathcal{R}/\mathcal{R}$ is a reasonable approximation,

$$\begin{aligned}
\frac{\Delta|\mathcal{R}|}{|\mathcal{R}|} &\simeq \left[1 + 2\Re\frac{\Delta\mathcal{R}}{\mathcal{R}}\right]^{1/2} - 1 \\
&\simeq \left[\left(1 + \Re\frac{\Delta\mathcal{R}}{\mathcal{R}}\right)^2\right]^{1/2} - 1 \\
&= \Re\frac{\Delta\mathcal{R}}{\mathcal{R}}\,.
\end{aligned} \tag{4.8}$$

Therefore, the real components of the fractional uncertainty in the complex-valued response function will be the fractional uncertainty in the magnitude of the response function.

Since $\mathcal{R} = |\mathcal{R}| \exp(i\Phi)$, the error in phase of the response function can be calculated from

$$\begin{aligned} \Delta\Phi &= \Phi_t - \Phi && (4.9)\\ &= -i \log\left(\frac{\mathcal{R}_t}{|\mathcal{R}_t|}\right) + i \log\left(\frac{\mathcal{R}}{|\mathcal{R}|}\right) && (4.10)\\ &= -i \log\left(\frac{\mathcal{R}_t/|\mathcal{R}_t|}{\mathcal{R}/|\mathcal{R}|}\right) . && (4.11) \end{aligned}$$

It is helpful to calculate the square of the argument of the logarithm, then take the square root of this result:

$$\begin{aligned} \left(\frac{\mathcal{R}_t/|\mathcal{R}_t|}{\mathcal{R}/|\mathcal{R}|}\right)^2 &= \frac{\mathcal{R}_t\mathcal{R}^*}{\mathcal{R}_t^*\mathcal{R}} \\ &= \frac{(\mathcal{R}+\Delta\mathcal{R})\mathcal{R}^*}{(\mathcal{R}^*+(\Delta\mathcal{R})^*)\mathcal{R}} \\ &= \frac{\mathcal{R}\mathcal{R}^*+\Delta\mathcal{R}\mathcal{R}^*}{\mathcal{R}\mathcal{R}^*+(\Delta\mathcal{R})^*\mathcal{R}} \\ &\simeq \left(1+\frac{\Delta\mathcal{R}}{\mathcal{R}}\right)\left(1-\left(\frac{\Delta\mathcal{R}}{\mathcal{R}}\right)^*\right) . \end{aligned}$$

If the imaginary component of $\Delta\mathcal{R}/\mathcal{R} \ll 1$ then,

$$\begin{aligned} \frac{\mathcal{R}_t/|\mathcal{R}_t|}{\mathcal{R}/|\mathcal{R}|} &\simeq \left(1+2i\Im\frac{\Delta\mathcal{R}}{\mathcal{R}}\right)^{1/2} \\ &\simeq 1+i\Im\frac{\Delta\mathcal{R}}{\mathcal{R}} . && (4.12) \end{aligned}$$

Therefore, the phase difference between the true response function and the measured response function is

$$\Delta\Phi \simeq -i \log\left(1+i\Im\frac{\Delta\mathcal{R}}{\mathcal{R}}\right) , \qquad (4.13)$$

and thus the phase uncertainty can be calculated from the imaginary components of $\Delta\mathcal{R}/\mathcal{R}$.

Provided the uncertainties associated with each measurement are independent, the

fractional partial derivative with respect to each term will result in real or complex terms. The real or imaginary terms are summed together in quadrature to determine the fractional uncertainty in the magnitude of the response function or the difference in phase between the true and measured response functions. Thus, the quadrature sum of the real terms of $\Delta\mathcal{R}/\mathcal{R}$ evaluated for each term is

$$\left(\frac{\Delta|\mathcal{R}|}{|\mathcal{R}|}\right)^2 = \left(\frac{\Delta A}{A}\right)^2 + (L_R\Delta\gamma)^2 + (L_I\Delta\eta)^2 + \left(L_R\frac{\Delta G}{G}\right)^2 + (L_I\Delta\alpha)^2 \qquad (4.14)$$

and the phase difference uncertainty is

$$\Delta\Phi = -i\log\left\{1 + i\left[(\Delta\delta)^2 + (L_I\Delta\gamma)^2 + (L_R\Delta\eta)^2 + \left(L_I\frac{\Delta G}{G}\right)^2 + (L_R\Delta\alpha)^2\right]^{1/2}\right\} \qquad (4.15)$$

where the terms $L_R \equiv \Re\{1/[1+\mathcal{G}(t_0,f)]\}$ and $L_I \equiv \Im\{1/[1+\mathcal{G}(t_0,f)\}$.

In the case where the uncertainties are correlated, the above calculation does not accurately calculate the total uncertainty in magnitude or phase. For example, an error in measurement of $A\exp(i\delta)$ can contribute to error in measurement of $G\exp(i\alpha)$ since the voice coil actuators with actuation function $\mathcal{A}(f)$ are used to derive the open loop transfer function $\mathcal{G}(f)$. Therefore, it is advantageous to have an accurate measurement of $\mathcal{A}(f)$ so that errors do not propagate to $\mathcal{G}(f)$.

In the following sections, we describe three fundamentally different methods applied to calibrate the ETM voice coil actuators. Our goal is to determine the magnitude of the voice coil actuation function, $A = A_l(f)$, for the ETMs of the LIGO interferometers. An accurate and precise measurement is essential to determine the uncertainty in the magnitude of the response function. Finally, we will compare the results of each of the techniques.

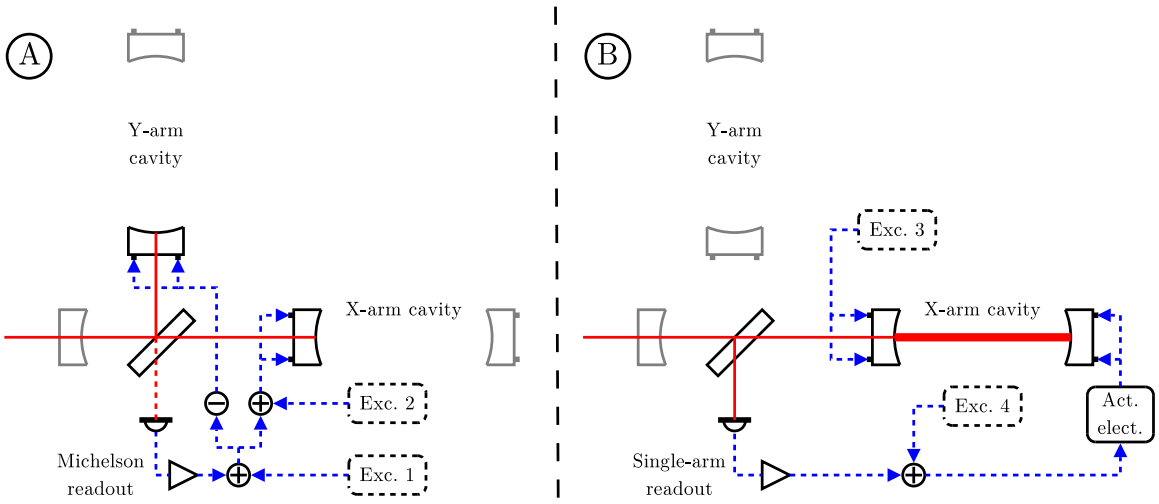

Figure 4.3: A: Schematic diagram of the simple Michelson configuration with misaligned optics shown in gray. The electronics are configured to feed back to the ITMs to maintain the dark-fringe condition at the anti-symmetric port. B: Schematic diagram of the single arm lock configuration, again with misaligned optics shown in gray. The electronics are configured to feed back to the ETM to maintain the resonance condition.

4.3 Free-swinging Michelson technique

The technique that has been the traditional calibration method employed by LIGO is referred to as the free-swinging Michelson method because it relies on measurement of Michelson interference fringes when the suspended optics are swinging freely. It thus endeavors to use the wavelength of the interferometer's laser light as a length reference to calibrate the end test mass (ETM) actuation function via a series of measurements made with both the interferometer and the actuation path electronics in various configurations and with drive amplitudes on the order of 10^{-8} m to 10^{-12} m. This process is described in detail in [49, 50]; an overview of the procedure is given here.

In summary, the first step in this process is to misalign the ETMs and the power recycling mirror, then align the input test masses (ITMs) and beam splitter to form a simple Michelson interferometer, as shown in figure 4.3A. The length control servo

electronics are configured to lock this setup on a dark fringe, i.e. with destructive interference of the light from each arm at the anti-symmetric port where the photodetector is located. Two transfer function measurements are made in this configuration, the overall open-loop transfer function (Exc. 1 in figure 4.3) and the transfer function from actuation of an ITM (Exc. 2) to the Michelson readout signal. The second measurement is repeated for the other ITM. Then, the feedback control is switched off, allowing the optics to swing freely in response to the seismic motion filtered by the vibration isolation systems. With the loop unlocked, the time series of the photodetector output is recorded as the Michelson length difference changes, causing the output to vary between the bright-fringe and dark-fringe levels. The difference between the maximum and minimum outputs corresponds to relative ITM motion of one-fourth of the wavelength of the laser light, thus providing a calibration of the anti-symmetric photodetector output signal in this Michelson configuration. Combining this result with the transfer functions resulting from ITM actuation and the overall open-loop transfer function yields a calibrated actuation function for the ITMs.

4.3.1 Calibration of the Michelson readout signal

The simple Michelson readout signal is measured by a photodetector as shown in figure 4.3A, and is used to determine the ITM actuation function by calibrating this signal using the input laser wavelength as a fiducial. The photodetector used here, however, does not measure the DC laser power. The signal measured is the demodulated power measured at angular frequency Ω. To investigate the calibration of this signal when the simple Michelson is unlocked, with optics freely swinging, we need to calculate the photodetector signal. It is useful to picture our optical layout in order to understand the associated laser fields. The layout of the unlocked simple Michelson interferometer is shown in figure 4.4. The macroscopic, constant distances to the reflecting surfaces of the x- and y-arm ITMs are l_x and l_y (from the fiducial

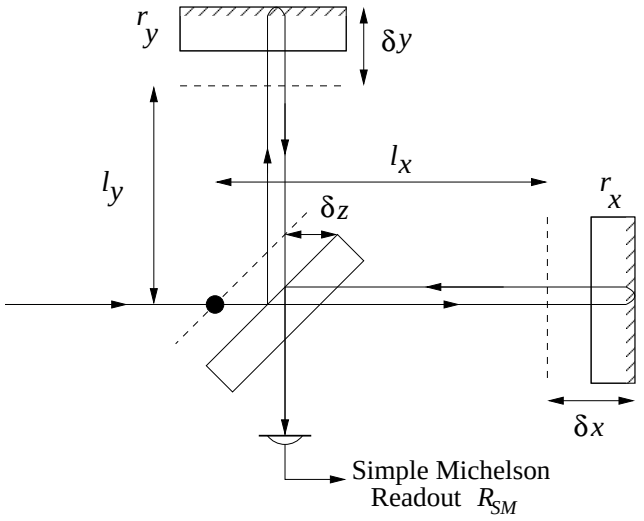

Figure 4.4: A schematic diagram of the unlocked Michelson cavity. The black dot indicates the fiducial point from which the macroscopic distances l_x and l_y and microscopic distance δz are derived.

point indicated), and the fluctuating microscopic distances are δx and δy for the two ITMs. The beamsplitter can also move microscopically by a distance given by δz.

The input laser beam electric field, E is phase modulated at angular frequency $\Omega = 2\pi \times 24.48$ MHz. The input is a superposition of all modulation harmonics,

$$E = \sum_{n=-\infty}^{\infty} E_n e^{in\Omega t} \tag{4.16}$$

where c is the speed of light and each $E_n = J_n(\Gamma)E_{\rm las}$, where J_n is the nth order Bessel function of the first kind and Γ is the modulation depth of the phase modulation.

Each $E_x^{(n)}$ and $E_y^{(n)}$ are the n-th order sideband ($E^{(0)}$ is the carrier) fields that travel down the x-arm and y-arm and back to the beamsplitter toward the photodetector at the anti-symmetric port. The E_{as} field is the superposition of the x-arm and y-arm fields on the antisymmetric side of the beamsplitter,

$$E_{as}^{(n)} = E_x^{(n)} + E_y^{(n)}. \tag{4.17}$$

More explicitly, the E_x field will be

$$\begin{aligned} E_x^{(n)} &= E_n e^{ik_n\delta z}\frac{1}{\sqrt{2}}e^{ik_n(l_x-\delta z+\delta x)}r_x e^{ik_n(l_x-\delta z+\delta x)}\frac{1}{\sqrt{2}} \\ &= \frac{1}{2}E_n r_x e^{2ik_n(l_x+\delta x-\delta z/2)} \end{aligned} \tag{4.18}$$

where $k_n = 2\pi/\lambda + n\Omega/c = k_0 + nK$ is the wave number of the n-th order sideband, r_x is the amplitude reflection coefficient of the x-arm mirror, and the argument of the Bessel function has been neglected for simplicity. Similarly, the y-arm field will be

$$E_y^{(n)} = -\frac{1}{2}E_n r_y e^{2ik_n(l_y+\delta y+\delta z/2)}\,. \tag{4.19}$$

where r_y is the amplitude reflection coefficient from the y-arm mirror. From this point onwards, the approximation that the reflection coefficients are $r_x \approx r_y \approx 1$ is made since the input mirrors have similar high reflectivity coefficients ($\approx$0.97). Thus, the $E_{as}^{(n)}$ field will be

$$E_{as}^{(n)} = \frac{1}{2}E_n\left[e^{2ik(l_x+\delta x-\delta z/2)} - e^{2ik(l_y+\delta y+\delta z/2)}\right]\,. \tag{4.20}$$

It is convenient to define $\delta\tilde{x} = \delta x - \delta z/2$ and $\delta\tilde{y} = \delta y + \delta z/2$. Then equation 4.20 becomes

$$E_{as}^{(n)} = \frac{1}{2}E_n\left[e^{2ik(l_x+\delta\tilde{x})} - e^{2ik(l_y+\delta\tilde{y})}\right]\,. \tag{4.21}$$

By definition, the photocurrent at the antisymmetric port is a measure of $P_{as} = |E_{as}^{(n)}|^2$. Writing out the individual terms to first order in Ω,

$$\begin{aligned} P_{as} = |E_{as}^{(0)}|^2 + |E_{as}^{(1)}|^2 + |E_{as}^{(-1)}|^2 + (E_{as}^{(0)}E_{as}^{(-1)*} + E_{as}^{(1)}E_{as}^{(0)*})e^{i\Omega} + \\ (E_{as}^{(-1)}E_{as}^{(0)*} + E_{as}^{(0)}E_{as}^{(1)*})e^{-i\Omega} + \cdots\,. \end{aligned} \tag{4.22}$$

Power at the first harmonic is the only necessary term since the signal is demodulated

at frequency Ω, and the photodetector is in a resonant circuit with an inductor tuned to pick out the photodiode signal at Ω. The measured quantity is

$$P_{as}^{(1)} = E_{as}^{(0)} E_{as}^{(-1)*} + E_{as}^{(1)} E_{as}^{(0)*} \,. \tag{4.23}$$

The fields $E_{as}^{(0)}$, $E_{as}^{(1)}$ and $E_{as}^{(-1)}$, are given by

$$E_{as}^{(0)} = \frac{1}{2} E_0 \left[e^{2ik_0(l_x+\delta\tilde{x})} - e^{2ik_0(l_y+\delta\tilde{y})} \right] \tag{4.24}$$

$$E_{as}^{(1)} = \frac{1}{2} E_1 \left[e^{2ik_1(l_x+\delta\tilde{x})} - e^{2ik_1(l_y+\delta\tilde{y})} \right] \tag{4.25}$$

$$E_{as}^{(-1)} = \frac{1}{2} E_{-1} \left[e^{2ik_{-1}(l_x+\delta\tilde{x})} - e^{2ik_{-1}(l_y+\delta\tilde{y})} \right] \,. \tag{4.26}$$

Since $k_0 \sim 5.9\times10^6\,\mathrm{m}^{-1}$, $K \sim 0.5\,\mathrm{m}^{-1}$, and l_x and l_y are of order meters, we can choose to construct the Michelson such that $k_0 l_x = k_0 l_y = n\pi$, and $K(l_{x(y)} + \delta x(y)) \simeq K l_{x(y)}$. As an example, the x-arm field is approximated by,

$$\begin{aligned} e^{2i(k_{\pm1})(l_x+\delta\tilde{x})} &= e^{2ik_0 l_x + 2ik_0\delta\tilde{x} \pm 2iKl_x \pm 2iK\delta\tilde{x}} \\ &= e^{2ik_0\delta\tilde{x} \pm 2iKl_x \pm 2iK\delta\tilde{x}} \\ &\simeq e^{2ik_0\delta\tilde{x} \pm 2iKl_x} \,. \end{aligned} \tag{4.27}$$

Therefore, the equations (4.24) through (4.26) reduce to

$$E_{as}^{(0)} = \frac{1}{2} E_0 \left[e^{2ik_0\delta\tilde{x}} - e^{2ik_0\delta\tilde{y}} \right] \tag{4.28}$$

$$E_{as}^{(1)} = \frac{1}{2} E_1 \left[e^{2ik_0\delta\tilde{x} + 2iKl_x} - e^{2ik_0\delta\tilde{y} + 2iKl_y} \right] \tag{4.29}$$

$$E_{as}^{(-1)} = \frac{1}{2} E_{-1} \left[e^{2ik_0\delta\tilde{x} - 2iKl_x} - e^{2ik_0\delta\tilde{y} - 2iKl_y} \right] . \tag{4.30}$$

With some algebra, the solution for $P_{as}^{(1)}$–hereafter the simple Michelson readout sig-

nal, R_{SM}–is given by,

$$R_{SM} = P_{\rm las} J_0(\Gamma) J_1(\Gamma) e^{iK(l_x+l_y)} \sin[K(l_x - l_y)] \sin[2k_0(\delta\tilde{x} - \delta\tilde{y})] \,. \tag{4.31}$$

Here, the property $J_{-m} = (-1)^m J_m$ was used to simplify the equations. The amplitude of the R_{SM} signal is determined by the input laser power, $P_{\rm las}$, the differential length, $l_x - l_y$, and the sideband and carrier amplitudes, $J_1(\Gamma)$ and $J_0(\Gamma)$. The phase of the signal is given by the common length, $l_x + l_y$, of the cavity. Any motion of the beamsplitter will always produce a differential length change.

Equation (4.31) can be simplified as

$$R_{SM} = A \sin(2k_0\delta) \tag{4.32}$$

where A encapsulates the macroscopic lengths, the sideband and carrier amplitudes, and the input laser power, which is assumed to be stable at the $\sim$1% level, and $\delta \equiv \delta\tilde{x} - \delta\tilde{y}$. The derivative of R_{SM} with respect to δ is

$$\frac{d}{d\delta} R_{SM} = A \cos(2k_0\delta) 2k_0 \tag{4.33}$$

and in the limit that the microscopic differential motion is 0, then this becomes

$$\frac{d}{d\delta} R_{SM}(\delta \simeq 0) \simeq \frac{4\pi}{\lambda} A = \frac{2\pi}{\lambda} A_{pp} = K_{SM} \,. \tag{4.34}$$

Therefore the calibration, K_{SM}, of the simple Michelson readout signal is calculated from the *maximum* peak-to-peak difference, A_{pp}, in the readout signal time series and the laser wavelength. The units of this calibration are counts of readback signal per meter of (microscopic) differential motion. An example time series segment of R_{SM} is shown in figure 4.5.

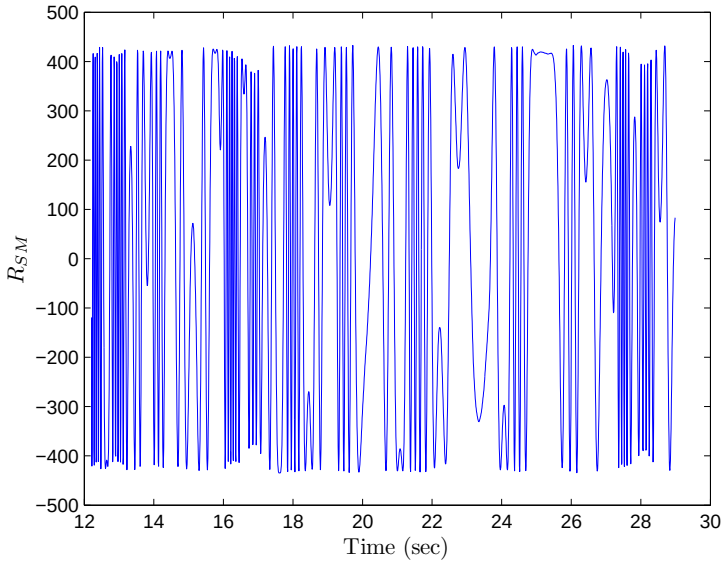

Figure 4.5: A time series segment of the simple Michelson readout signal, R_{SM}, for the H1 detector.

4.3.2 Calibration of the input test mass actuator

As summarized in section 4.3, to calibrate an ITM voice coil actuator using the previously calibrated simple Michelson readout signal, two additional measurements are needed. First, a transfer function of the ITM input signal (Exc. 2 of figure 4.3A) to simple Michelson readout, $R_{SM}/S_{l,itm}$ and, second, an open loop transfer function measurement, $\mathcal{G}_{SM}$, of the locking loop (measured from Exc. 1 of figure 4.3A) which holds the now servo-controlled simple Michelson on a dark fringe. Since the transfer function of ITM input signal to simple Michelson readout is made in a closed loop configuration, the result is suppressed by the closed-loop gain of the servo loop. Using the open loop transfer function measurement, the ITM actuation function can be calculated as,

$$A_{l,itm}(f) = \frac{R_{SM}}{S_{l,itm}} \frac{1 - \mathcal{G}_{SM}}{K_{SM}} \tag{4.35}$$

where the free-swinging simple Michelson readout calibration, K_{SM}, and the two transfer function measurements made with the simple Michelson servo controlled to

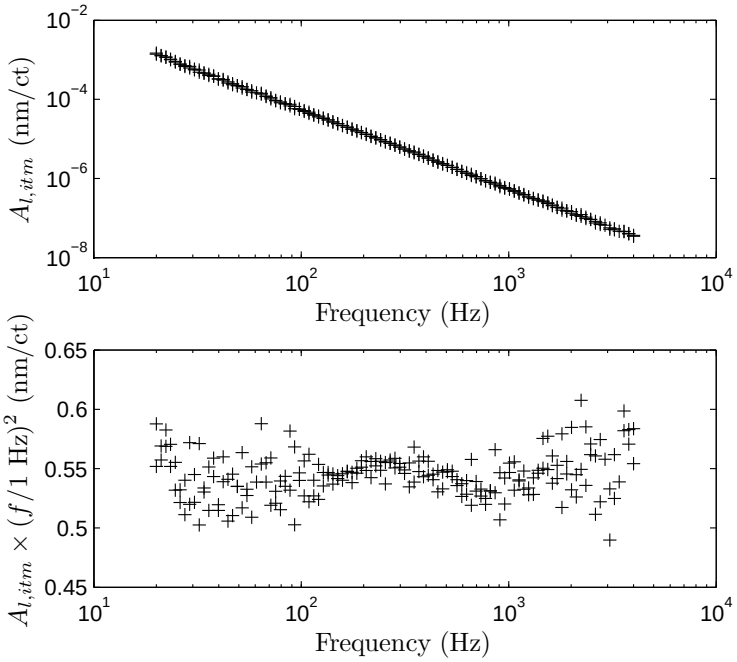

Figure 4.6: Top panel: Two sets of calibration data for the H1 x-arm ITM using the free-swinging Michelson technique. Bottom panel: The same calibration data as the upper panel with each data point scaled by the measurement frequency squared in order to compare with the expected f^{-2} frequency-dependence.

remain on a dark fringe are used to complete the measurement.

Since the measurements are made at frequencies well above the pendulum resonance frequency of the ITM of 0.75 Hz, the actuation function is expected to have a functional form proportional to f^{-2} (see figure 4.6). The frequency dependence could have a different functional form if the force exerted by the voice coils is not frequency-independent. These measurements are repeated for the other ITM.

4.3.3 Calibration of the end test mass actuator

The next step in the process is to misalign one of the ITMs and realign the ETM on the opposite arm. The servo electronics are then configured to feed back to the position of the ETM forming a resonant Fabry-Perot arm cavity as shown in

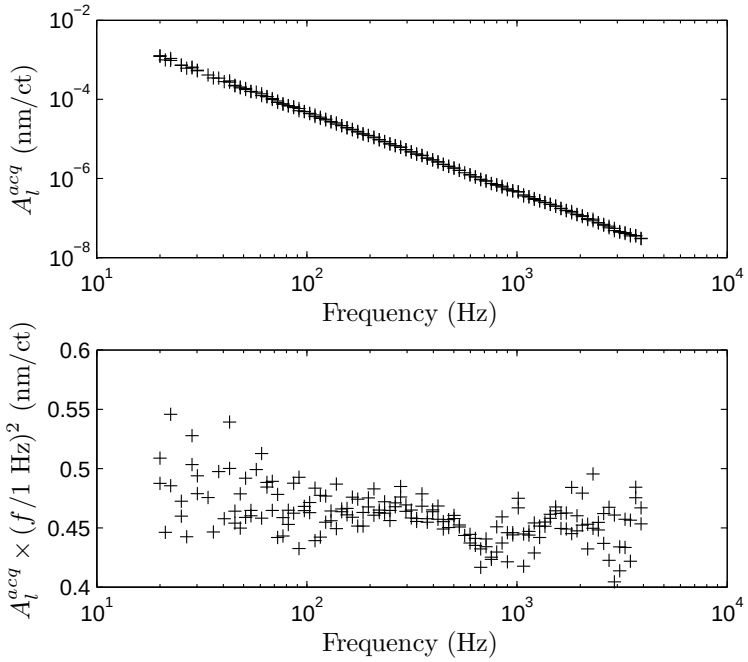

Figure 4.7: Top panel: Two sets of calibration data for the H1 x-arm ETM using the free-swinging Michelson technique. Bottom panel: The same calibration data as the upper panel with each data point scaled by the measurement frequency squared in order to compare with the expected f^{-2} frequency-dependence.

figure 4.3B. Transfer functions from ITM and ETM actuations (Exc. 3 and 4) to the photodetector output signals are then measured. Their ratio, combined with the calibration of the ITM actuation function yields the ETM actuation function, given by

$$A_l^{acq}(f) = \frac{R_{etm}}{S_l} \left(\frac{R_{itm}}{S_{l,itm}}\right)^{-1} \frac{R_{SM}}{S_{l,itm}} \frac{1-\mathcal{G}_{SM}}{K_{SM}}\,. \tag{4.36}$$

where R_{etm}/S_l and $R_{itm}/S_{l,itm}$ are the transfer functions of the single-arm servo read-back signals to the digital excitations of the ETM and ITM voice coil actuators, respectively. Here, the measurements are typically made with the ETM voice coil actuation electronics set in the Acquire mode in order to prevent saturation of the drive electronics. Similar measurements are repeated for the other arm cavity to obtain the actuation function of the other ETM.

4.3.4 Configuration of the actuation electronics

The swept-sine measurements performed in the single-arm configuration require the actuation path electronics to be in the Acquire mode. In the Acquire mode, however, the coupling of electronics noise to test mass displacement is 3-4 orders of magnitude larger than in the Run mode, which is used for gravitational wave searches. There are four parallel paths for the four voice coil actuators on each ETM and several components in each path. Measuring and combining the electronics transfer functions is a complicated and challenging task. Converting calibrations performed using the free-swinging Michelson method to the high-sensitivity, fully-locked interferometer configuration requires correcting for subtle differences between the Acquire and Run mode actuation paths.

The Acquire and Run paths contain digital and analog whitening/dewhitening filters and the analog coil driver electronics which convert voltage to coil current as shown in figure 4.8. Digital filters are produced whose transfer functions are the mathematical inverses of the analog coil drive electronics. The whitening/dewhitening filters are used in the DARM readout and in the actuation paths so that the digital control system is not overly saturated by the enormous low frequency control (below the most sensitive frequency band of LIGO) needed to compensate for seismic noise variations. The analog whitening/dewhitening filters are measured and their effect is compensated for by using their inverse in digital filters.

The traditional free-swinging Michelson calibration measurements made during the S5 science run were made with the ETM electronics set in the Acquire mode. This is because the amplitude of drive required in the previous steps of the procedure to obtain precise measurements will saturate the electronics if set in the Run mode. During normal science operations, the ETM electronics are set to the Run mode. In each of these states, digital filters are engaged such that, ideally, the transfer function is unity across a wide frequency band from 10 Hz to $\sim$7.5 kHz at which point the

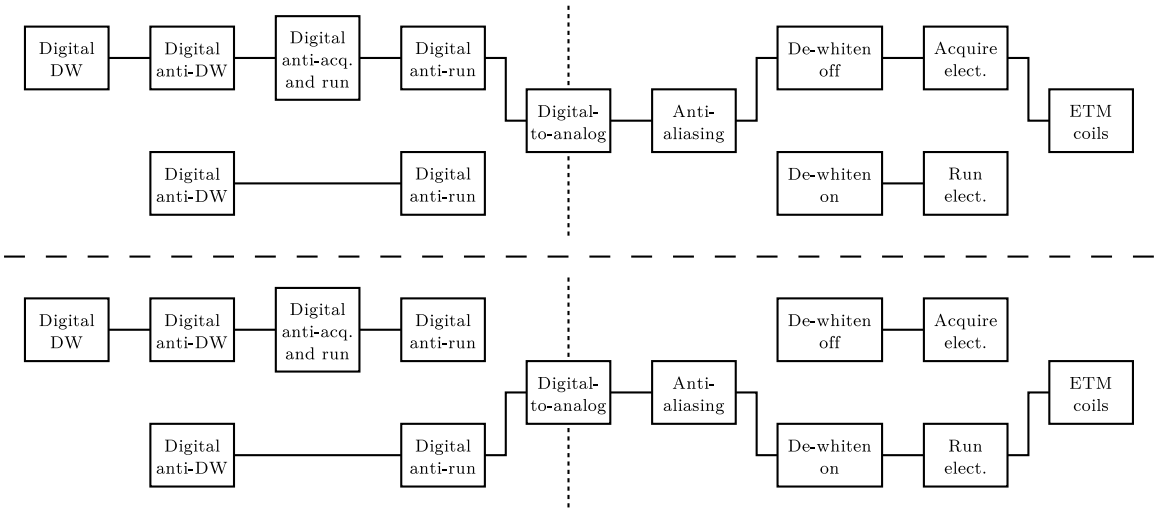

Figure 4.8: Upper section shows the typical ETM electronics configuration during the free-swinging Michelson measurements. The lower section shows the ETM electronics configuration when running the interferometers in their most sensitive state. There are individual paths for each of the four voice coil actuators controlling the longitudinal position of the ETM. Not shown are digital notch filters which only effect a very narrow region in frequency and have negligible effect at other frequencies.

analog anti-aliasing filter is strongly suppressing high frequency signals.

It was discovered, following the science run, that the transfer function was not unity across the transition between configurations. The discovery meant that actuation coefficient measurements made in a different electronics configuration did not give an accurate measurement of the actuation coefficient in the nominal science configuration.

It is possible to include the electronics difference into the actuator calibration but this will incorporate additional uncertainty into the overall actuator calibration uncertainty estimate. To include this difference, transfer function measurements of the analog electronics are made for each of the four coil paths for each of the ETMs, and the digital compensation filters' mathematical transfer functions are applied in the calculation as follows:

$$A_l^{run} = A_l^{acq} \frac{H_{dw\,on}}{H_{dw\,off}} \frac{H_{run}}{H_{acq}} \frac{1}{D_{dw}\, D_{anti.acq,run}} \tag{4.37}$$

where A_l^{acq} are the measured frequency dependent actuation coefficients, $H_{dw\,on}$ is the frequency-dependent analog transfer function of the dewhitening filters in the "on" state, $H_{dw\,off}$ is the analog dewhitening transfer function measurement in the "off" state (which is designed to be a frequency-independent stage with gain equal to 1), H_{run} is the frequency-dependent analog transfer function measurement of the coil driver electronics in the Run state, H_{run} is the transfer function measurement in the Acquire state, D_{dw} is the digital filter transfer function of the dewhitening filters which have been modeled and fitted using the analog dewhitening filters, $D_{anti.acq,run}$ is a combination of two filters, the digital anti-acquire filter and the digital run filter which are modeled and fitted using the digital inverse of the analog Acquire electronics and the analog Run electronics, respectively.

The frequency-dependent average of the measurements made along the four voice

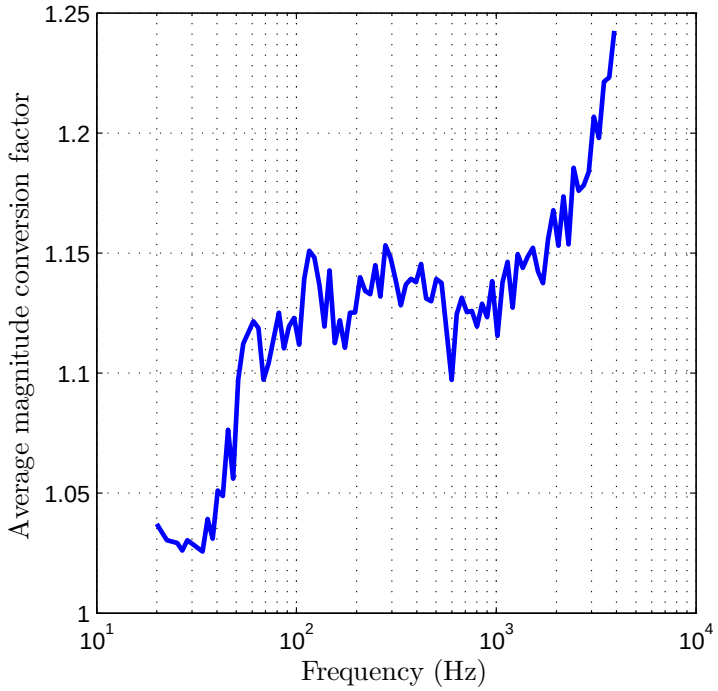

Figure 4.9: Example of the frequency-dependent factor to convert Acquire mode measurements into Run mode measurements derived from the average of 4 ETM voice coil digital compensation filters and analog electronics for the H1 x-arm. Measurements were made following the conclusion of the fifth science run.

coil paths is computed in order to determine the overall change caused by the electronics differences. Ideally, this should be a frequency-independent value of unity. Since the analog measurements are made using different frequencies from the actuation coefficient measurements, a simple interpolation is applied to relate the different frequency points. While this Acquire to Run correction reduces a potentially severe systematic error, it unfortunately will also introduce additional statistical uncertainty due to the additional transfer function measurements in different electronic configurations that were required to correct for the systematic error.

4.3.5 Free-swinging Michelson method conclusions

The fundamental premise of the free-swinging Michelson technique relies on the wavelength of the laser light as a length fiducial for calibration of the LIGO ETMs. Aligning the interferometer into simple optical configurations for translation of the simple Michelson readout calibration to an ITM and finally an ETM calibration relies on multiple, sequential transfer function measurements. Multiple transfer function measurements in various interferometer and electronic configurations are needed, and can increase the statistical uncertainty of the final ETM voice coil calibration. The transfer function measurements are not a fundamental limitation of the procedure, however, only the way the LIGO Calibration Team has chosen to employ the technique. One could, in principle, choose to measure at a few frequencies to reduce statistical uncertainty by averaging many measurements.

During the nearly 10 years of its use in calibrating the ETMs of the LIGO detectors, our confidence in the free-swinging Michelson measurement procedure has improved, and the 2-year stability of these calibration measurements has been observed during the fifth science run [49]. While the precision of the measurements on any given day is quite high, there are variations in the calibration results that are not well understood. A changing systematic effect appears to be varying from measurement to measurement with a variation of approximately 10%. Recent work by the LIGO Calibration Team has placed an emphasis on uncovering the systematic differences between measurements.

The simplicity of the free-swinging Michelson technique, relating the wavelength of light to the ETM motion, is elegant but must be carefully employed since the measurements take place in different electronics and optical configurations. The LIGO Calibration Team continues to use this technique and is pioneering new efforts to reduce the systematic and statistical variations. Comparing these results with other techniques is a key step in uncovering potential systematic uncertainties of the LIGO

detector calibration (see section 4.6).

4.4 Frequency modulation calibration technique

In this section, we describe a fundamentally different method that is based on frequency modulation of the laser light. Much of the material from this section will soon be published in Classical and Quantum Gravity [35]. Some additional details are described that are beyond the scope of the article.

For this technique, the interferometer is operated in a single-arm configuration. The frequency of the laser light is sinusoidally modulated, and this modulation is interpreted by the sensor of the arm cavity locking servo as a length modulation, providing a fiducial for ETM voice coil actuator calibration. This method has been used both to calibrate the LIGO actuators and to investigate systematic errors associated with other calibration methods [36].

For a resonant Fabry-Perot cavity, frequency variations and length variations are related by the dynamic resonance condition [70] which is given by

$$C(f)\frac{\Delta\nu(f)}{\nu} = -\frac{\Delta L(f)}{L}\,. \tag{4.38}$$

Here f is the frequency of the variations, ν is the laser frequency, L is the cavity length, $\Delta\nu(f)$ and $\Delta L(f)$ are the amplitudes of the sinusoidal variations, and $C(f)$ is the normalized frequency-to-length transfer function given by

$$C(f) = \frac{1 - e^{-4i\pi fT}}{4i\pi fT}\,, \tag{4.39}$$

where $T = L/c$ is the light transit time in the cavity. Equation (4.39) for the LIGO arm cavities is plotted in figure 4.10. A calibrated frequency modulation, $\Delta\nu$, thus results in a calibrated length modulation, ΔL.

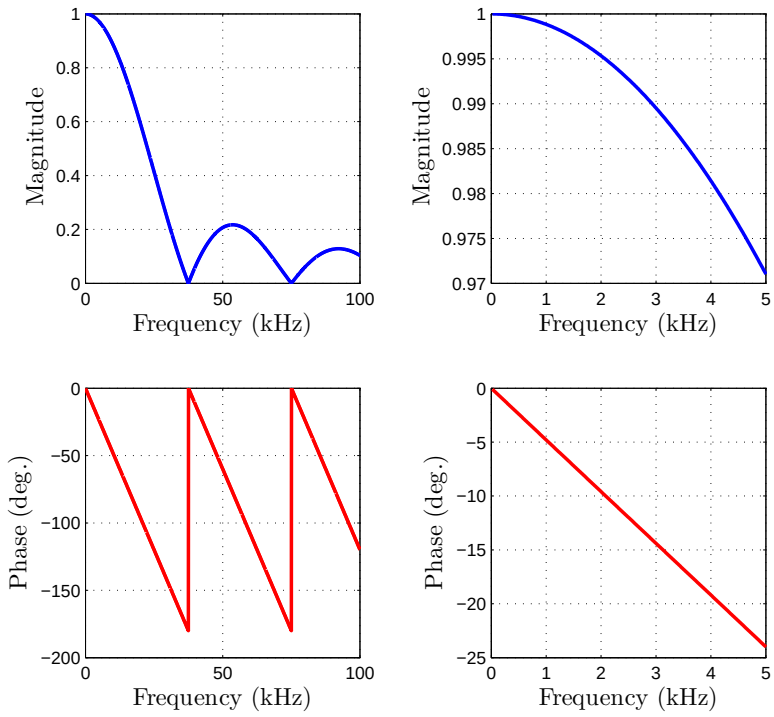

Figure 4.10: Magnitude and phase of the frequency-to-length transfer function, $C(f)$, for the LIGO 4-km-long arm cavities over a 100 kHz span (left) and over a 5 kHz span (right).

Calibration of the injected frequency modulation is the first step in applying this method. This is described in detail in section 4.4.1. We then proceed with calibration of the ETM voice coil actuators via measurements made in a single-arm lock configuration, as shown schematically in figure 4.11 and discussed in more detail in section 4.4.2. Temporal variations in the arm locking control loop are minimized by simultaneously driving both the ETM voice coil actuator and an effective length variation via modulation of the laser frequency, with the two excitation frequencies separated by a fraction of a hertz. The arm length variations appear as two closely-spaced peaks in the power spectrum of the readout signal of the arm length control servo (see figure 4.11). With the frequency excitation providing an independent and calibrated effective arm length variation, the ratio of the two peaks yields the voice coil actuation coefficient.

A key advantage of this technique is that it does not exert localized forces on the test masses in addition to the forces exerted by the voice coil actuators. Such additional calibration forces can cause elastic deformation of the test masses and can be a dominant source of systematic errors for other calibration methods [37, 42]. The frequency modulation method should thus enable investigation of the elastic deformation induced by the voice coil actuator forces [19].

4.4.1 Calibration of the frequency actuation

To modulate the laser frequency, we utilize a frequency shifter, composed of a double-passed acousto-optic modulator (AOM) and an AOM driver, that is embedded within a laser frequency locking servo as shown in figure 4.11. The voltage-controlled oscillator (VCO) at the heart of the AOM driver operates at a nominal frequency of 80 MHz. This frequency changes in response to the AOM driver input signal. The unity gain frequency of the frequency locking servo is approximately 600 kHz and the gain at 100 kHz is more than 25 dB. Thus, for the frequencies of interest for our

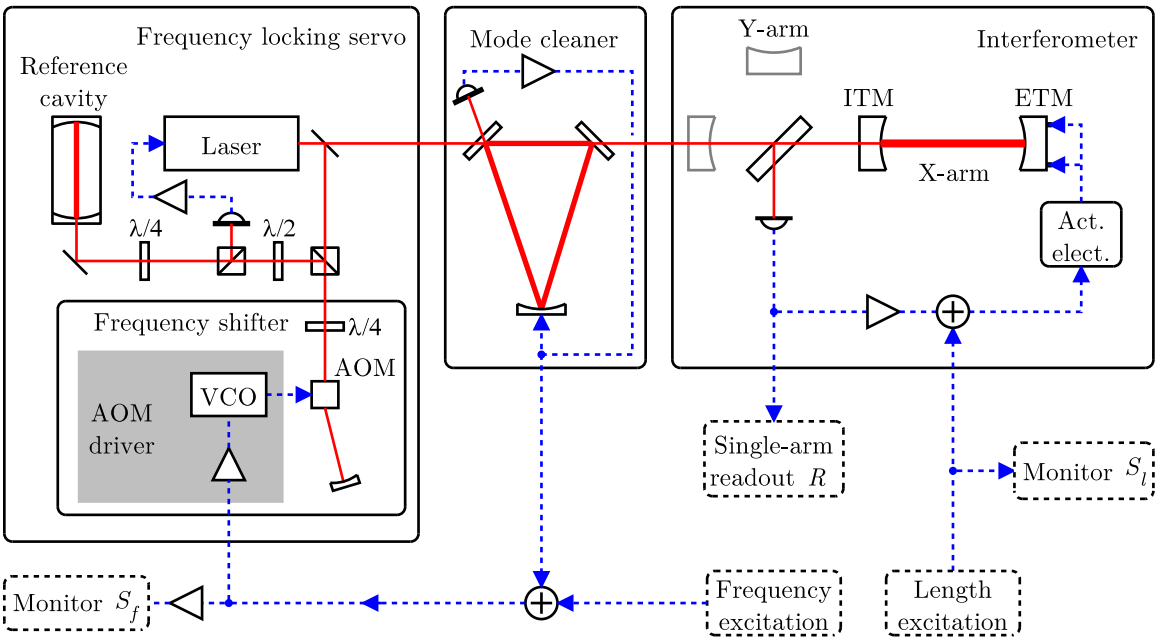

Figure 4.11: Schematic of the experimental setup used to calibrate the ETM voice coil actuators using the frequency modulation technique. The laser frequency is locked to a resonance of the reference cavity. Driving the VCO input injects a frequency modulation into the frequency locking servo loop via the double-passed AOM. The frequency servo acts on the laser frequency to cancel the injected modulation, thus imposing the inverse of the modulation on the laser light directed to the mode cleaner. The mode cleaner filters the frequency modulated light which then impinges on the arm of the interferometer. The arm length is held on a resonance by the voice coil actuators that control the position of the ETM.

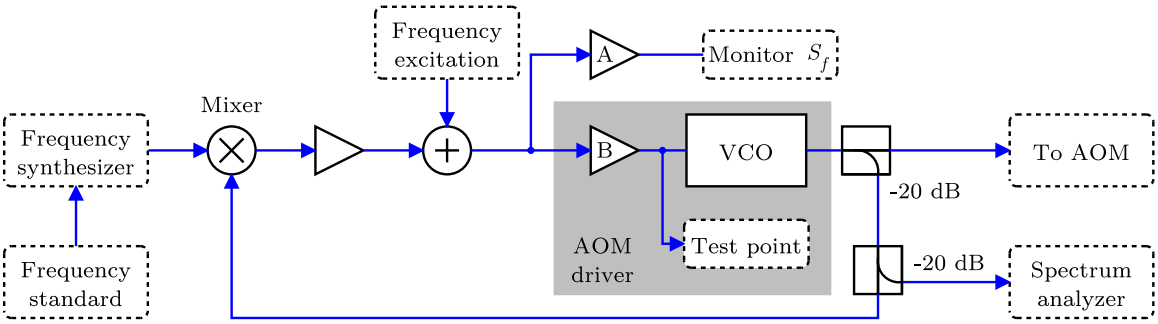

Figure 4.12: Schematic of the feedback control loop used to lock the VCO to a frequency synthesizer to measure the magnitude of the induced frequency modulation. The sideband-to-carrier power ratio is measured with an RF spectrum analyzer.

measurements (< 1 kHz), changes in the laser output frequency induced by changes in the AOM driver input signal are equal and opposite to the frequency changes induced by the double-passed AOM.

To characterize the AOM driver, the output frequency is locked to a frequency synthesizer, which is itself locked to a frequency standard, as shown schematically in figure 4.12. This minimizes frequency drifts in the AOM driver output, enabling precise measurement of the amplitudes of the carrier and modulation sidebands using a spectrum analyzer. The unity gain frequency of this temporary locking servo is approximately 400 Hz. To calibrate the AOM driver input monitor signal, we inject a sinusoidal frequency excitation as shown in figure 4.12, measure the closed-loop signal response at the S_f monitor point, and use an RF spectrum analyzer (Agilent 4395A) to measure the ratio of the power in one of the induced first-order frequency modulation sidebands with respect to the carrier.

The time-varying electric field of the frequency modulated laser source can be expressed as

$$E(t) = E_0 e^{i(2\pi\nu t + \phi(t))} \tag{4.40}$$

where E_0 is the amplitude of the sinusoidally varying electric field and

$$\phi(t) = 2\pi \int_0^t \Delta\nu \cos(2\pi f\tau)\mathrm{d}\tau = \Gamma \sin(2\pi f t)\,, \tag{4.41}$$

with the modulation index, Γ, given by $\Gamma = \Delta\nu/f$. The frequency-modulated field can be decomposed into a carrier and a series of frequency-shifted sideband fields by writing it as an infinite series of Bessel functions of the first kind, J_n, as

$$E(t) = E_0 e^{2i\pi\nu t} \sum_{n=-\infty}^{\infty} J_n(\Gamma) e^{2i\pi n f t}\,. \tag{4.42}$$

The ratio of the power in one of the first-order sidebands with respect to the power in the carrier is then given by $P_1/P_0 = J_1^2(\Gamma)/J_0^2(\Gamma)$. By measuring the sideband and carrier powers, this expression yields Γ and therefore $\Delta\nu$, the amplitude of the laser frequency modulation.

The calibration function for conversion of S_f to amplitude of the frequency modulation at the AOM driver output, $\mathcal{K} = \Delta\nu/S_f$, is determined by simultaneous measurement of the power spectrum of S_f during the sideband and carrier power measurements (see figure 4.13). To interpolate to other modulation frequencies and to assess the frequency response of the VCO, we also measure the magnitudes of the frequency-dependent transfer functions of the analog electronics, denoted by blocks A and B in figure 4.12, $H_A(f)$ and $H_B(f)$. The VCO actuation coefficient, α, which we expect to be frequency-independent, is determined by a least-squares fit using pole-zero approximations of the measured electronics transfer functions, with α as the only free parameter ($\mathcal{K}(f) = \alpha H_B(f)/H_A(f)$). The normalized deviation between the measured values of $\mathcal{K}$ and the fit (meas./fit-1) is shown in the lower panel of figure 4.13. The standard error of the mean value relative to the expected frequency-independent actuation coefficient is 0.1%, dominated by statistical fluctuations in the

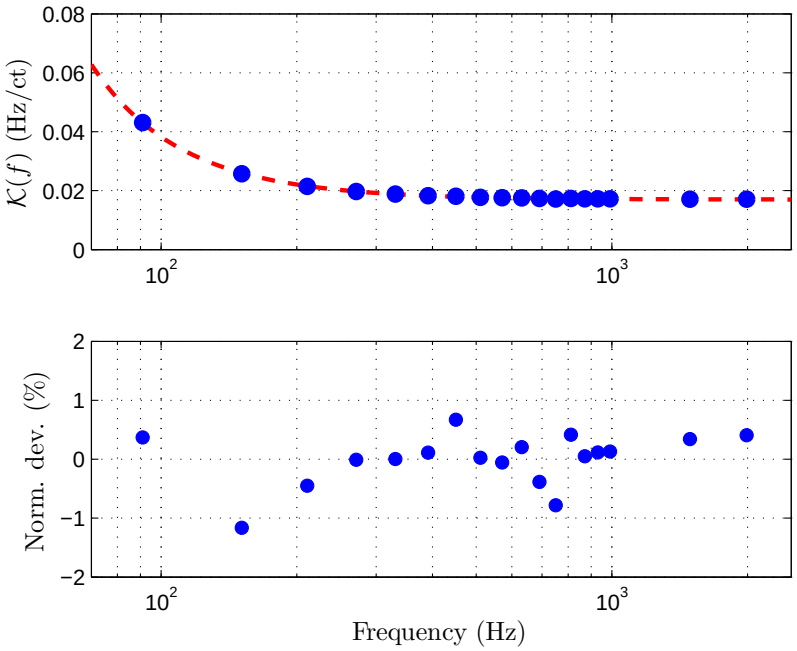

Figure 4.13: Calibration function, $\mathcal{K}$, for the S_f monitor point. The circles in the upper panel indicate measured values, and the dashed line is a least-squares fit assuming a frequency-independent VCO actuation coefficient, α. The normalized deviations between the measurements and the fit are plotted in the lower panel.

measurement of the sideband-to-carrier power ratio (see section 4.4.3).

In order to increase our confidence in the measurement and model comparison, we constructed a Matlab Simulink model of the frequency locking loop. The inputs to the model are the fitted poles and zeros of the filters in blocks A and B. There are two free parameters of the model; first, the overall gain of the locking loop; and second, the VCO actuation coefficient α. Once the overall gain is computed by fitting to the open loop transfer function, α is determined by a least-squares fit to the measurements of sideband-to-carrier power ratio and signal measured at S_f. Figures 4.14 through 4.16 show the comparison of our measurements with the constructed model.

Laser light with the frequency modulation imposed by the frequency locking servo is transmitted through a mode cleaner before impinging on the arm cavity ITM (see

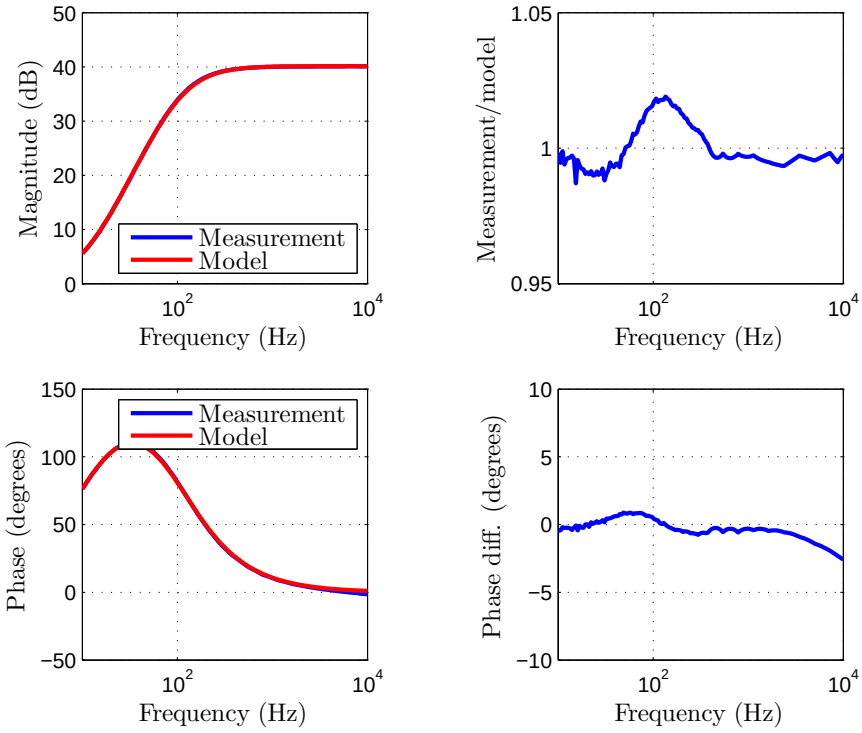

Figure 4.14: Left: Magnitude and phase of the transfer function measurements (blue) and pole-zero approximation (red) for block A. Right: Comparing the measurement and fit by the ratio of the transfer function magnitudes and the difference in transfer function phase.

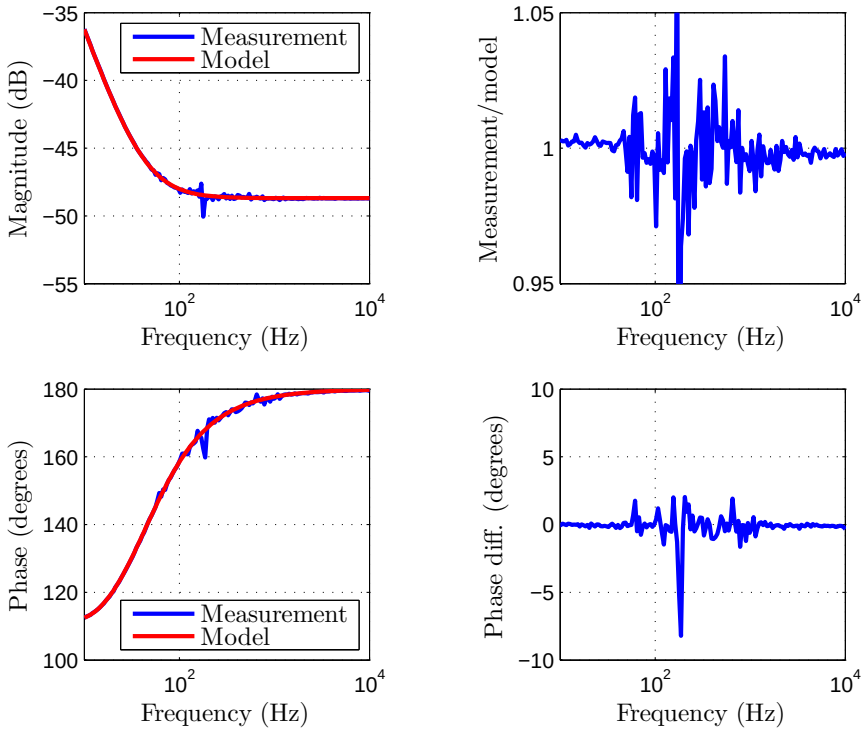

Figure 4.15: Left: Magnitude and phase of the transfer function measurements (blue) and pole-zero approximation (red) for block B. Right: Comparing the measurement and fit by the ratio of the transfer function magnitudes and the difference in transfer function phase.

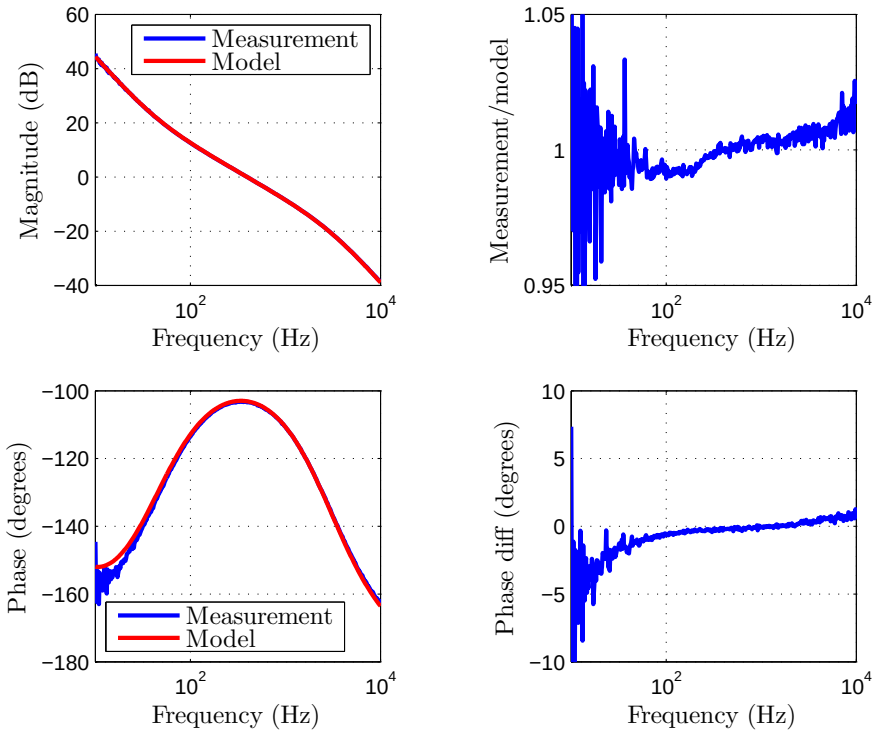

Figure 4.16: Left: Locking loop open loop gain transfer function measurement (blue) and fit (red) using a frequency-independent VCO actuation coefficient and the pole-zero approximation for the block B transfer function. Right: Comparing the measurement and fit by the ratio of the transfer function magnitudes and the difference in transfer function phase.

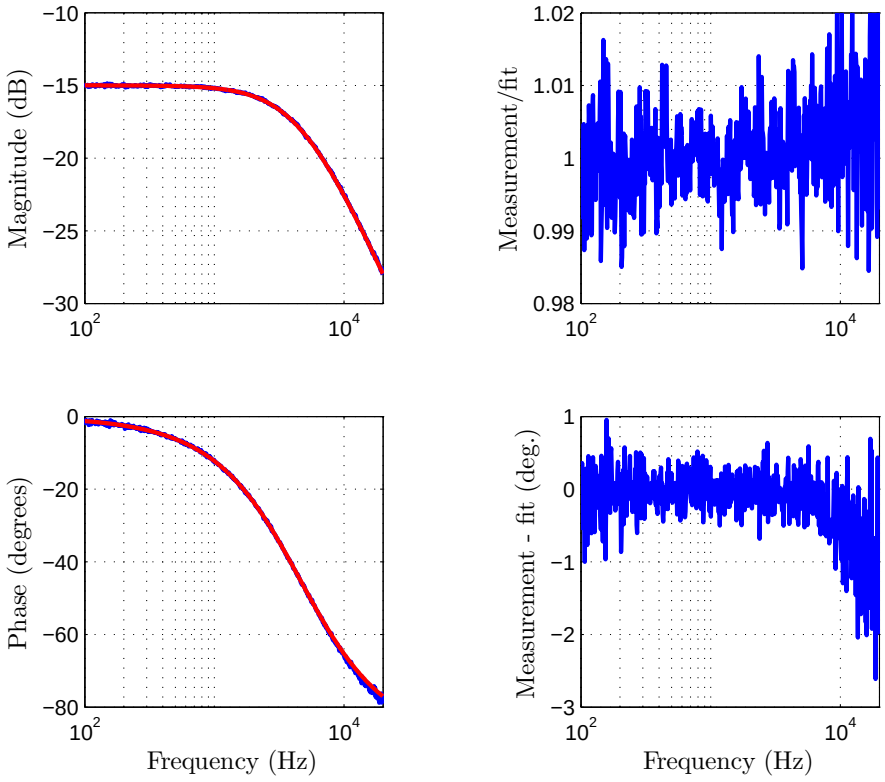

Figure 4.17: Left: Magnitude and phase of the transfer function measurements (blue) and single-pole approximation (red) for the H1 mode cleaner. Right: Comparing the measurement and fit by the ratio of the transfer function magnitudes and the difference in transfer function phase.

figure 4.11). This 12-m-long, triangular Fabry-Perot resonator has an optical storage time of approximately 35 μs that filters the laser frequency variations. To characterize the mode cleaner's passive filtering, we measure the power modulation transfer function from 10 Hz to 10 kHz using photodetectors located upstream and downstream of the mode cleaner. For modulation frequencies well below the mode cleaner cavity's free spectral range of 12.3 MHz, the response to power variations is functionally equivalent to the response to frequency variations, and can be approximated by a single real pole at frequency f_0 [69, 70]. Fitting the magnitude and phase of this transfer function with a single real pole yields $f_0 = 4.61$ kHz (see figure 4.17).

The amplitude of the frequency modulation downstream of the mode cleaner is

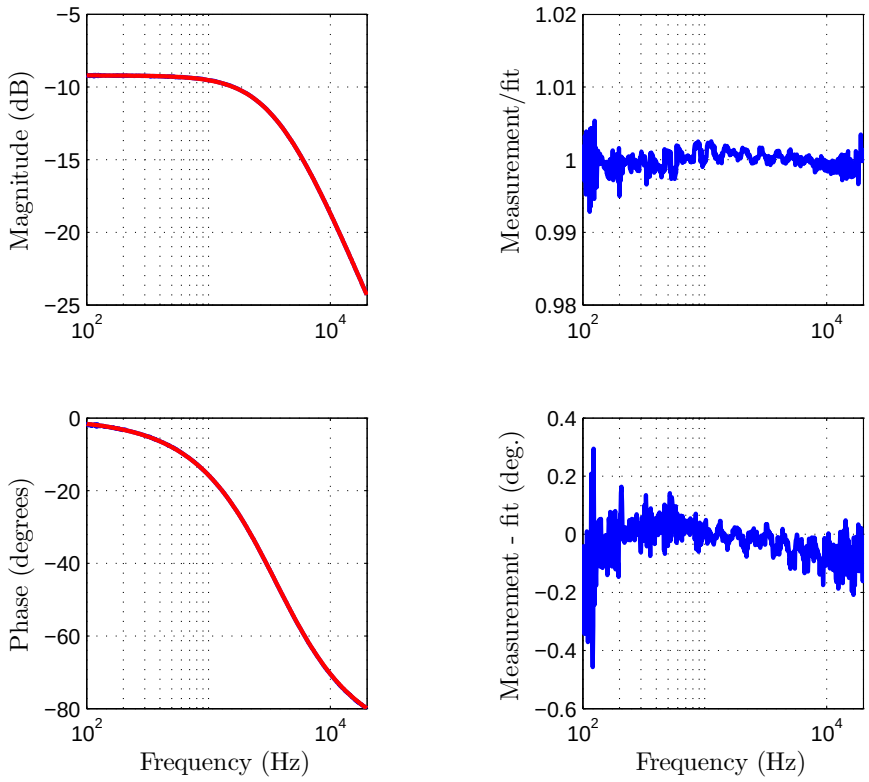

Figure 4.18: Left: Magnitude and phase of the transfer function measurements (blue) and single-pole approximation (red) for the H2 mode cleaner. Right: Comparing the measurement and fit by the ratio of the transfer function magnitudes and the difference in transfer function phase. The fitted pole frequency for the H2 mode cleaner is 3.55 kHz.

thus given by

$$\Delta\nu_t(f) = \Delta\nu_i(f)\, H_{mc}(f) \simeq 2\Delta\nu(f) \left| \frac{f_0}{f_0 + if} \right| = \frac{2\Delta\nu(f)}{\sqrt{1 + f^2/f_0^2}} \tag{4.43}$$

where $\Delta\nu_i$ and $\Delta\nu_t$ are the sinusoidal amplitudes of the incident and transmitted frequency modulations and H_{mc} is the frequency modulation transfer function of the mode cleaner. Here, $\Delta\nu_i = 2\Delta\nu = 2\mathcal{K}S_f$. The factor of 2 results from double-passing the AOM. The feedback control loop that holds the mode cleaner on resonance actuates on both the length of the mode cleaner (at low frequencies) and the frequency of the laser light via the AOM driver (at higher frequencies) as shown in figure 4.11. To ensure that length actuation by the mode cleaner locking servo is not changing the expected filtering function of the mode cleaner, a digital notch filter, centered at the measurement frequency, is inserted into the length control path.

4.4.2 Calibration of the interferometer displacement actuator

Our principal objective is determination of the actuation functions for the voice coil actuators which control the positions of the ETMs. Assuming that the coil driver electronics transfer functions are flat over the frequency range of our measurements, we expect the voice coil actuators to deliver longitudinal forces that are independent of the drive frequency. Our measurements are made at frequencies well above the 0.75 Hz pendulum resonance frequencies of the suspended test masses, so we expect them to behave as free masses with displacements that are 180 degrees out of phase with the forces from the voice coils and decreasing with the inverse square of the drive frequency. To calibrate a voice coil actuation coefficient at a given frequency, we lock the particular single arm of the interferometer and simultaneously drive both the laser frequency actuator and the voice coil actuators with sinusoids at frequencies separated by 0.1 Hz. We monitor the magnitudes of the induced peaks in the power

spectra of the arm locking servo readout signal, the frequency modulation drive signal, and the voice coil drive signal[3].

Using equations 4.38 and 4.43, the effective length modulation induced by the frequency modulated light incident on the arm cavity is given by

$$\Delta L(f) \simeq \frac{-C(f)L}{\nu}\Delta\nu_t(f) = \frac{-C(f)L}{\nu}\, 2\mathcal{K}(f)\, H_{mc}(f)\, S_f = A_f(f)\, S_f\,. \tag{4.44}$$

Here, A_f is the function that converts the AOM driver input monitor signal, S_f, to effective arm cavity length variation. The calculated ETM voice coil calibration coefficient, A_l, is then calculated from the ratios of the sinusoidal injection amplitudes in the amplitude spectral densities of the single arm readback and the signal readbacks of frequency and length modulation and the ratio of the single arm response to length variations at the frequency of length or frequency variations. Mathematically, this is written,

$$A_l(f) = A_f\, \frac{S_f}{S_l}\, \frac{R_l}{R_f}\, \frac{r_l}{r_f} \tag{4.45}$$

where S, R, and r terms with subscript l and f are measured at the length and frequency excitation frequencies, respectively; R_l and R_f are the amplitudes of the peaks in the power spectrum of the arm locking readout signal; S_l is the amplitude of the peak in the ETM length excitation monitor point signal (see figure 4.11); and r_l and r_f are the closed-loop responses of the single-arm cavity locking readout signal to length fluctuations. For simultaneous excitations, the final ratio, r_l/r_f, allows propagation of the calibration from the VCO excitation frequency to the voice coil excitation frequency. Simultaneous excitation minimizes the influence of temporal variations in interferometer and control loop parameters such as optical gain changes due to alignment fluctuations. The r_l/r_f ratio can be estimated from a model of the

[3]Note that the actuator for the arm locking servo is also the voice coil actuator for the excited test mass, so the readout signal, R, indicates the residual length modulation sensed by the servo. The servo suppresses the frequency modulation excitation by actuating on the length of the arm via the voice coil, thus inducing a physical length variation to reduce the effective length variation.

single-arm closed-loop response. For sequential voice coil and frequency modulation excitations at the same frequency, r_l/r_f should be 1.

To assess the precision inherent in the frequency modulation calibration method, we made measurements using the x-arm of the Hanford 4 km interferometer at three widely separated frequencies within the most sensitive region of the LIGO detection band, 91, 511, and 991 Hz. The data for these measurements were recorded by driving the frequency modulations at all three frequencies simultaneously, each with an associated length modulation separated by 0.1 Hz (six excitations total). The calibration results are plotted in figure 4.19. The dashed lines denote a weighted least-squares fit to the data with the expected f^{-2} force-to-length functional form. The error bars show the estimated $\pm 1\sigma$ uncertainties of approximately 0.8%, as described in section 4.4.3.

Deviations from the expected f^{-2} force-to-length functional form can be caused by measurement error or actuation electronics which have frequency-dependence. As described in section 4.3.4, the signal path for the voice coil actuators contains several frequency-dependent electronics that should be compensated so that the transfer function of the entire signal path is frequency-independent so that the voice coil actuators deliver a frequency-independent force to the ETM. Deviations from this design would result in the actuation function having a different functional form instead of the expected f^{-2}. Frequency-dependent variations in the actuation electronics of the order of a few percent over the band of interest have been observed.

4.4.3 Estimate of uncertainties

Expanding equation 4.45, the calibrated voice coil actuation function can be written as,

$$A_l = \left[\frac{-C(f)L}{\nu}\right] 2\mathcal{K}(f)\, H_{mc}(f) \left[\frac{S_f}{S_l}\,\frac{R_l}{R_f}\right] \frac{r_l}{r_f}\,. \tag{4.46}$$

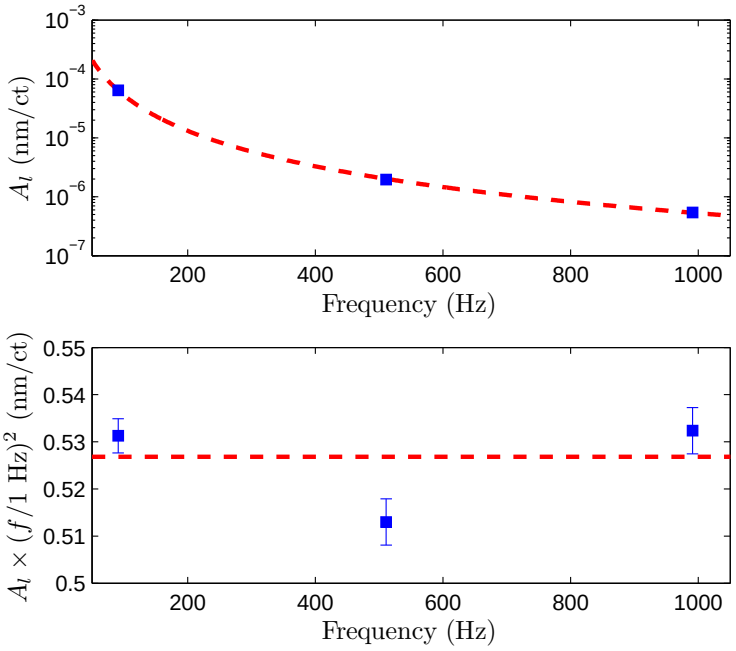

Figure 4.19: ETM voice coil actuation coefficients measured using the frequency modulation technique for the x-arm of the Hanford 4-km-long interferometer. The dashed lines are a weighted least-squares fit with a f^{-2} functional form. In the lower panel, the expected functional dependence is removed by multiplying by the square of the measurement frequency. The error bars represent the estimated $\pm 1\sigma$ uncertainties.

Variable	1σ uncertainty
S_f actuation function, $\mathcal{K}$	0.1% (Statistical)
Mode cleaner filtering, H_{mc}	0.05% ($f_0 \sim 3\%$)
Signal ratio, $(S_f R_l)/(S_l R_f)$ ($N \simeq 35$)	0.8% (Typical)
Control loop response, r_l/r_f	0.05% (Typical)
Estimated overall uncertainty	**0.8%**

Table 4.1: Summary of the significant relative uncertainties contributing to the overall relative uncertainty for the frequency modulation voice coil calibration technique.

The uncertainty in A_l is estimated by calculating partial derivatives of equation 4.46 with respect to variables that have significant uncertainties and summing in quadrature. These estimates are summarized in table 4.1 and discussed below.

The first term in square brackets has negligible uncertainty because both L, and therefore $C(f)$, and ν are known with high accuracy. The relative uncertainty in arm cavity length is of the order of 10^{-4} % and the relative uncertainty in laser frequency is of the order of 0.01%.

The statistical uncertainty in the S_f calibration function, $\mathcal{K}$, is determined using two methods. First, repeated measurements are made at a single frequency; second, measurements are made at multiple frequencies over a span from 90 Hz to 2 kHz (see figure 4.13). Both methods yield a standard error in the calibration function of approximately 0.1%, originating from uncertainty in measuring the sideband-to-carrier power ratio. We have not included estimates of potential sources of systematic error associated with using the spectrum analyzer to measure the sideband and carrier power level ratio, although we expect them to be small. The power levels typically differ by approximately 30 dB at frequencies separated by less than 2 kHz; the maximum frequency difference divided by the mean frequency is less than 3×10^{-5}.

The results of repeated measurements of the mode cleaner pole frequency vary by as much as 3%. However, the contribution of this variation to the overall uncertainty in the actuation coefficient is reduced by a factor of $(f_0^2/f^2 + 1)^{-1}$ due to the partial

derivative of equation 4.46 with respect to f_0. Thus, the contribution to the uncertainty in A_l due to uncertainty in the mode cleaner pole frequency is about 0.05% at 1 kHz and even smaller at lower frequencies.

The last term in square brackets includes the frequency and length excitation amplitudes measured at the monitor points and the measured amplitudes in the single-arm readout signal. For typical measurements, we average 35 successive 4-minute-long Fourier transforms. This reduces the combined standard error for this term to 0.8%, dominated by the uncertainties in measurement of S_f and R_l. The contribution from S_f is large because the monitor point for the frequency excitation is downstream of the summation point for the mode cleaner locking servo. R_l contributes significantly due to the small excitation amplitudes used in order to avoid saturation of the ETM actuation electronics.

For the 0.1 Hz frequency separation used in these measurements, the estimated r_l/r_f ratio differs from unity by less than 0.05%, significantly below measurement statistical variations. This was confirmed experimentally by repeating calibration measurements with the length and frequency modulation excitation frequencies interchanged.

Adding all of these relative uncertainties in quadrature, we estimate the typical fractional 1σ uncertainty in the calibration of the ETM voice coil actuation coefficient to be approximately 0.8%. With longer integration times and more averaging of the measured signals, the overall estimated uncertainty could be further reduced.

4.4.4 Conclusions of the frequency modulation technique

We have described a new technique for calibrating the test mass displacement actuators of the LIGO interferometers that uses frequency modulation of the injected laser light to create an effective length modulation fiducial. We have also described the method employed to measure the amplitude of the applied frequency modulation

and therefore the induced effective length modulation. Procedures used to improve the overall estimated test mass voice coil calibration precision to less than 1% (1σ) have been discussed.

The test mass actuation coefficients determined using this technique are consistent with those derived using two distinctly different methods, the free-swinging Michelson and the photon calibrator (see section 4.6). Unlike both of these methods, the frequency modulation technique does not exert additional forces directly on a test mass. Measurements and finite-element modeling have shown that elastic deformation of the test masses caused by these actuation forces can induce large errors in actuator calibration, especially for actuation frequencies above 1 kHz [19, 37, 42].

For the frequency modulation method, we induce effective arm length displacements on the order of 10^{-13} m which are much smaller than the displacements used for the free-swinging Michelson method ($\sim 10^{-8}$ m), but much larger than those used for the photon calibrator method ($\sim 10^{-17}$ m). In contrast to the free-swinging Michelson method that requires multiple sequential measurements, frequency modulation enables a single-step actuator calibration. However, it uses a single-arm configuration rather than the full *science-mode* configuration in which searches for gravitational waves are performed and the photon calibrator method is applied.

Recent improvements in the single-arm feedback control loop have reduced noise levels. The reduced noise should enable increased calibration precision with shorter integration times using the frequency modulation method. Increasing measurement precision and applying several disparate calibration methods has improved our understanding of systematic errors and increased our confidence in test mass actuator calibration results. Optimizing the scientific reach of future gravitational wave searches will require further improvements in detector calibration accuracy and precision [52]. We expect that the frequency modulation method will continue to play an important role in these efforts.

4.5 Photon calibrator technique

Another voice coil calibration technique, the photon calibrator, can be used in the science-mode interferometer configuration. Much of this section has been published in [37]. Included here are technical details that are beyond the scope of the published article.

Photon calibrators have been implemented at the Glasgow 10-meter prototype detector [25] and the GEO600 detector [62], and they have been under development at LIGO and VIRGO for a long time [23, 34, 75, 76]. The work reported here expands upon previous efforts [25, 42, 62] and addresses dominant systematic uncertainties that can arise from absolute laser power calibration, test mass angular displacement, localized elastic deformations induced by the photon calibrator laser beams, and temporal variations in interferometer signals used to sense displacements. We have demonstrated methods devised to reduce or eliminate these major, and other smaller, uncertainties, reducing the overall voice coil actuator calibration uncertainty to less than 2% (1σ).

A key advantage of photon calibrators is that they can be used while an interferometer is running in the science-mode configuration. Measuring in this configuration eliminates systematic uncertainties that arise in other methods, such as the standard calibration techniques employed during previous LIGO science runs [50], which require different optical and electronic configurations. Photon calibrators can be used either to determine the differential-length sensitivity of the interferometer directly, or to measure the voice coil actuation functions. An additional advantage of photon calibrators is their ability to measure the time delay in the length response of the interferometer [20].

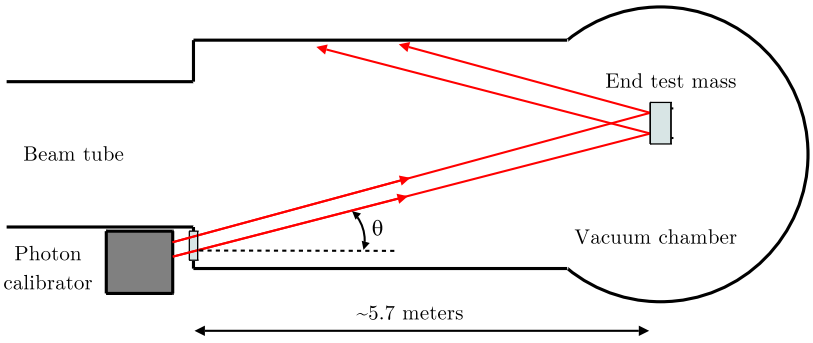

Figure 4.20: Schematic diagram of a LIGO photon calibrator with output beams reflecting from an end test mass inside the vacuum envelope.

4.5.1 Principles of photon calibration

When a beam of photons with time-dependent power $P(t)$ is incident upon the high reflectivity surface of an ETM at an angle of incidence θ (see Figure 4.20), the beam reflects from the surface, transfers momentum from the recoiling photons, and thereby exerts a force on the mirror proportional to the power and the cosine of the angle of incidence. A sinusoidal power modulation can be written as,

$$P(t) = P_0 + P_m \sin(\omega t) \tag{4.47}$$

where P_0 is the average power that is incident on the test mass, P_m is the amplitude of the power modulation, and ω is the angular frequency. The LIGO ETMs are suspended as pendulums with resonances at about 0.75 Hz. When the frequency of the modulated force on the optic is far above the pendulum resonance frequency, the optic is essentially free to move in the horizontal plane. For the photon calibrator, the amplitude of the induced motion, x_m, is given by

$$x_m(\omega) \simeq -\frac{2P_m \cos\theta}{Mc\omega^2} \tag{4.48}$$

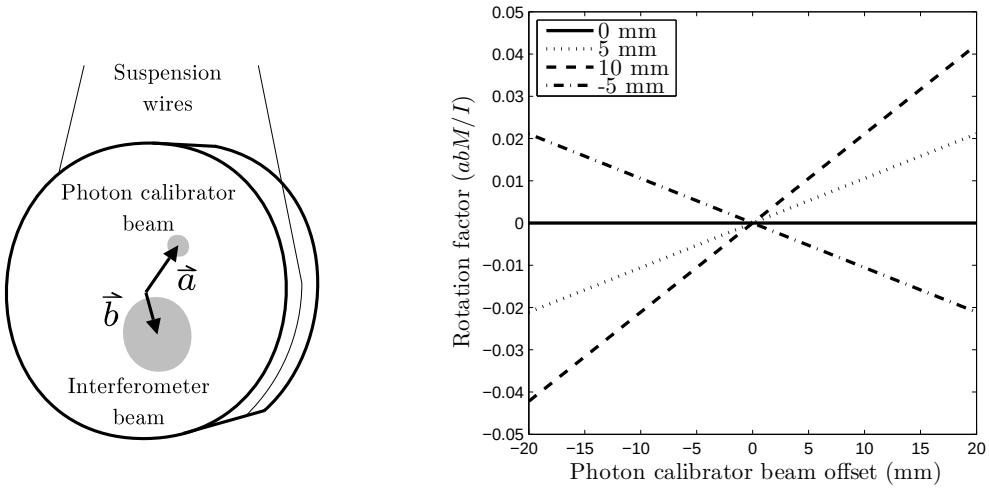

(a) (b)

Figure 4.21: (a) Schematic diagram of a suspended ETM showing the locations of the photon calibrator and interferometer beams, with displacement vectors $\vec{a}$ and $\vec{b}$, respectively. The rotation-induced apparent length variations caused by the photon calibrator and sensed by the interferometer are proportional to $\vec{a} \cdot \vec{b}$. (b) Rotation-induced length change factor versus photon calibrator beam offset for four interferometer beam displacements with $\vec{a} \parallel \vec{b}$.

where M is the mass of the mirror, c is the speed of light, and the minus sign indicates the motion is 180 degrees out of phase with the applied force.

When the applied force is not directed through the center of mass of the optic, the induced torque causes an angular deflection of the test mass. The resonance frequencies for pitch and yaw rotations of the test mass are ∼0.5 Hz. Again, the mirror is essentially free to rotate for modulation frequencies much greater than these resonance frequencies.

Consider a photon calibrator beam that is incident at a point displaced from the center of the face of the optic, given by the displacement vector $\vec{a}$, as shown on the left in Figure 4.21. For small rotation angles, the induced torque is approximately $\vec{\tau} \simeq \vec{a} \times \vec{F}$, where $|\vec{\tau}| = aF$.

The equation of motion for the freely rotating optic is given by

$$I\ddot{\Omega}(\omega,t) = aF(\omega,t) \tag{4.49}$$

where $\ddot{\Omega}$ is the angular acceleration. The optic is approximated as a right circular cylinder[4] with the moment of inertia about an axis through the center of the mass and parallel to the face of the optic given by $I = Mh^2/12 + Mr^2/4$, where M is the mass, h is the thickness, and r is the radius of the optic. For frequencies much greater than the rotational resonance frequencies, the modulated laser power induces a variation of the angle about the center of mass with amplitude given by

$$\Omega(\omega) \simeq -\frac{2aP_m\cos\theta}{Ic\omega^2}\,. \tag{4.50}$$

If the interferometer beam is not centered, then the interferometer senses an apparent length change due to the rotation of the mass. For small angles of rotation, the effective length change, x_{rot}, is given by

$$x_{rot}(\omega) \simeq -\frac{2P_m\cos\theta}{Ic\omega^2}\,\vec{a}\cdot\vec{b} \tag{4.51}$$

where $\vec{b}$ is the displacement vector of the center of the interferometer beam on the mirror's surface.

The effective length change due to the rotating mass adds or subtracts to the longitudinal length change, depending on the sign of $\vec{a}\cdot\vec{b}$. Thus, the total sensed motion due to the photon calibrator actuation is given by

$$x_{tot}(\omega) \simeq -\frac{2P_m\cos\theta}{Mc\omega^2}\left(1+\frac{M}{I}\,\vec{a}\cdot\vec{b}\right)\,. \tag{4.52}$$

[4]The rear surface of the optic is actually wedged at 2 degrees. The maximum change in the rotational moment of inertia is approximately 0.2% and is included as an offset of 1.4 mm in the vertical beam centering of the photon calibrator beams. Since the change in the moment of inertia is small, the right circular cylinder approximation is used in the analysis of rotational effect uncertainties.

The factor $\vec{a}\cdot\vec{b}M/I$ for a LIGO ETM is plotted in the right-hand plot of Figure 4.21 as a function of photon calibrator beam offset for various interferometer beam offsets. In this figure, the photon calibrator beam displacement is parallel to the interferometer beam displacement. For a photon calibrator beam offset by 10 mm in the same direction as an interferometer beam offset of 5 mm, the sensed length change due to rotation adds 1% to the total motion.

Hild et al. showed that localized elastic deformation of the test mass surface due to photon calibrator radiation pressure can significantly change the amplitude of the sensed length modulation [42]. The free-mass motion falls as f^{-2}, but the elastic deformation is approximately frequency-independent for frequencies far below the test mass internal mode frequencies. The lowest internal mode frequency is approximately 6 kHz. At several kHz, the amplitudes of the free-mass motion and the elastic deformation are comparable (see Figure 4.22). The free-mass motion is 180 degrees out of phase with the force applied to the optic while the elastic deformation is in phase with the force applied. The amplitude of the sensed elastic deformation is strongly dependent on the overlap of the photon calibrator beam with the interferometer beam, and, to a lesser extent, the spatial intensity profiles of the beams and the specific shape and composition of the test mass. The interferometer is maximally sensitive to the elastic deformation caused by the photon calibrator when the interferometer and photon calibrator beam centroids are co-located on the face of the optic, while the effect is minimized when the beams do not overlap. Even at lower frequencies, the elastic deformation can contribute significantly to the sensed motion when the beams are closely located. If not properly accounted for, this introduces a frequency-dependent systematic error in the voice coil actuator calibration. For example, measurements performed using a single-beam photon calibrator (presented in Section 4.5.3) show that when the photon calibrator and interferometer beams are centered on the optic, the total sensed motion at 1 kHz is 10% smaller than the ex-

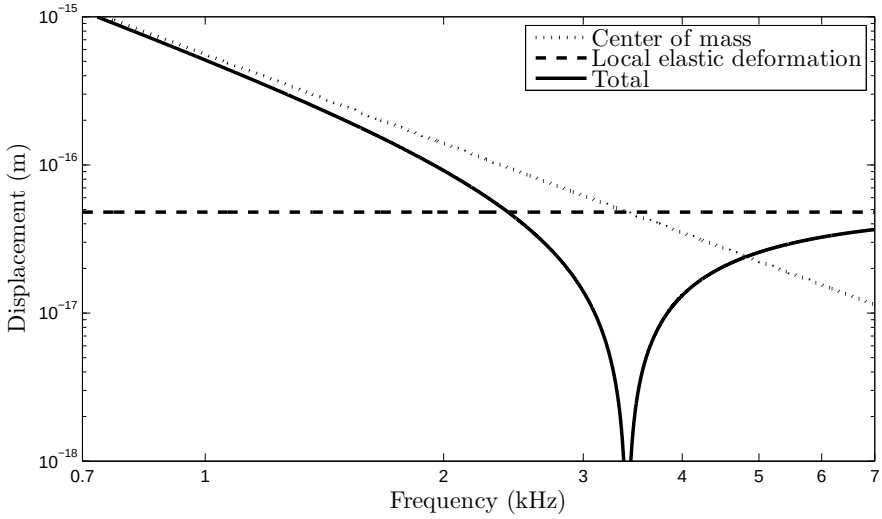

Figure 4.22: The bulk displacement of the test mass as a function of frequency for a free mass (dotted line) falls as f^{-2}, the frequency-independent local elastic deformation (dashed line) 180 degrees out of phase with the bulk displacement, and the total surface motion (solid line) sensed by the interferometer. This is the same functional form as described by Hild, et al. The relative amplitude of these terms is taken from measurements in Section 4.5.3.

pected free-mass displacement, and indicate that near 3.4 kHz the elastic deformation of the surface is comparable to the free-mass motion (see Figure 4.22). Uncertainties in determining the beam positions can lead to significant errors in predicting the interferometer sensing of the elastic deformation.

To minimize the local elastic deformation effect, one can simply move the photon calibrator beam away from the region of the optic that the interferometer beam is sensing, typically the center of the optic. However, as previously discussed, the resulting torques would lead to undesired angular displacements. We instead use two beams, balanced in power and displaced symmetrically about the center of the face of the optic.

When using two laser beams, however, the ratio of powers of the beams becomes

important. For two beams, the effective beam position can be described by

$$\vec{a}_{eff} = \frac{\alpha\,\vec{a}_1 + \vec{a}_2}{\alpha + 1} \tag{4.53}$$

where the photon calibrator beam positions are $\vec{a}_1$ and $\vec{a}_2$ and the ratio of beam powers is $\alpha = P_1/P_2$. In practice, beam powers are adjusted such that $|1 - \alpha| \leq 0.02$ and the beams are positioned such that $\vec{a}_2 = -\vec{a}_1$. Thus, $\vec{a}_{eff} = \vec{a}_1(\alpha - 1)/(\alpha + 1)$, which is typically less than $0.01 \times \vec{a}_1$.

4.5.2 Experimental setup

Photon calibrators have been installed on each of the three LIGO interferometers, one to actuate each ETM. A schematic of a photon calibrator optical breadboard is shown in Figure 4.23. The horizontally polarized output of an optically-pumped Nd^{3+}:YLF laser operating at a wavelength of 1047 nm is directed through a polarizing beamsplitter and is focused into an acousto-optic modulator that diffracts a fraction of the laser power that varies in response to the modulation input signal. The first-order diffracted beam is collimated and a sample is directed to a high-bandwidth, large-area germanium photodetector that provides a continuous monitor of the modulated laser power. The remaining beam is divided equally into two beams which are directed to the ETM[5].

The optical breadboard is mounted on a platform outside of the vacuum enclosure. The photon calibrator beams enter the vacuum envelope through a glass viewport and impinge on the ETM as shown schematically in Figure 4.20. The ETM is 25 cm in diameter, 10 cm thick, and has a mass of approximately 10.3 kg. The photon calibrator beams are displaced symmetrically by about 8 cm to either side of the center of the high reflectivity surface of the mirror. The interferometer spot size (radius) is

[5]The original layout for the LIGO photon calibrators was a single-beam configuration aligned to the center of the test mass to avoid large systematic errors due to rotation of the optic. They were converted to the two-beam configuration to avoid sensing the induced local elastic deformation.

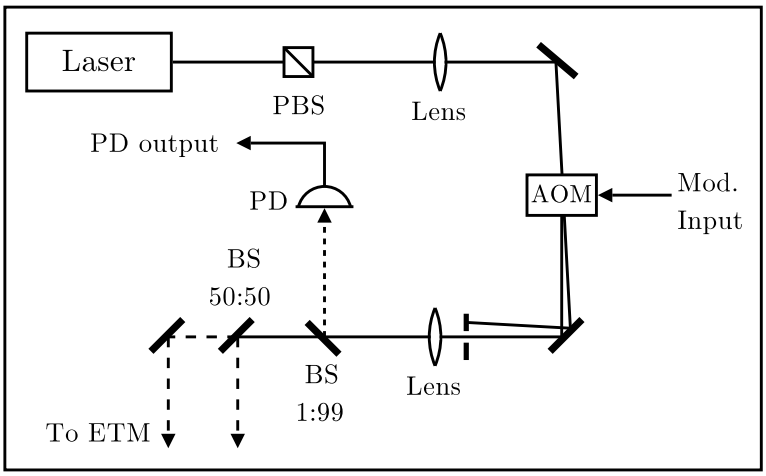

Figure 4.23: Schematic diagram of the photon calibrator optical layout. PBS: polarizing beamsplitter, AOM: acousto-optic modulator, BS: beamsplitter, and PD: photodetector

about 3.4 cm. The angle of incidence of the two beams is approximately 9.6 degrees. The spot sizes (radii) of the two beams at the ETM surface are approximately 2 mm, and the average power of each beam is approximately 100 mW. The typical amplitude of the sinusoidally-modulated power in each beam is about 50 mW.

The positions of the photon calibrator beam spots are determined by observing the beams' scattered light on the ETM surfaces, using cameras mounted on other vacuum viewports. Accounting for parallax and refraction, alignment fiducials are provided by light emitting diodes (LEDs) used for mirror positioning, which emit light from apertures located close to the back surfaces of the optics. These fiducials are also used to determine the position of the interferometer spot on the face of the optic when operating in the science-mode configuration.

The photodetector that monitors the laser power is calibrated to indicate the laser power directed toward the vacuum window as a function of the voltage measured by the photodetector. To calibrate the photodetector, a power sensor that consists of an integrating sphere with a temperature controlled InGaAs photodetector and high-bandwidth current amplifier (working standard) is first calibrated against a sec-

ond, identical power sensor (gold standard) which was sent to the National Institute of Standards and Technology (NIST) for absolute power calibration using 1047 nm Nd^{3+}:YLF laser light [38]. Then, the working standard is used to measure the power exiting the photon calibrator. The optical efficiencies from incidence on the viewports to reflections from the ETMs were measured when the vacuum enclosures were open. For one ETM, for example, the overall optical efficiency is 90.7%. The viewport transmits 90.8% of the incident light and the ETM reflectivity is 99.9%. The laser power reflecting from the ETM can be continuously monitored by computing the product of the photodetector signal with the overall optical efficiency coefficient. The uncertainty in the absolute power calibration is discussed in Section 4.5.4.

4.5.3 Measurements and results

To determine the voice coil actuation function, A_l, for an ETM, the photon calibrator and the voice coil actuators sinusoidally actuate the position of the optic while the interferometer is operating in the science-mode configuration. By driving both actuators simultaneously, systematic errors induced by time-varying interferometer parameters, such as optical gain, are minimized. The sine wave frequencies are separated by 0.1 Hz, close enough to minimize interferometer response function variations, but far enough apart to minimize either signal contaminating the other due to leakage in the amplitude spectral density (ASD) calculation.

Each actuation is detected by the interferometer as a length modulation, and the signal appears as a peak above noise in the ASD of the error signal of the DARM servo loop. During the measurement, the peak in the ASD of the photon calibrator photodetector output and the peak in the ASD of the digital excitation signal sent to the voice coil actuator are also measured. The transfer coefficient magnitude is calculated from each ratio of error signal peak to excitation channel peak. Dividing the two transfer coefficients relates the digital excitation of the voice coils to the

Parameter	H1 x	H1 y	H2 x	H2 y	L1 x	L1 y
M (kg)	10.338	10.380	10.372	10.363	10.34	10.36
Optical eff.	0.907	0.980	0.973	0.967	0.919	0.930
θ (deg.)	10.1	9.2	9.6	9.4	9.5	9.2
$\vec{a}_{eff}$ (mm)	(0.0,-1.4)	(0.0,-1.4)	(1.5,1.6)	(0.3,-1.0)	(0.0,-1.4)	(0.0,-1.4)
$\vec{b}$ (mm)	(1.5,1.2)	(-1.8,0.3)	(7.8,1.5)	(-3.0,-3.2)	(0.0,0.0)	(0.0,0.0)

Table 4.2: Summary of photon calibrator parameters used for measurements made following S5.

photon calibrator photodetector signal. The ETM voice coil actuation function is calculated using the previously obtained calibration of the photodetector, the mass of the ETM, the angle of incidence of the photon calibrator laser beams, the viewport transmission, the ETM reflectivity, the frequency of modulation, and the positions of the photon calibrator and interferometer laser beams on the ETM surface (see table 4.2). The 0.1 Hz separation in frequency of the actuations requires a small correction ($< 0.1\%$) for the frequency-dependent responses of the interferometer and the force-to-length actuation function.

The Hanford 4 km interferometer (H1) x-arm ETM voice coil actuation function has been measured at several frequencies between 90 Hz and 1 kHz, and the results are shown in the upper panel of Figure 4.24. At these frequencies, the ETM is essentially free to move in the longitudinal direction, so the force-to-length actuation function is expected to fall as f^{-2}. For comparison with this expected actuation function, the data are multiplied by the square of the measurement frequencies and plotted in the lower panel of Figure 4.24 with their associated $\pm 1\sigma$ error bars (see Section 4.5.4). A free-mass response would appear as a horizontal line in this plot. The peak-to-peak variation in these data is less than 3.7%.

The influence of local elastic deformation for a single, centered photon calibrator beam is shown by the data in the left-hand plot of Figure 4.25. Data from the single-beam H1 y-arm photon calibrator are shown for frequencies between 91 Hz and 2.1

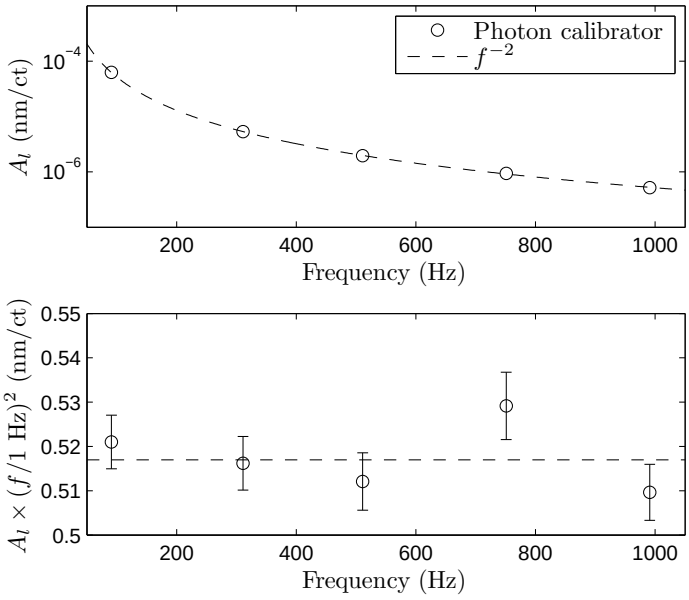

Figure 4.24: H1 x-arm ETM voice coil actuation function measured with the photon calibrator versus frequency (upper panel). The dashed line indicates the expected f^{-2} behavior. In the lower panel, the measured actuation function values are multiplied by the square of the measurement frequency. The error bars indicate the estimated $\pm 1\sigma$ uncertainties.

kHz. The beam is centered on the test mass and overlaps the main interferometer beam. A chi-square fit to these data using the same functional form as Hild, et al. [42] is calculated from the data and their associated uncertainties. The model has two parameters, one for an idealized actuation function for a free mass falling as f^{-2}, and one for a frequency-independent deformation of the mirror surface that is 180 degrees out of phase with the free-mass motion. The calculated fit parameters are $5.58 \pm 0.04 \times 10^{-10}\,(1\,\mathrm{Hz}/f)^2$ m/count for the free-mass response and $4.8 \pm 0.2 \times 10^{-17}$ m/count for the frequency-independent contribution of the surface elastic deformation to the sensed motion. The longitudinal displacement of the region of the optical surface sensed by the interferometer beam is thus less than the expected free-mass motion. If not accounted for, this results in a systematic error in the voice coil calibration that increases with frequency, as shown in Figure 4.22. For the H1 y-arm configuration, the discrepancy is approximately 60% at 2091 Hz (see Figure 4.25).

Data for the Hanford 2 km interferometer (H2) x-arm photon calibrator using two beams symmetrically displaced from the center of the ETM are shown in the right-hand plot of Figure 4.25. In this configuration, the expected f^{-2} response (frequency-independent in this plot) is observed because the local elastic deformations caused by the photon calibrator beams are outside the region sensed by the interferometer beam. To confirm this, the two beams were aligned to the center of the optic, overlapping each other and the interferometer beam, and the voice coil actuation function was again measured at 1691 Hz. The actuation function increased by about 45% because the motion sensed by the interferometer is reduced due to the combined effect of the photon calibrator induced displacement and the elastic deformation of the optical surface. For the two-beam configuration measurements on H2, the voice coil actuation function has a peak-to-peak variation of 3.6% about an idealized free-mass actuation function.

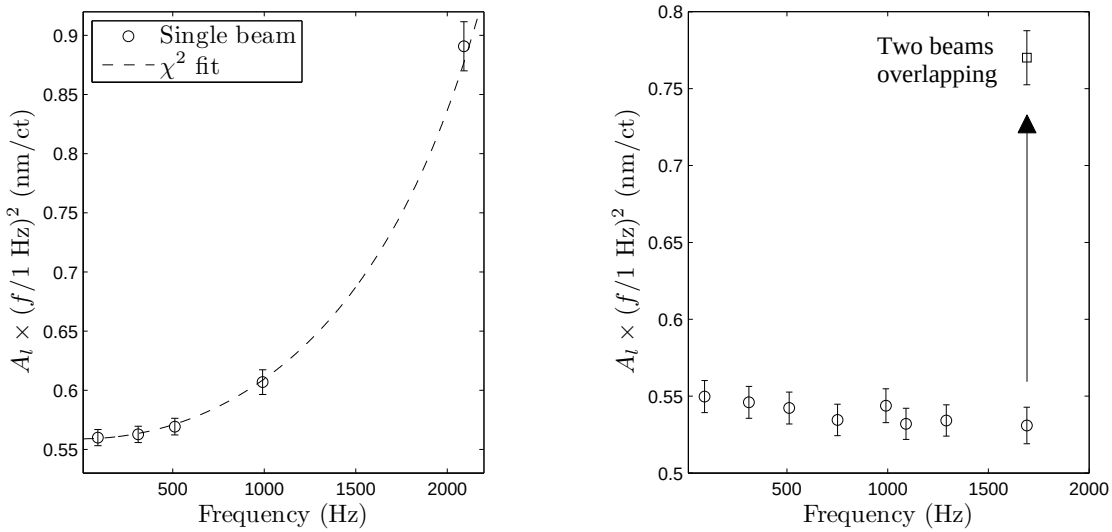

Figure 4.25: Left panel: data from the single-beam, centered H1 y-arm photon calibrator with the χ^2 fit to the data. Right panel: data from the two-beam H2 x-arm photon calibrator in two different configurations. First, with the beams are in their nominal positions, diametrically opposed about the center of the face of the optic, and, second, with the two beams overlapping with the interferometer beam at the center of the ETM surface. The error bars indicate the estimated $\pm 1\sigma$ uncertainties.

Variable	1σ uncertainty
Rotation, $(1 + \vec{a} \cdot \vec{b}M/I)$	1.0%
Power coefficient, P_m	0.7%
Statistical ($N \simeq 100$)	0.25% (Typical)
Angle cosine, $\cos\theta$	0.1%
Mass of ETM, M	0.1%
Total error	**1.3%**

Table 4.3: Summary of the significant photon calibrator uncertainties for the H1 x-arm ETM voice coil calibration. Note that systematic errors arising from effects associated with test mass deformations have not been included.

4.5.4 Estimated uncertainties

There are a number of potential sources of both statistical and systematic uncertainty that can impact the overall accuracy and precision of the voice coil actuation function derived from the measurements with the photon calibrators. We describe these sources below and summarize their respective estimated uncertainties in Table 4.3.

A potentially large source of systematic uncertainty is the absolute power calibration of the photon calibrator's internal photodetector. The calibrated photodetector signal indicates the laser power directed toward the vacuum enclosure window. The estimated overall uncertainty in its calibration is 0.56% including contributions from several sources added in quadrature. The photodetector calibration relies on the absolute calibration, performed by NIST, of the gold standard power measurement system. The NIST calibration carries a 1σ uncertainty of 0.44%[6] [38]. To assess the variability in transferring the NIST calibration of the gold standard to the working standard, we repeated a detailed calibration procedure 25 times. The 1σ variation of the derived working standard calibration coefficients was 0.21%. The uncertainty introduced by variations in the positioning of the integrating sphere aperture relative to the incident laser beam was assessed by successive repositioning of the integrat-

[6]Calibrations repeated yearly will indicate the long-term stability of the gold standard calibration.

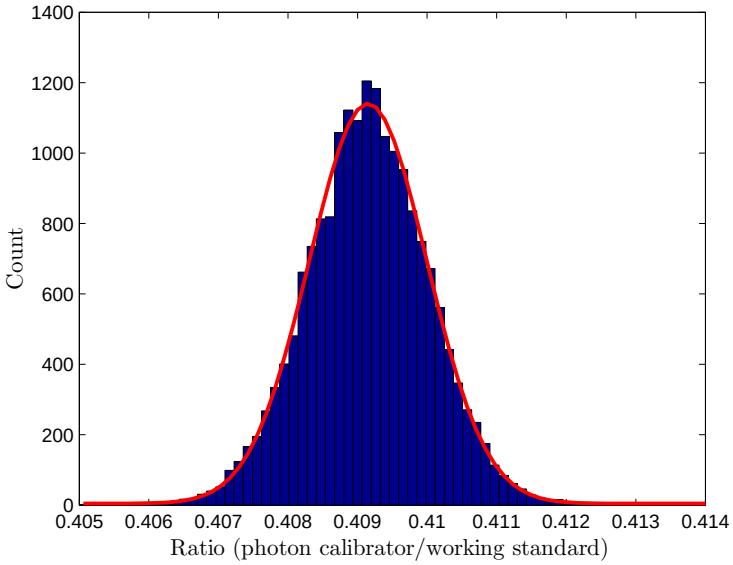

Figure 4.26: Histogram ratio of one-minute averaged photon calibrator photodetector output compared with the one-minute average of the working standard integrating sphere placed in the output laser beam of the photon calibrator. The red line indicates a fit of the histogram data to a Gaussian function.

ing sphere assembly. The 1σ variation of these measurements was 0.18%. Temporal variations in the calculated calibration of the internal photodetector were investigated by positioning the working standard in an installed photon calibrator output beam and simultaneously recording its output and the output of the internal photodetector over a two-week period (see figure 4.26). The 1σ variation of the ratio of the outputs, calculated via the 1-minute averaged output signals over two weeks was 0.22%. Adding these four contributions in quadrature gives the overall estimated uncertainty of 0.56% in the calibration of the internal photodetector in terms of the absolute power directed toward the vacuum viewport [32].

Measurements of the viewport transmission and ETM reflection coefficients were made with the working standard when the ETM vacuum enclosure was open. Measurements were made, both inside and outside the vacuum enclosure. These are relative measurements, so the working standard calibration uncertainty does not en-

ter into these measurements. From these measurements, the estimated 1σ relative uncertainty in the overall optical efficiency is 0.40%. Combining in quadrature with the calibration of the photon calibrator photodetector gives a 1σ uncertainty of 0.69% in the absolute power reflecting from the ETM surface.

The position of the photon calibrator beams on the ETM surface can also be a major source of uncertainty when calculating rotation-induced length changes. First, an image is recorded of the optic's surface showing the relative locations of the photon calibrator beams and the LEDs located behind the optic. Then, using the LED spots as fiducials, the positions of the photon calibrator beams are determined using image processing software, taking into account refraction and parallax. The measurements are made several times and an average value is calculated. With this technique, the positions of the photon calibrator beams on the ETM surface are determined to within ± 5 mm. The location of the larger interferometer beam is known to within ± 10 mm. The uncertainty due to the rotation-induced length change is calculated for positions mis-measured by 5 mm and 10 mm for the photon calibrator and interferometer beams, respectively, the worst-case scenario. Additionally, for photon calibrators with two beams, a power imbalance ratio of 2% has been incorporated into the uncertainty estimate because this variation would effect the torque applied to the mirror. In total, the resulting estimated 1σ value is typically 1.0%. The uncertainty scales with the nominal locations of the photon calibrator and interferometer laser beams on the ETM surface.

The ETM mass was first calculated from the dimensions of the ETM and the density of the ETM substrate material. The masses of four ETMs (the x- and y-arms of H1 and the Livingston 4 km interferometer, L1) were measured using calibrated scales. The maximum discrepancy between the measured and calculated values is less than 20 grams. We use a rectangular window of 0.2% for the ETM mass that results in an estimated 1σ uncertainty of about 0.1%.

There are well constrained limits on the angle of incidence due to the physical constraints of the LIGO vacuum chamber assembly. The location of each photon calibrator beam spot on the viewport window is known to within 6 mm. The angle of the beams from the viewport spot location to the ETM spot location is determined from as-built technical drawings of the vacuum enclosure and the ETM placement. Calculations allow for a variation of 6 cm in the position of the ETM along the beam tube axis and 3 cm perpendicular to the beam tube axis, relative to the as-built technical drawings. Under these considerations, the cosine of the angle of incidence has a 1σ uncertainty of 0.1%.

Due to fluctuations of the optical gain of the interferometer, the interferometer differential-length sensitivity varies slightly as a function of time. These fluctuations induce a 1σ uncertainty of only 0.01% in the voice coil actuator calibration because the peaks in the DARM servo error signal are measured simultaneously and are separated in frequency by only 0.1 Hz.

The statistical error in the overall calibration has been estimated from the standard deviation of multiple measurements of the ratio of the peaks in the DARM servo loop error signal to the peaks in the excitation monitor signals. From these measurements, the standard error is estimated to be 0.25%. At low frequencies, fewer measurements were required to obtain a standard error at this level, while at higher frequencies more measurements were required. The statistical uncertainty is frequency dependent since the motion induced by the photon calibrator falls as f^{-2} and the differential-length sensitivity is decreasing as f^{-1} above roughly 200 Hz. A typical number of measurements to obtain this level of precision is $N \simeq 100$ between 90 Hz and 1 kHz for integration times of 128 seconds.

Combining estimates of both systematic and statistical uncertainties, the total estimated 1σ uncertainty in the calibration of the voice coil actuators is 1.3%, indicative of the accuracy achievable with the photon calibrator. With increased precision

in the localization of the photon calibrator and interferometer beams on the ETM surface, the overall uncertainty could be reduced below 1%.

This uncertainty estimate does not include contributions that arise from elastic deformation of the test mass by the photon calibrator forces. Finite-element analysis of the motion of the optical surface in response to dynamic external forces is ongoing. [19, 80] Preliminary results suggest that at frequencies above a few kHz bulk deformation of the test mass significantly changes the motion sensed by the interferometer beam. As the excitation frequency increases, there is a dramatic increase in the discrepancy between the free-mass motion, which is falling as f^{-2}, and the deformation-induced motion, which is increasing as the internal mode resonance frequencies are approached. For the measurements presented here, errors due to bulk deformation appear to be less than 1%. We thus estimate that the total photon calibrator uncertainty, including errors due to bulk elastic deformation, could be as high as 2% at the highest frequencies. Careful modeling may enable correcting for bulk deformation caused by the photon calibrator, but significant uncertainties may remain due to uncertainties in determining beam positions.

4.5.5 Photon calibrator conclusions and outlook

We have implemented high-precision photon calibrators on the LIGO detectors and used them to measure the ETM voice coil actuation functions at frequencies from 90 Hz to 2.1 kHz. Measurements made in both single- and two-beam configurations have confirmed the importance of the local elastic deformation of the mirror surface induced by the photon calibrator beams predicted by Hild, et al. The two-beam configuration has been shown to sufficiently minimize the calibration errors caused by this effect. We have considered mirror rotation induced by non-centered photon calibrator beams and derived expressions for the sensed longitudinal motion as a function of the product of the interferometer and photon calibrator beam offsets and

the effective beam position if the power is unbalanced when using a two-beam photon calibrator.

Estimated measurement uncertainties have been reduced to approximately 1.3% (1σ) by incorporating several improvements. These include accounting for rotation-induced apparent length variations, accurate power measurement, using a two-beam photon calibrator configuration, and exciting simultaneously at closely spaced frequencies. Other potential sources of systematic errors were reduced by careful measurement of the transmission of the vacuum windows, the reflectivity of the test masses, the angles of incidence on the mirrors, the positions of the interferometer and photon calibrator beams, and the masses of the ETMs. Statistical errors were reduced by multiple averages of power spectral densities calculated from long-duration time series.

Frequency-dependent variations in the actuation path electronics and test mass deformations induced by the voice coil forces can cause the actuation function to deviate from the expected f^{-2} force-to-length response of a free mass. However, the data presented in Figure 4.24 indicate that the peak-to-peak deviation is less than 3.7% over the frequency range from 90 Hz to 1 kHz. Finite-element modeling of test mass deformations due to the applied photon calibrator forces should facilitate correction for deformation-induced systematic errors, significant at frequencies above a few kHz, enabling investigation of test mass actuation functions at even higher frequencies.

One of the key advantages of the photon calibrator is its ability to operate in the most sensitive science-mode configuration. It is capable of introducing calibrated differential length displacements using an actuator that is outside the closed DARM control loop and thus enabling both calibration of the in-loop actuators and direct calibration of the monitor point sensitive to gravitational waves, the DARM servo error point. This capability, together with their demonstrated levels of precision

and accuracy, makes photon calibrators a prime candidate for calibration of future gravitational wave detectors that will utilize more sophisticated test mass suspensions with more complex actuation chains.

4.6 Comparison of the calibration techniques

This section is based upon a published article comparing the results of the three voice coil calibration techniques [36]. The measurements reported here were performed at the LIGO Hanford Observatory (LHO) during a period dedicated to calibration-related activities at the end of the S5 science run [13] in October and November of 2007. Two interferometers were operating at LHO, the H1 interferometer with 4-km-long arm cavities and the H2 interferometer with 2-km-long arms. The photon calibrators for three of the four ETMs had already been converted to two-beam configurations. Only the H1 y-arm system was still in a one-beam configuration with the beam centered on the ETM.

The photon calibrator and frequency modulation measurements were similar in that they were made at a few discrete frequencies. Long integration times ($\geq$128 seconds) and multiple averages enabled assessment of the statistics for the measurements and reduction of the standard errors. On the other hand, swept-sine measurements with approximately fifty measurement frequencies between 90 Hz and 1 kHz were used for the free-swinging Michelson technique. This is not a fundamental requirement for this method, rather it is the type of measurement found to be most useful for estimating the actuation function over the relevant band of frequencies. We thus compare swept-sine measurements for the free-swinging Michelson method with single-frequency measurements at a few discrete frequencies for the other two methods.

The results of measurements carried out with all three techniques are plotted together in figure 4.27. For each datum, the calculated actuation coefficient is mul-

tiplied by the square of the measurement frequency to facilitate comparison with a simple f^{-2} functional dependence. The free-swinging Michelson data, plotted without error estimates, are from two separate calibration sequences that were carried out on consecutive days. For better visibility, the error bars for the photon calibrator and frequency modulation data are $\pm 3\sigma$ estimates of statistical uncertainties only, with σ a representative standard error for the averaged measurements. Estimates of systematic uncertainties for each calibration method [35, 37, 49] have intentionally been omitted so that the overall systematic uncertainty can be evaluated by comparing the results of the three methods with statistical precision indicated by the error bars, or the scatter in the data for the free-swinging Michelson results. For each ETM, the dashed horizontal lines indicate the simple mean value for the free-swinging Michelson method and the weighted mean values for the photon calibrator and frequency modulation methods. All data are normalized to the average of the mean values for the three methods, $\overline{A}_l$. The H1 y-arm photon calibrator is in a single-beam configuration, therefore local elastic deformation caused by the photon calibrator forces and sensed by the interferometer beam causes the overall actuation function to rise dramatically with increasing frequency [37]. We thus fit a curve with the functional form predicted by Hild, et al. [42] to the data in figure 4.27 instead of averaging over frequencies. The low frequency asymptote is the actuation coefficient we would expect for a two-beam photon calibrator operating on this mass.

The data for all three measurement methods exhibit variations with frequency that appear to be inconsistent with a simple f^{-2} frequency dependence. This is likely due to either frequency-dependent systematic errors in the calibration methods or frequency-dependent variations in the actuation path electronics in Run mode. For the free-swinging Michelson data, the sensing function and errors in making the Run/Acquire correction can also introduce frequency-dependent variations.

Potential sources of systematic errors for the free-swinging Michelson technique

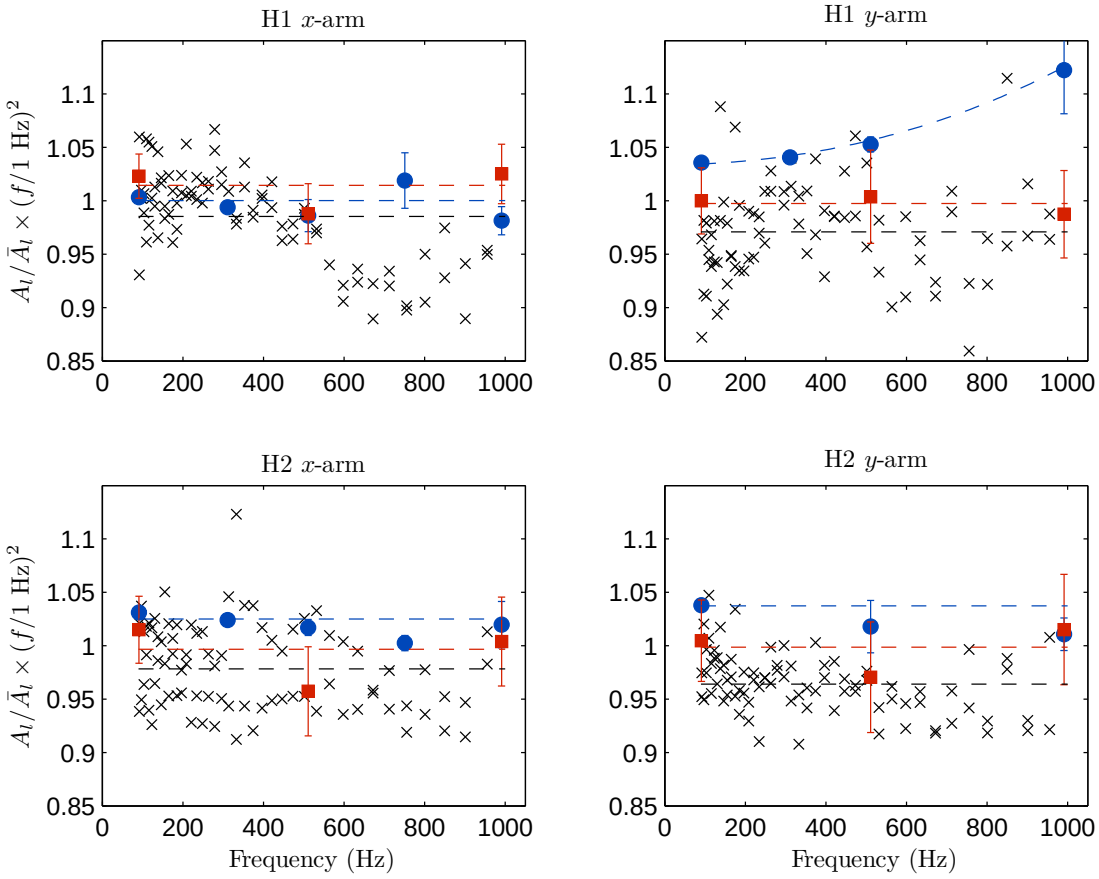

Figure 4.27: Comparison of ETM actuation coefficients measured with three techniques: free-swinging Michelson (black crosses), photon calibrator (blue circles), and frequency modulation (red squares). The data are multiplied by the square of the measurement frequency and normalized to the average of the three weighted mean values (dashed horizontal lines) for each method, $\overline{A}_l$. The free-swinging Michelson data are plotted without error bars; for visibility, 3σ statistical error bars are plotted for the other two methods. The single-beam H1 y-arm photon calibrator data show the influence of local elastic deformation by photon radiation pressure.

include time-dependent alignment variations during sequential measurements, measuring in different interferometer and electronics configurations, and extrapolation over nearly 12 orders of magnitude in actuation range. Overall systematic uncertainty, estimated from the observed spread in the data and from propagating errors through the many steps of the technique, is approximately 10% [49]. The primary identified sources of systematic uncertainty for the photon calibrator method are rotation due to beam centering offsets and absolute power calibration. With reasonable centering tolerances and the demonstrated power calibration accuracy, the estimated total systematic uncertainty can be reduced to the order of 1% [37]. For the frequency modulation method, the dominant sources of potential systematic errors are the calibration of the VCO which relies on accurate measurement of the sideband-to-carrier ratios and extrapolation over approximately 5 orders of magnitude in actuation range. In practice, the overall estimated uncertainty for this method due to known sources of systematic errors can also be reduced to the 1% level [35].

All calculated actuation coefficients–for all frequencies, for all masses, and for all three techniques–fall within the ±15% ranges plotted in figure 4.27. The maximum difference between the mean values over all frequencies of any two methods for any ETM is less than 8%. The maximum difference between the mean value for any method and the average of the mean values for all three methods, $\overline{A}_l$, for any ETM, is 3.7%; the standard deviation of the twelve differences with respect to $\overline{A}_l$ (all four ETMs) is 2.4%.

4.7 Conclusions and outlook

Errors in the measurement of the actuation functions directly translate into errors in the inferred responses of the LIGO detectors to length variations. Potential errors in the determination of the actuation functions have been the principal concern regarding overall detector amplitude calibration uncertainty. We have presented the results

of measurements made to compare three intrinsically different test mass actuator calibration methods in order to bound potential systematic errors in the free-swinging Michelson method, the main calibration technique traditionally used by LIGO. The observed level of consistency, in light of the differences in the techniques–from fitting interference fringes in a Michelson configuration to photon pressure actuation to laser frequency modulation, in the methods of application–from Michelson and single-arm configurations to the fully-locked configuration used during gravitational wave searches, and in the range of actuation–from 10^{-8} m to 10^{-18} m, indicates that the actual voice coil actuation functions are within the bounds of these measurement results. This, together with the independent measurement of detector displacement sensitivity afforded by the photon calibrator, gives us confidence that the LIGO detector calibration is within the stated uncertainty estimates. For the S5 science run, the estimated 1σ uncertainties for each of the LIGO interferometer's frequency independent combined actuation coefficients (root-mean-square uncertainty of each interferometer's two ETMs) determined using the free-swinging Michelson technique is 5.4% for H1, 5.8% for H2, and 12.2% for L1 [49].

As we have described above, calibration of the displacement actuators of an interferometric gravitational wave detector can be a tedious and complicated enterprise. Future gravitational wave detectors will have even more sophisticated actuation and readout chains. With optimal signal extraction requiring overall calibration accuracies of 1% in amplitude, plus constraints on phase and timing, continued improvement of calibration methods and procedures will be imperative[7]. For instance, ongoing finite-element modeling of actuation forces interacting with LIGO-style test masses indicates that calibration at the 1% level will require correcting for the bulk deformation induced by the actuation forces. This is particularly relevant at frequencies near

[7]Actuator calibration is just one part of the overall interferometer calibration process that includes, for instance, accounting for changes in interferometer operating parameters such as optical gain and generation of time domain calibration functions from frequency domain models. These additional steps expand the overall calibration uncertainty as described in [49, 50].

and above 1 kHz. Techniques such as the photon calibrator, or novel concepts such as a gravity calibrator [41] or dynamic gravity field generator [57], that can provide on-line calibration of the DARM readout signal during gravitational wave searches will be particularly attractive. Multiple parallel calibration efforts will likely be required to achieve these goals. These results have demonstrated the benefits of employing several different methods to search for and mitigate potential sources of systematic errors. The need for precise and accurate on-line calibration dictates that calibration requirements must be an integral part of the design of gravitational-wave detectors to achieve their full scientific potential.

CHAPTER V

An all-sky search algorithm for spinning neutron stars in binary systems

5.1 Introduction

Searches for neutron stars emitting quasi-monochromatic, continuous gravitational waves using LIGO, Virgo, GEO600 or TAMA data have been underway for roughly 10 years. Broadly speaking, there are three different approaches to search for these types of gravitational wave signals. First, a known neutron star with well understood signal parameters can be searched for using a targeted method [3, 5, 7, 15]. Second, a search over a particular sky location that contains possible candidates for gravitational wave signals (e.g. the galactic center or globular clusters) are targeted by algorithms to search over a range of parameters with sensitive search algorithms, examining only one sky location. Unfortunately, these algorithms are computationally costly and cannot be used to search over the entire sky for unknown sources. The third approach attempts to cover a wide region of parameter space, over the entire sky, by using computationally efficient search algorithms. However, these methods are intrinsically less sensitive than the targeted search algorithms, but are able to target unknown isolated sources of continuous gravitational waves [4, 8, 10–12].

The current all-sky search algorithms are not designed to search for unknown

neutron stars in a binary systems. The continuous gravitational wave signal from a source in a binary system is frequency-modulated by the motion of the source in the binary orbit. In order to search for such a source using the current all-sky algorithms, the parameter space for each of the five (non-relativistic) binary orbital parameters must be searched over [30]. The current methods cannot cope with the increased computational cost by adding these parameters because they are already computationally limited. We must therefore find alternative methods to reduce the dimensionality of the parameter space.

The most sensitive search techniques are employed when the neutron star spin parameters and binary orbital parameters are well constrained. When some source parameters are not well constrained, however, then other techniques must be used. For example, while several binary orbital parameters of the Low Mass X-ray Binary (LMXB) Scorpious X-1 (Sco X-1) have been determined, the spin frequency of the neutron star is unknown. This unknown parameter prevents the current targeted search routines from beating the torque balance limit–an assumption that all rotational energy that is lost by the neutron star is converted into gravitational radiation balances the torque imparted to the star by the infalling matter. In order to search for a continuous gravitational wave signal from Sco X-1, new targeted search methods are under development [58, 71].

The search for unknown spinning neutron stars in binary systems requires new search algorithms that balance search sensitivity with computational speed. We have developed such an algorithm to detect the periodic Doppler shift the signal frequency experiences with each orbit of the binary system. Since these orbits are extremely stable over the course of the detector observation time ($T_{obs} \sim 1$ year), our search method exploits the periodicity by using two successive Fourier transformations of the detector output. Hence the name *TwoSpect* (from the use of two successive spectral transformations). Using the power and computational efficiency of Fourier techniques,

this search enables an all-sky search for neutron stars in binary systems over a wide region of parameter space.

5.2 Astrophysical parameter space

Observational evidence has shown that neutron stars exist within binary systems with a wide variety of binary orbital parameters [56][1]. As such, any algorithm attempting to probe this region of parameter space should be able to search a wide range of parameter values. In many cases, these systems are nearly circularized (eccentricity $\epsilon \lesssim 10^{-3}$). To get a sense of the largest scale of Doppler shift that occurs due to the binary orbit, we calculate the velocity of the neutron star based on its motion about the binary system's center of mass (using the Newtonian approximation),

$$\frac{GM_{NS}^2 q}{(r_1 + r_2)^2} = M_{NS}\omega^2 r_1 \tag{5.1}$$

where G is the gravitational constant, M_{NS} is the neutron star mass, $q \equiv M_2/M_{NS}$ is the ratio of the companion object to the neutron star mass, and r_1 and r_2 are the distances from the center of the neutron star and companion star to the binary system center-of-mass, respectively. Then, using the period of the binary orbit, $P = 2\pi/\omega$, and the velocity of the neutron star, $v_{NS} = 2\pi r_1/P$, we solve for the neutron star velocity,

$$v_{NS} = \left(\frac{2\pi G M_{NS}}{P}\right)^{1/3} \left[\frac{q}{(1+q)^{2/3}}\right] . \tag{5.2}$$

Therefore, the maximum Doppler shift observable $\Delta f_{max} = f v_{max}/c$ will be

$$\Delta f_{max} \simeq 1.82 \left(\frac{f}{1\,\mathrm{kHz}}\right) \left(\frac{M_{NS}}{1.4\,M_\odot}\right)^{1/3} \left(\frac{P}{2\,\mathrm{hrs}}\right)^{-1/3} \left[\frac{q}{(1+q)^{2/3}}\right] \mathrm{Hz} \tag{5.3}$$

and c is the speed of light.

[1]The Australian National Telescope Facility keeps a database of all known radio pulsars and is reachable on the web via http://www.atnf.csiro.au/research/pulsar/psrcat/.

The maximum Doppler shift can vary by orders of magnitude depending on the intrinsic spin frequency of the neutron star and the mass of the companion star. For $q \ll 1$, the scale of Δf_{max} is $\sim$18 mHz; for $q \simeq 1$, the scale of Δf_{max} is $\sim$1.15 Hz; and for $q \gg 1$, the scale is $\Delta f_{max} \sim 3.7$ Hz. The present TwoSpect analysis is restricted to $\Delta f_{max} \leq 1$ Hz due to decreasing sensitivity to gravitational waves from sources with increasing Δf_{max} (see Chapter VI). Additionally, the observed Doppler shift caused by the orbital motion also depends on the inclination angle i of the orbital system to the line of sight of the detector. From the observer's point of view, the Doppler shift is scaled by, $\Delta f_{obs} = \Delta f_{true} \sin i$, where i is the inclination angle of the binary orbital plane with respect to the vector which points from the detector to the sky position. The observed Doppler shift is coupled to the parameters

$$\Delta f_{obs} \propto M_{NS}^{1/3} \frac{q}{(1+q)^{2/3}} \sin i \,. \tag{5.4}$$

That is, the constituent masses of the binary system and the inclination angle of the system to the observer cannot be separately determined using the observed Doppler shift alone.

The range of binary orbital periods to search depends on the total observation time, T_{obs}. The upper bound on the orbital period is placed by how many orbits take place during the observation time and are still observed cleanly in the second Fourier transformation. Simulations show that a reasonable upper bound on this orbital period is one-fifth of the total observation time. Meanwhile, the lower bound is governed by the shortest coherence time of the initial Fourier transformation used to cover the parameter space. From this limit, the shortest period $P_{min} = 2$ hours (see figure 5.2 in section 5.2).

The frequency band to be searched is determined by the sensitivity of the detectors to gravitational waves. In this case, the LIGO detectors are most sensitive in the range

of $50 \leq f \leq 1000$ Hz with the best strain sensitivity occurring near 150 Hz. Assuming the emission of gravitational waves occurs because the neutron star's crust supports an ellipticity of the moment of inertia, emitting waves at twice the rotational frequency, this corresponds to neutron star spin frequencies of $25 \leq \nu \leq 500$ Hz. There are 182 known pulsars with observed spin frequencies greater than 25 Hz, and, of these pulsars, 111 are located within binary systems [56].

5.3 Overview of the TwoSpect analysis technique

As described in section 5.1, the TwoSpect algorithm exploits the long-term periodicity of signal power within a range of frequency bins of sequential, short coherence length Fourier transforms (so-called *SFTs*). In other all-sky semi-coherent search methods, the typical coherence time for SFTs is $T_{SFT} = 1800$ seconds. TwoSpect uses coherence lengths of 1800 seconds and shorter (see section 5.4). While the all-sky search methods presented previously allow arbitrary gaps between SFTs, the algorithm presented here requires SFTs to start with synchronously aligned start times. Drop-outs in the data stream, either due to loss of detector control or periods of poor data quality, are filled with zeros to maintain synchronization.

The magnitude-squared of the Fourier coefficients (the "power") calculated from the SFTs that are produced from the calibrated detector gravitational wave channel, $h(t)$, are computed in the detector's rest frame and must be corrected to account for the motion of the detector with respect to the Solar System barycenter (see section 5.4 for further description). After this correction is made, a second Fourier transform is computed for each SFT frequency bin power as a function of time. Signals with periodically varying frequency will cause excess power to be found in the second Fourier transforms' frequency bins corresponding to the fundamental frequency, and possibly, the higher harmonic frequencies. Figure 5.1 shows an example of a strong periodically varying signal from a simulated source of continuous gravitational waves

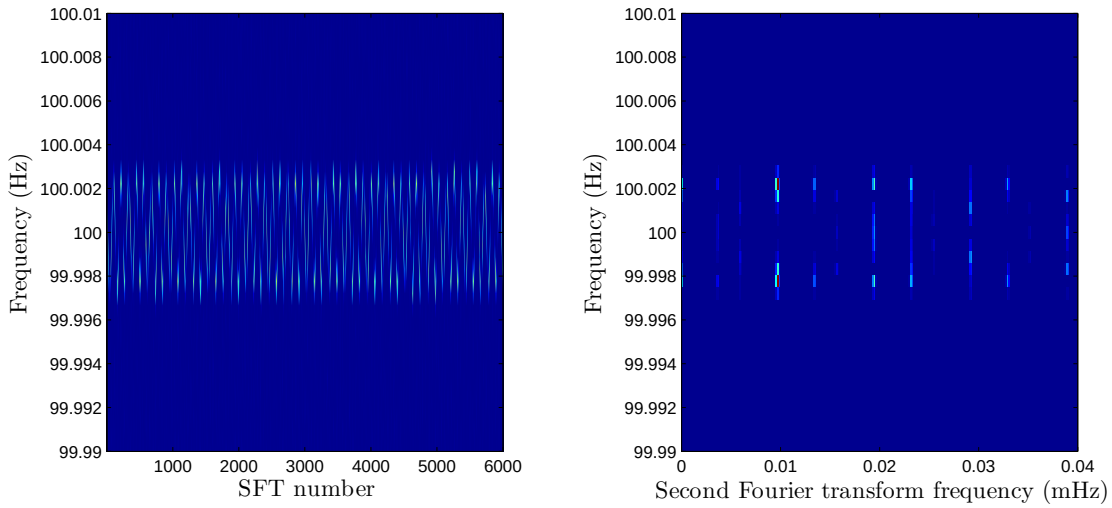

Figure 5.1: Left: Time-frequency plot of a simulated strong continuous wave signal in detector data over nearly 10 weeks of observation. The SFT data has been corrected for the motion of the detector and the antenna pattern weighting. Right: After Fourier transformation of each frequency bin's powers as a function of time, the periodicity of the signal is clearly visible with harmonics of the binary orbital period clearly evident in the second Fourier transform.

located in a binary system.

Once the second Fourier transform powers are computed, the algorithm must locate the pixels with excess power and obtain the most likely set of signal parameters. For TwoSpect, these signal parameters are $(\alpha, \delta, f, P, \Delta f)$ where (α, δ) is the sky location in right ascension and declination, f is the frequency of the gravitational wave signal in the barycentric reference frame, P is the orbital period of the detected signal, and Δf is the observed frequency modulation amplitude. One must also include potential spin-down (or spin-up), $\dot{f}$, of the NS as well, but at this stage of development, we neglect the intrinsic spin-down of the neutron star. The observed spin-down of millisecond pulsars in binary systems is typically much smaller than isolated pulsars ($\dot{f} \lesssim 10^{-16}$ Hz/s) [56]. Implementation of a spindown parameter search will increase the TwoSpect computational cost.

By reducing the binary orbital search parameters from five for the general binary orbit (three for a circularized orbit) to the two parameters used by TwoSpect, computational efficiency is gained at the cost of sensitivity. The computational savings provided permit the search to complete in a reasonable amount of time.

5.4 Details of the TwoSpect algorithm

5.4.1 TwoSpect parameter space

The calibrated time series strain data, $h(t)$, from a detector is divided into short segments of length T_{SFT} that are coherently analyzed using the Fourier transform algorithm. These short stretches of data are windowed using the Hann window function in order to minimize signal leakage into neighboring frequency bins, and each SFT segment overlaps by 50%. This analysis assumes the signal is Doppler modulated by the source motion in such a way in that it periodically is moving between SFT frequency bins. In order to constrain the signal to a single frequency bin for a single SFT, the SFT coherence time is bounded by

$$T_{SFT} \leq \left(\frac{P}{2\Delta f}\right)^{1/2} . \tag{5.5}$$

Using equation (5.5), different regions of parameter space are probed via different coherence times for the SFTs.

The best sensitivity is achieved when using the longest coherence time possible for the SFTs. Therefore, we choose the parameter space to be searched based on the coherence time of the SFTs. This choice is illustrated in figure 5.2 where accessible regions of the space $(P, \Delta f)$ available to searches using SFTs of coherence length T_{SFT} lie below the solid lines. The dashed lines indicate Δf_{max} for several different source signal frequencies.

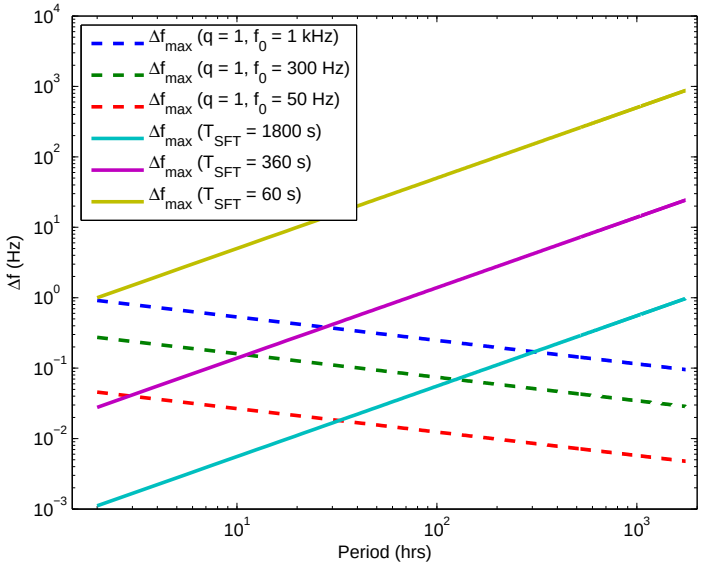

Figure 5.2: The maximum frequency modulation Δf_{max} for three different signal frequencies, 50 Hz, 300 Hz, and 1 kHz, are shown as dashed lines. The maximum frequency modulation for a given period used by the TwoSpect algorithm is shown in solid lines. Successively shorter T_{SFT} values are used in order to illustrate the extent of the parameter space.

5.4.2 Data preparation

The calibrated detector $h(t)$ data is selected by choosing segment lengths in which the detector is operating in its nominal condition, so-called *category 1 flags* are used to select these segments. Then, the segments are divided into lengths of T_{SFT}, synchronously aligned to $T_{SFT}/2$ to be Fourier analyzed. Gaps in the SFTs are filled with zeros. The "power" in each frequency bin is computed by taking the complex conjugate squared of the Fourier coefficients. The instantaneous signal frequency in the Solar System barycenter (SSB) frame, $\hat{f}(t)$, is a frequency modulated signal in the detector reference frame, $f(t)$. The detector signal can be converted to the instantaneous frequency in the SSB frame by [4, 8]

$$f(t) - \hat{f}(t) = \hat{f}(t)\frac{\mathbf{v}(t)\cdot\hat{\mathbf{n}}}{c} \tag{5.6}$$

where $\mathbf{v}(t)$ is the detector velocity with respect to the SSB frame and $\hat{\mathbf{n}}$ is the unit vector in the direction of the sky location to be observed. The detector velocity is computed using Earth-Sun ephemeris files[2].

Thus, the powers in frequency bins can be adjusted for the motion of the detector located on Earth with respect to a given sky location (see figure 5.3). This type of "barycentering" is used in many semi-coherent, all-sky search algorithms [8, 11]. The intrinsic angular resolution between two different sky locations is given by,

$$\varphi_{min} = \frac{c}{(v\sin\theta)_{max}}\frac{1}{2fT_{SFT}} \tag{5.7}$$

where φ_{min} is the smallest difference in angle between any two sky positions, v is the magnitude of the detector velocity, θ is the angle between the detector velocity and the unit vector which points to the sky position of the source in the SSB frame, and

[2]The Jet Propulsion Laboratory maintains the ephemerides for Solar System bodies and can be found at http://ssd.jpl.nasa.gov/.

f is the observation frequency. The number of sky locations is approximately,

$$N_{sky} \approx \frac{4\pi}{\varphi_{min}^2} \tag{5.8}$$

$$\approx 2 \times 10^4 \left(\frac{f}{100\,\mathrm{Hz}} \right)^2 \left(\frac{T_{SFT}}{1800\,\mathrm{s}} \right)^2 . \tag{5.9}$$

Equation (5.8) defines an isotropic sky grid. This grid oversamples regions of the sky where the velocity of the detector with respect to the sky location does not change significantly between nearby locations. One consequence of using shorter coherence length SFTs is a quadratic reduction in the number of sky points searched.

For each sky position, the powers of each frequency bin are adjusted with respect to the detector velocity, the expectation value of the SFT powers in the absence of a signal is subtracted from the SFT power, and the data is weighted for detector antenna pattern variation and the variance of each SFT in the absence of a signal. The expectation value of power is computed from a running median over SFT frequency bins in order to avoid biasing the background estimate due to instrumental lines or gravitational wave signals. The running median is converted to a mean using the correct bias factor for an exponential distribution [8, 59, 60].

The noise-weighted, mean subtracted power in frequency bin k as a function of SFT number n is given by,

$$P_n'^k = \frac{P_n^k - \langle P^k \rangle_n}{\langle P^k \rangle_n^2} \left[\sum_n \frac{1}{\langle P^k \rangle_n^2} \right]^{-1} \tag{5.10}$$

where $\langle P^k \rangle_n$ is the expected power in frequency bin k for SFT n, and the term in square brackets is used to correctly normalize the weighting. The original SFT powers, P_n^k, are normalized such that the expectation value of the noise is equal to 1.

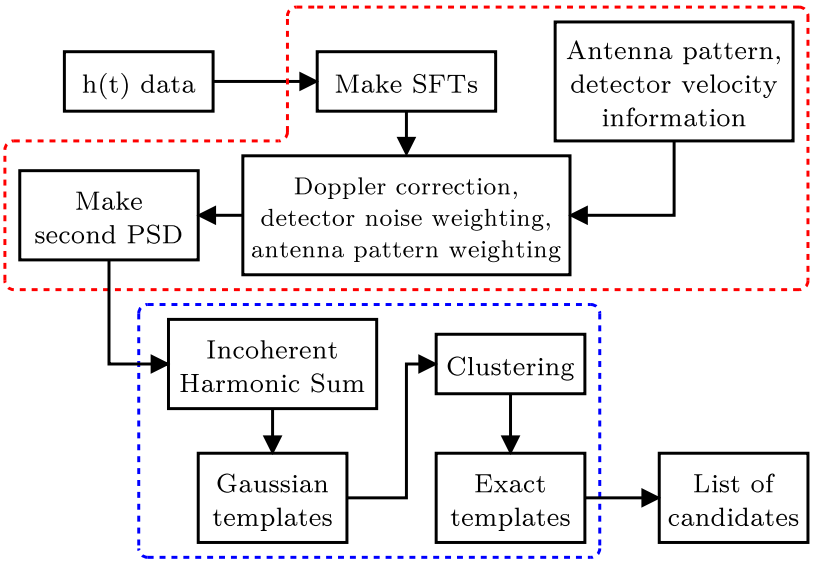

Figure 5.3: Flow chart schematic illustrating the basic hierarchical TwoSpect search pipeline.

Including antenna pattern weighting in equation (5.10) yields

$$\widetilde{P}_n^k = \frac{F_n^2(P_n^k - \langle P^k \rangle_n)}{\langle P^k \rangle_n^2} \left[\sum_n \frac{F_n^4}{\langle P^k \rangle_n^2} \right]^{-1} \tag{5.11}$$

where $\widetilde{P}_n$ are the new values of powers after mean subtraction and noise and antenna pattern weighting, and the antenna pattern is $F_n^2 = F_{n,+}^2 + F_{n,\times}^2$ for a given sky location. This is equivalent to the variable the PowerFlux search calculates for a circularly polarized gravitational wave, except here we subtract the expected noise so that the expectation value of $\widetilde{P}^k$ is equal to zero.

The advantage in using this weighting scheme is that SFTs with high noise levels or low antenna pattern values are suppressed, while SFTs with lower noise levels or higher antenna pattern values are more heavily weighted. The value of $\widetilde{P}_n$ maximizes the signal-to-noise ratio of potential signals [8].

The Fourier transform of $\widetilde{P}_n$ is then computed for each frequency bin k, and normalized such that the expectation value of the noise is equal to 1. The noise-only

distribution of powers from the Fourier transform of $\widetilde{P}_n$ is a χ^2 distribution with 2 degrees of freedom. When there is a persistent Doppler modulated signal, the second Fourier transform has excess power at frequency bins corresponding to harmonics of the binary orbital period. The goal is to then efficiently find the bins with excess power and characterize any signals that may be present, or to set upper limits if no signals are found.

The noise background of the Fourier transformed powers must be characterized in order to determine the false alarm probability of candidate signals. To assess the noise background of the second Fourier transform powers, the mean value of each SFT's powers is computed across the band of interest. Then, drawing from an exponential distribution with each SFT's average as a function of time, a time series of powers is created, the expected background value is subtracted and a Fourier transform is computed. This is repeated many times ($\sim$100) and averaged to find an estimate of the background noise power in each second Fourier transform for each sky location. Then, the background is scaled for different SFT frequencies depending on the mean value of the time series of powers in those SFT frequency bins.

5.4.3 TwoSpect detection statistic

Assume the signal power is distributed among M pixels of the second Fourier transform for a narrow band of SFT frequencies, with the fraction of the signal in pixel m equal to w_m. A useful statistic to sum pixel powers is

$$R = \frac{\sum_{m=0}^{M-1} w_m(x_m - \lambda_m)}{\sum_{m=0}^{M-1} w_m^2} \tag{5.12}$$

where λ_m is the expected noise value of pixel m of the second Fourier transform (see section 5.4.2). For a noise-only signal, the expectation value of R will equal zero by design. If the input time series of data is random, Gaussian white noise, then the

value of R is a weighted χ^2 variable with $2M$ degrees of freedom with zero-mean. The weights, w_m, for each pixel location, m, in the second Fourier transforms for every frequency in the band, are determined by using a set of templates with parameters $(f, P, \Delta f)$ using the same T_{SFT} and T_{obs} as the search.

Since the power spectrum of a time series of Fourier powers is used by the R detection statistic, the value of R is proportional to the amplitude of the strain signal to the fourth power. We expect the value of the reconstructed strain amplitude, h_{rec}, to scale with the value of R, T_{SFT}, and T_{obs} by,

$$h_{rec} \propto \left(\frac{R}{T_{SFT}T_{obs}}\right)^{1/4}. \tag{5.13}$$

Thus, for increasing observation time and given a threshold for which signals are detectable at a particular confidence level, the detectable strain amplitude decreases as the fourth-root of the observation time and the SFT coherence time.

The scale factor to convert equation (5.13) into an equality is determined using a series of simulated signals with random frequencies, periods, and modulation depths. The mean value of these scale factors is used to determine the relationship between R and h_{rec} and is given by,

$$h_{rec} \simeq 3S_h^{1/2}\left(\frac{R}{T_{SFT}T_{obs}}\right)^{1/4}, \tag{5.14}$$

where the scaling $S_h^{1/2}$ is the noise amplitude spectral density is included due to the normalization of the time series of SFT powers.

5.4.4 Computation of templates

Template weights are calculated using two methods. The first type is called "Gaussian" because the second Fourier transforms are analytically calculated from a series of periodic Gaussian functions serving as templates, as described by the following

equation

$$x_k(t) = \sum_{n=1}^{N} \left[e^{-(t-nP)^2/2\sigma^2} + e^{-(t-nP-\Delta_k)^2/2\sigma^2} \right] \tag{5.15}$$

where k signifies the first Fourier transform frequency bin, $N = \text{round}(T_{obs}/P)$, $\Delta_k = T_2 - P$ is the characteristic time between Gaussians in frequency bin k, and σ determines the width of the Gaussian functions. Equation (5.15) mimics the variation of the periodically varying signal in a binary system.

The Fourier transform of $x_k(t)$ yields

$$x_k(\omega) = \sqrt{2\pi\sigma^2} \sum_{n=1}^{N} \left[e^{-\omega(2iP+\omega\sigma^2)/2} + e^{-\omega[2i(P+\Delta_k)+\omega\sigma^2]/2} \right] . \tag{5.16}$$

Taking the magnitude squared, we recover the powers

$$|x_k(\omega)|^2 = 4\pi\sigma^2 e^{-\sigma^2\omega^2} [1 + \cos(\Delta_k\omega)] \frac{\cos(NP\omega) - 1}{\cos(P\omega) - 1} . \tag{5.17}$$

To use equation (5.17) for a signal with expected values of $(f, P, \Delta f)$, Δ_k and σ must be computed. The value of Δ_k is easily determined to be

$$\Delta_k = \frac{P}{2} - \frac{P}{\pi} \sin^{-1} \left[\frac{(f_k - f_0)}{\Delta f} \right] \tag{5.18}$$

where in the case that $|f_k - f_0|/\Delta f > 1$ we set $\Delta_k = 0$. The rate at which the signal moves from one frequency bin to the next in the first Fourier transforms determines the size of σ. This relationship was numerically determined from simulations of various signal velocities.

The second method of template weight calculation is called "exact," because the templates used are closer to the true numerical values of a potential signal in each pixel of the second Fourier transform than the Gaussian templates. Note, however, that these are not the *true* values of the signal power for a given set of signal parameters, merely close approximations. The advantage of the Gaussian templates is

that the weights are analytically determined so the calculation of the weights is computationally efficient. In the case of the exact templates, the power value for each SFT frequency bin are analytically determined assuming a signal with parameters $(f, P, \Delta f)$ (and an arbitrary initial phase), then the Fourier transform of each SFT frequency bin is computed.

The equation for the power of a signal-only, Hann-windowed, normalized Fourier transform is given by

$$|x_m(n)|^2 = \frac{2}{3}\frac{\mathrm{sinc}^2[k + \Delta f T_{SFT}\sin(2\pi n T_{1/2}/P) - m]}{\left[(k + \Delta f T_{SFT}\sin(2\pi n T_{1/2}/P) - m)^2 - 1\right]^2} \tag{5.19}$$

where k is the frequency bin for a non-modulated signal, m is a particular SFT frequency bin for which the power is to be computed, and $T_{1/2}$ is the midpoint of the SFT coherence time. For practical purposes, when $|k+\Delta f T_{SFT}\sin(2\pi n T_{1/2}/P)-m| > 5$ the power is sufficiently small to set $|x_m|^2$ to zero. Once each SFT is analytically computed, the FFT for each frequency bin m is computed to create the template.

For either template calculation method, the largest M weight values are normalized by the sum of all weights computed. The distribution of weights is dependent on the signal parameters. To achieve maximum sensitivity, every weight for a given template should be used, but this is computationally costly. Using a smaller number of weights is more efficient. The number of pixels which sum to 90% of the total template weight is typically of the order of 100 pixels. The largest weights and their pixel locations are identified and sorted using an insertion sorting routine.

A clustering algorithm is employed in the TwoSpect pipeline in order to 1) recombine multiple candidates related to a single source into a single, most significant candidate and 2) reduce computational costs in later pipeline stages. Clustering is accomplished by grouping candidates into sequences of signal frequency and nearby binary orbital periods. Then, the range of frequency modulation amplitude values

are tested and the most significant candidate is selected.

The final results of the TwoSpect pipeline are reconstructions of the source parameters ($h_{rec}, f_{rec}, P_{rec}, \Delta f_{rec}$) for every sky position. However, for a measured signal using only the TwoSpect analysis, we can gain insight into only the amplitude of the gravitational wave signal h, binary orbital parameter P, and gravitational wave frequency f. Since we are measuring Δf and not Δf_{max}, we are unable to separate the mass ratio q from the binary orbital inclination angle i. If we observe a signal with significance beyond our expectation for noise alone, then follow-up studies using other analysis methods may help to determine these other binary orbital parameters.

5.4.5 Placement of templates

Computational limitations restrict the amount of parameter space that can be covered using a lattice of templates placed for a given allowed mismatch μ. The mismatch defines the fraction by which R is reduced when using a template that does not match the true signal parameters. The maximum separation values were determined empirically using simulated data. Figures 5.4 and 5.5 show the results of one set of simulations to compute template spacings.

Placing templates in frequency space would give a mismatch of $\lesssim$0.2 for templates spaced by $1/(2T_{SFT})$ Hz. This indicates that the resolution of the signal frequency using a mismatch value of 0.2 would be no better than $1/(2T_{SFT})$ Hz. Decreasing the mismatch value, i.e. decreasing spacing between templates, would improve the resolution but increase computational costs of the search.

For placement of the templates in binary orbital period we use an iterative routine,

$$\Delta P = P_1 - P_0 \tag{5.20}$$

where P_1 is the new period a distance ΔP away from the previous period P_0. This

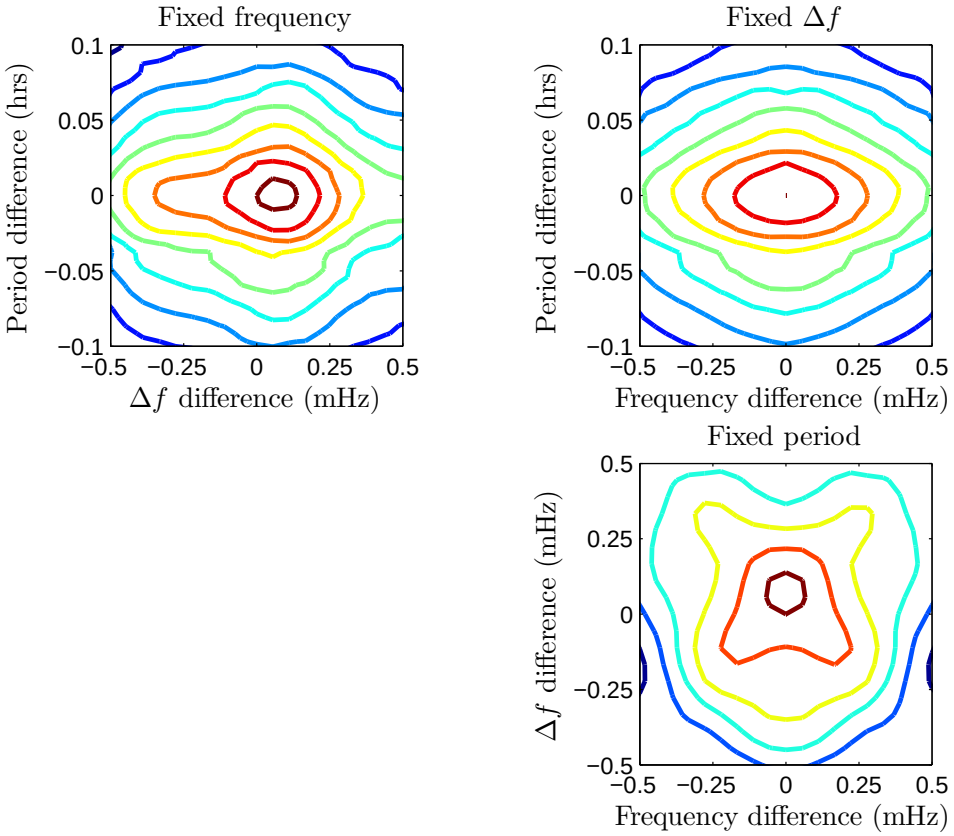

Figure 5.4: Contour curves from different "exact" templates matched against an injected signal with parameters $f = 100$ Hz, $P = 14.274$ hrs, and $\Delta f = 3.67$ mHz. In each plot, one parameter is held fixed while varying the remaining parameters. Darker curves correspond to smaller R values.

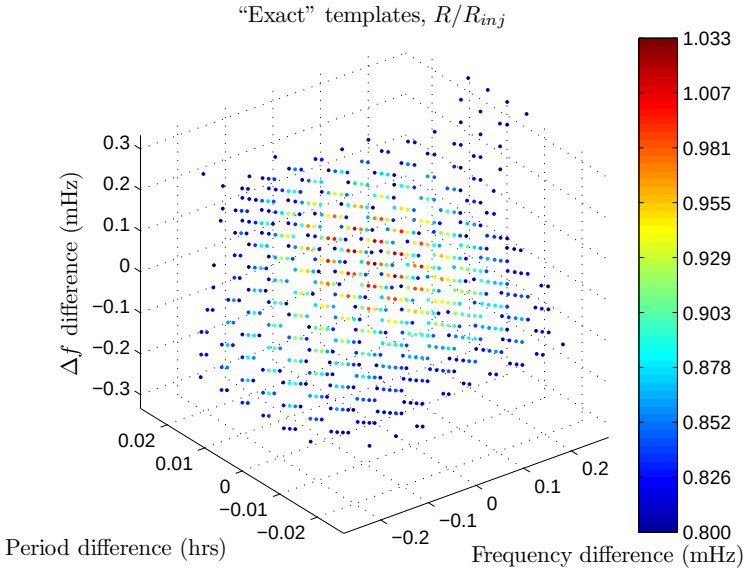

Figure 5.5: Scatter plot from different "exact" templates matched against an injected signal with parameters $f = 100$ Hz, $P = 14.274$ hrs, and $\Delta f = 3.67$ mHz. Here, only templates with a normalized R value greater than or equal to 0.8 were kept. This corresponds to a mismatch 0.2 or less.

can be written assuming that the signal is shifted some fraction of a second Fourier transform frequency bin,

$$\Delta P = \frac{1}{1/P_0 - 1/(xT_{obs})} - P_0\,. \tag{5.21}$$

Here, $1/(xT_{obs})$ is the fractional bin shift for a given mismatch μ, and x is an empirically derived parameter. To first order in $P_0/(xT_{obs})$,

$$\Delta P \simeq \frac{P_0^2}{xT_{obs}}\,. \tag{5.22}$$

The empirically derived value for x is linearly dependent on the coherence time as $x \simeq 2.7(T_{coh}/1800\,\mathrm{s}) + 1.8$. The empirically derived value for ΔP scales inversely with the square root of the modulation depth because the signal at the turning points of the frequency variation in the second Fourier transform scales with the square root

of the modulation depth for a fixed binary orbital period. Therefore, the distance in period spacing between templates must be reduced as the modulation depth increases.

The spacing in modulation depth is similar to the spacing of templates in frequency. For a mismatch of $\mu = 0.2$ the spacing of templates is $1/(2T_{SFT})$.

Using the above expressions, it is possible to determine the expected number of templates needed for a particular set of search parameters. For example, given $\mu = 0.2$, the number of templates for the binary orbital period is

$$N_P(\Delta f) \simeq \left[1.17 \times 10^4 \left(\frac{T_{SFT}}{1800\,\mathrm{s}}\right) + 7.71 \times 10^3\right] \left(\frac{T_{obs}}{1\,\mathrm{yr}}\right) \left(\frac{P_{min}}{2\,\mathrm{hrs}}\right)^{-1} \left(\frac{\Delta f}{3.6\,\mathrm{mHz}}\right)^{-1/2} . \tag{5.23}$$

Here, it was assumed that $P_{min} \ll T_{obs}$ and $P_{min} \ll P_{max}$. Note that the number of templates has a power-law dependence on the modulation depth of the signal where calculated values were determined with $\Delta f = 3.6$ mHz. The number of templates in the 3-dimensional parameter space $(f_0, P, \Delta f)$ is

$$N_{f,P,\Delta f} = \int_{f_{min}}^{f_{max}} \int_{\Delta f_{min}}^{\Delta f_{max}} \frac{N_P(\Delta f)}{d\Delta f df}\, d\Delta f df\,. \tag{5.24}$$

Replacing $d\Delta f = df = 1/2T_{SFT}$, the double integral can be solved. Searching the whole sky in a 1 Hz band at 100 Hz, covering a range of periods down to 2 hours, using 1 year of data broken into 1800 second segments would require N_{tot} templates,

$$N_{tot} = N_{sky} N_{f,P,\Delta f} \tag{5.25}$$

$$\simeq \left[3 \times 10^{14} \left(\frac{T_{SFT}}{1800\,\mathrm{s}}\right) + 2 \times 10^{14}\right] \left(\frac{T_{obs}}{1\,\mathrm{yr}}\right) \left(\frac{T_{SFT}}{1800\,\mathrm{s}}\right)^4 \left(\frac{P_{min}}{2\,\mathrm{hrs}}\right)^{-1} \left(\frac{f_{band}}{1\,\mathrm{Hz}}\right) \left(\frac{f}{100\,\mathrm{Hz}}\right) \left(\Delta f_{max}^{1/2} - \Delta f_{min}^{1/2}\right) . \tag{5.26}$$

This is a vast number of templates to search, but the search is feasible with available computational resources. The trade-off between search sensitivity and computational

cost is assisted by configuring the pipeline in a hierarchical manner. This hierarchy is assisted by utilizing a pre-template stage which reduces the parameter space needing to be searched using templates (see figure 5.3).

5.4.6 Incoherent harmonic sum

The search is initiated with an unbiased, efficient algorithm to extract regions of parameter space to be searched later using templates. An incoherent harmonic summing (IHS) algorithm is employed based upon techniques developed in the radio astronomy community [72]. Using this algorithm, each *second Fourier transform* power spectrum is stretched an integer S times, and each harmonic factor is summed. If a periodic signal is present, then the IHS algorithm will accumulate the signal into the harmonic frequencies of the signal. The signal-to-noise ratio of the signal bins grow $\propto\sqrt{S}$ provided the harmonic powers have similar SNR in the original spectra. In practice, this increase in SNR is limited by the strength of the signal harmonics, giving this search a limit of $S \sim 5$. To accumulate additional signal power, the maximum IHS values across multiple SFT frequency bins are summed. Each series of summed IHS values are subjected to a threshold test on the sum of the maximum IHS values at each SFT frequency (see figure 5.6). Then, a coincidence test must be satisfied where the most significant pair of maximum IHS values in the sequence of SFT frequencies must be symmetric across the summed IHS values.

The coincidence criterion is determined using a χ^2 test for symmetry of a signal in the second Fourier transform domain. Let P be the number of column pairs, m_i^l and m_i^u are the measured lower and upper locations of the IHS for that row in pair i, σ_{l_i} and σ_{u_i} are the uncertainties in measured locations, and T_i^l and T_i^u are the true locations of the IHS values. The statistic $\mathcal{M}$ is a χ^2 test for coincidence

$$\mathcal{M} = \sum_{i=1}^{P} \left[\frac{(m_i^l - T_i^l)^2}{\sigma_{l_i}^2} + \frac{(m_i^u - T_i^u)^2}{\sigma_{u_i}^2} \right] \tag{5.27}$$

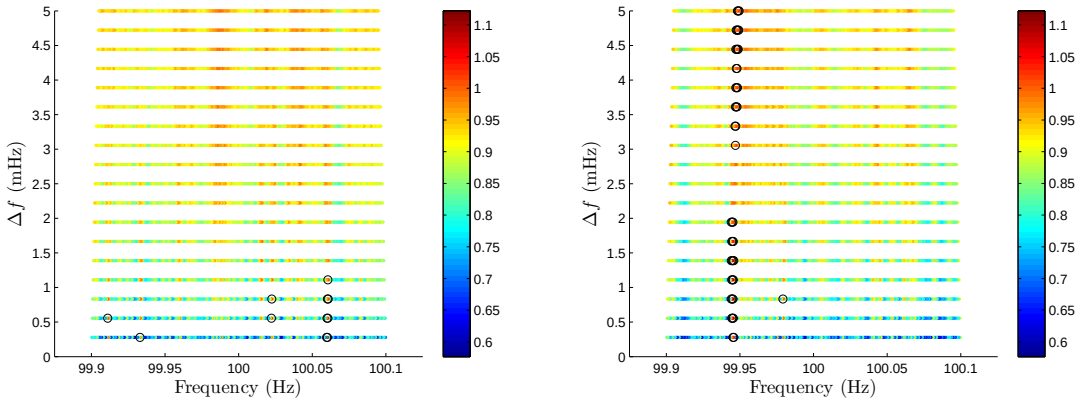

(a) Noise-only. (b) Moderate strength simulated signal injection.

Figure 5.6: The maximum IHS values across sequential SFT frequency bins normalized by the expected false alarm threshold value for frequency modulation amplitudes between 0.5 and 9.5 frequency bins ($0.28 \leq \Delta f \leq 5$ mHz). (a) The noise-only case shows a few candidate events. Note the variance of the maximum IHS values decreases with increasing modulation depth due to the sum across multiple SFT bins. (b) The weak signal case shows a few candidate events (indicated by black empty circles). Note the correlations along the vertical axis.

This function should be minimized subject to the constraint that $T_i^l - T_i^u = 0$. Therefore, a Lagrange multiplier is introduced. The minimum value satisfies,

$$\nabla \mathcal{M} = \sum_{i=1}^{P} \lambda_i \nabla (T_i^l - T_i^u) \tag{5.28}$$

and

$$T_i^l - T_i^u = 0\,. \tag{5.29}$$

The result yields the system of equations,

$$\frac{2(m_i^l - T_i^l)}{\sigma_{l_i}^2} = \lambda_i \tag{5.30}$$

$$\frac{2(m_i^u - T_i^u)}{\sigma_{u_i}^2} = -\lambda_i \tag{5.31}$$

$$T_i^l - T_i^u = 0\,. \tag{5.32}$$

Solving this system of equations for $T_i \equiv T_i^l = T_i^u$ gives the result,

$$T_i = \frac{\sigma_{l_i}^2 \sigma_{u_i}^2}{\sigma_{l_i}^2 + \sigma_{u_i}^2} \left(\frac{m_i^l}{\sigma_{l_i}^2} + \frac{m_i^u}{\sigma_{u_i}^2} \right) . \tag{5.33}$$

This is substituted into the value for $\mathcal{M}$ so that it reduces to

$$\mathcal{M} = \sum_{i=1}^{P} \frac{1}{\sigma_{l_i}^2 + \sigma_{u_i}^2} (m_i^l - m_i^u)^2 . \tag{5.34}$$

Since the IHS location is simply a single bin, the variance in this value is 1/12. The variance is then weighted by the signal-to-noise ratio $\mathcal{S}$ of the IHS value. Substituting $\sigma^2 = 1/12/\mathcal{S}$ we find,

$$\mathcal{M} = \sum_{i=1}^{P} \frac{12\mathcal{S}_l \mathcal{S}_u}{\mathcal{S}_l + \mathcal{S}_u} (m_i^l - m_i^u)^2 . \tag{5.35}$$

In practice, the largest contribution to $\mathcal{M}$ will be dominated by the pair that has the highest combined SNR, we therefore only determine $\mathcal{M}$ for the highest combined SNR pair.

The threshold IHS value is determined by a Monte Carlo simulation of exponentially distributed second Fourier transform noise with expectation values determined by the estimate of the noise-only background, then running the IHS algorithm on the simulated noise, and then computing the necessary sums of multiple noise-only IHS values. The second Fourier transform bin location of the maximum IHS value in an SFT frequency bin is determined and compared across multiple SFT frequencies. This comparison proves useful to eliminate false signals. Once candidate regions of parameter space have passed threshold tests using the IHS routine, the candidate signals are subjected to a threshold test on R using templates based on the values found from the IHS step as described in section 5.4.4.

5.4.7 Significance of candidate events

Candidates are characterized by their false alarm probability, that is, the probability of the candidate's R value arising in a signal-free sample of Gaussian noise. In random noise alone, the TwoSpect search statistic R is the weighted sum of χ^2 random variables, each with 2 degrees of freedom but with differing expectation values for each variable. For equally weighted variables, the distribution of the sum approaches a Gaussian distribution in the limit of a sum of infinite variables. When one variable dominates, the distribution of the weighted sum is approximately exponential.

The problem of calculating the false alarm probability for a sum of weighted χ^2 variables is well-known problem in statistics. The probability that a value of R exceeds a threshold value of R_0 for a single, weighted, χ^2 random variable with two degrees of freedom is given by

$$P(R \geq R_0) = \frac{1}{\lambda_1} \int_{R_0/w_1}^{\infty} e^{\frac{-x_1}{\lambda_1}}\, dx_1 = e^{\frac{-R_0}{w_1\lambda_1}} \tag{5.36}$$

where w_1 is the weight and λ_1 is the expectation value of the χ^2 variable. For a weighted sum of two random variables, $R = w_1x_1 + w_2x_2$, the probability of exceeding a threshold value is

$$\begin{aligned} P(R \geq R_0) &= \frac{1}{\lambda_1} \int_{R_0/w_1}^{\infty} e^{\frac{-x_1}{\lambda_1}}\, dx_1 + \frac{1}{\lambda_1\lambda_2} \int_{0}^{R_0/w_1} \int_{(R_0-w_1x_1)/w_2}^{\infty} e^{\frac{-x_1}{\lambda_1}} e^{\frac{-x_2}{\lambda_2}}\, dx_2 dx_1 \\ &= \frac{e^{\frac{-R_0}{w_1\lambda_1}}\, w_1\lambda_1}{w_1\lambda_1 - w_2\lambda_2} + \frac{e^{\frac{-R_0}{w_2\lambda_2}}\, w_2\lambda_2}{w_2\lambda_2 - w_1\lambda_1} \end{aligned} \tag{5.37}$$

provided that $w_1\lambda_1 > w_2\lambda_2$. In the limit that $w_1\lambda_1 = w_2\lambda_2$, the probability to exceed a threshold is determined using L'hopital's Rule on equation (5.37), where the result is

$$P(R \geq R_0,\, w_1\lambda_1 = w_2\lambda_2) = \frac{e^{\frac{-R_0}{w_1\lambda_1}}(R_0 + w_1\lambda_1)}{w_1\lambda_1}\,. \tag{5.38}$$

These equations can be extended to the sum of N weighted, χ^2 random variables with two degrees of freedom, with each random variable having expectation value λ_i and an associated weight, w_i. The number of integrals in each value to be summed is represented by k, so the total probability is then given by,

$$P(R \geq R_0) = \sum_{k=1}^{N} \left[\sum_{i=1}^{k} \frac{e^{\frac{-R_0}{w_i \lambda_i}} (w_i \lambda_i)^{k-2} w_k \lambda_k}{\prod_{j \neq i} (w_i \lambda_i - w_j \lambda_j)} \right] \tag{5.39}$$

where j runs from $i = 1 \ldots k$ except $j \neq i$. This can be further reduced by combining the $k = 1 \ldots N$ terms to

$$P(R \geq R_0) = \sum_{i=1}^{N} \frac{e^{\frac{-R_0}{w_i \lambda_i}}}{\prod_{j \neq i} \left(1 - \frac{w_j \lambda_j}{w_i \lambda_i}\right)} . \tag{5.40}$$

Unfortunately, equations (5.39) and (5.40) diverge as any number of weights times expectation values approach similar values.

It proves useful to use a *characteristic function* determine the probability of exceeding a threshold in a different way. This technique converts the probability distribution function of random variables to the Fourier domain. Characteristic functions can be used to find the probability distribution for a weighted sum of random χ^2 variables which is discussed in detail in [28, 44]. A summary of the solution using characteristic functions is given below.

A characteristic function, ϕ, describes a random variable, X, by

$$\phi_X(u) = E\left[e^{iuX}\right] = \int_{-\infty}^{\infty} e^{iux} f_X(x)\, dx \tag{5.41}$$

where E represents the expectation value, i is the imaginary unit, and $f_X(x)$ is the probability distribution function of X. A single value which enters the sum in R will

have a characteristic function

$$\phi(u) = \frac{1}{1 - iuw'_j\lambda_j} \tag{5.42}$$

where $w'_j = w_j / \sum_j w_j^2$ and λ_j is the expected noise value in second Fourier transform pixel j.

Since each of these random variables in the sum is independent, the characteristic function of R (neglecting mean subtraction, which is simply a rescaling factor) will take the form

$$\phi_R(u) = \prod_{j=1}^{N} \frac{1}{1 - iuw'_j\lambda_j} \,. \tag{5.43}$$

This is related to formulas previously derived in [28, 44]. However, in the case of TwoSpect, the weights and expectation values are independent for each random variable. Determining the probability that R lies *below* a value R_0 is then given by the Gil-Pelaez formula [33]

$$P(R < R_0) = \frac{1}{2} - \int_{-\infty}^{\infty} \Im\left(\frac{\phi_R(u)e^{-iux}}{2\pi u}\right) du \tag{5.44}$$

and is related to the probability of exceeding the threshold by, $P(R \geq R_0) = 1 - P(R < R_0)$. Solving equation (5.44) requires numerical integration. The details of the integration method can be found in [29]. Though this integral is not solved analytically, the performance of this numeric calculation is significantly faster than estimating the probability function using Monte-Carlo simulations.

The solution to this integral can be used in two ways. First, it can be used when a candidate signal has been detected for a given set of weights, expected noise values for given pixels, and a value of R_0 to determine the probability that purely random noise values would have produced a value of R that is as large as the found R_0. Secondly, this equation can be solved for R_0 using iterative numerical solving techniques when

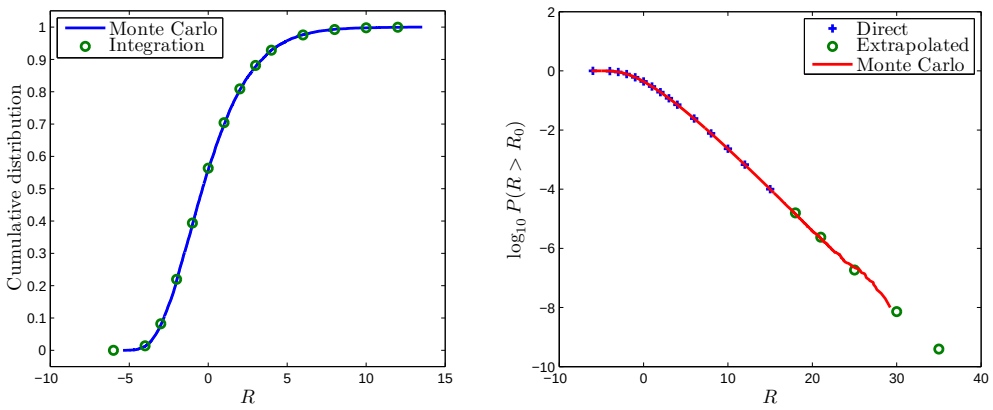

(a) (b)

Figure 5.7: (a) The cumulative distribution function of R for a particular template of w_i values determined using Monte Carlo simulations over Gaussian noise and by numerical integration of the Gil-Pelaez formula. (b) Extrapolation of rare events (gree circles) by exploiting the linear logarithmic probability function in the regime of rare events (tail of blue crosses). A Monte Carlo simulation using exponentially distributed random variables (red line) confirms the validity of the extrapolation.

we wish to set a false alarm probability threshold value of R_0.

5.4.8 Running the TwoSpect analysis code

The TwoSpect program is written in C and stored in the LSC Algorithms Library (LALapps) repository [26]. TwoSpect reads in previously stored SFTs calculated from the calibrated detector $h(t)$ channel for sliding, weighting, and computation of the second Fourier transform (see figure 5.3). The code performs all necessary calculations and outputs a list of candidates which have exceeded threshold values.

The parameter space defined in section 5.4.1 is divided into narrow spans of frequency, binary orbital period, and signal modulation depth and submitted as separate, parallel jobs which are run on LIGO Scientific Collaboration (LSC) computer clusters under the Condor environment. Each job searches over the the entire sky for its range of frequency, binary orbital period and signal modulation depth parameters.

The outer loop of the code searches over sky position. Then the inner loop of

the incoherent harmonic sum step searches over signal frequency and modulation depth, identifying possible binary orbital periods associated with candidates found from this step. Next, each candidate identified in the incoherent harmonic sum step is passed to the template-based approach. Each candidate is compared with possible templates. Those that pass threshold tests are considered to be outliers that need follow-up studies (see chapter VI).

5.5 Summary

We have described a new, computationally efficient method to search for unknown spinning neutron stars emitting gravitational waves that are located in binary systems using two successive Fourier transformations. The detector time series is divided into short segments with length $\leq$1800 seconds. Once the total observation time is divided and Fourier transforms computed for each segment, the effect of the changing detector velocity is compensated for and each segment is weighted according to the antenna pattern and noise within the segment. Then a second Fourier transform is computed for each first Fourier frequency as a function of time.

Sensitivity trade-offs were made by using the computationally more efficient incoherent harmonic summing algorithm in order to limit the number of templates which would otherwise be searched over. While these imposed constraints limit the sensitivity of the search pipeline, they allow coverage of the entire parameter space. An efficient template creation method by analytically solving the Fourier transformation of a series of Gaussian functions is also able to reduce computational costs in the template stage. In chapter VI, the results of tests using simulated data and the first look at LIGO detector data is addressed.

CHAPTER VI

Validation of the TwoSpect pipeline

In addition to testing the various functions of the TwoSpect program to verify algorithm correctness, an end-to-end validation of the complete TwoSpect pipeline is assessed by several methods. First, simulated detector data consisting of *pure noise* has been used to determine threshold levels to limit the number of outliers and assess the typical noise background (see section 6.1). Second, as described in section 6.2, the pipeline has been subjected to different software injections using simulated data with various signal parameters and strain amplitudes in order to determine the sensitivity of the pipeline. Finally, we describe in section 6.3 the analysis of a subset of real detector data from the sixth LIGO Science Run (S6) by TwoSpect to understand potential detector artifacts the pipeline encounters. These validations have confirmed the promising potential and robustness of the pipeline, but have also shown that the estimation of outlier statistical significance needs refinement before we carry out a full search of the S6 data.

6.1 Pure noise tests

A ten-week sample of simulated detector data has been generated using the Makefakedata program. This LALApps repository [26] program was run with options set to create Hann-windowed, noise-only 1800-second SFTs with 50% overlap between

each SFT. The SFT data was centered at 100 Hz, with a bandwidth of 0.2 Hz, and had frequency bin spacing $\delta f = T_{SFT}^{-1} \simeq 5.556 \times 10^{-4}$ Hz. The noise is random, Gaussian, white, and stationary with an expectation value of the amplitude spectral density equal to 0.02357 $\mathrm{Hz}^{-1/2}$ (for testing purposes only)[1]. The parameter space of period and frequency modulation depth searched was divided into subspaces, with each running instance of TwoSpect covering a subspace in a search over the entire sky for the entire bandwidth. The range of parameter values for this search was $f_0 = (99.9, 100.1)$ Hz, $P = [2, 336]$ hrs, and $\Delta f = [0.27, 55.8]$ mHz. The false alarm rate for the IHS step in this run was set at 0.1% while the threshold rate for the template steps was set at 10^{-2}% in order to further reject false signals. In the pipeline, the templates were placed with a mismatch of $\mu = 0.2$. A template-based search only (e.g. a search not using the IHS algorithm) would require of order 10^{13} independent templates to cover this parameter space.

The search described above took about 24 hours to run on 500 computing nodes of LSC computer clusters. Figures 6.1 and 6.2 shows sky maps of the candidates surviving the threshold cuts used. Figure 6.1 shows the resulting logarithmic false alarm probabilities for each candidate's R value, and Figure 6.2 shows each candidate's reconstructed strain amplitude using equation (5.14). The candidates are expected to be randomly scattered over the sky with sporadic arcs around regions where the noise, by random chance, has higher values and the Doppler shift between grid points is not large. The number of IHS "templates" searched is of the order of 10^9. The IHS templates are not strictly independent since there exist correlations between neighboring SFT frequency bins when the IHS values from the different bins are summed (see figure 5.6). The false alarm threshold calculations take these correlations into account when setting the threshold limits.

Histograms of the noise-only candidates' parameters are shown in figures 6.3(a)–

[1]The typical noise amplitude spectral density of a LIGO detector near 100 Hz is of the order of $10^{-22}\,\mathrm{Hz}^{-1/2}$.

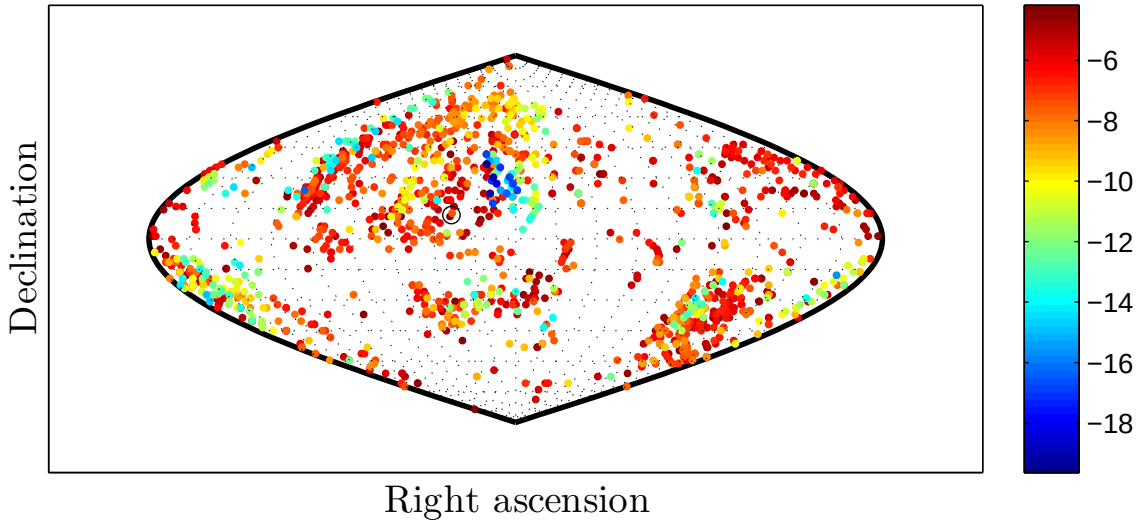

Figure 6.1: Sky map of the candidates' logarithmic likelihood found in noise-only data. The color indicates the probability that noise alone could produce a candidate with certain amplitude. Red colors indicate a higher probability of noise alone is producing a candidate while blue colors indicate a smaller probability. The black circle indicates the average position of the Sun during the observation time. Zero hours right ascension is located at the left of the plot, with increasing right ascension as one moves to the right.

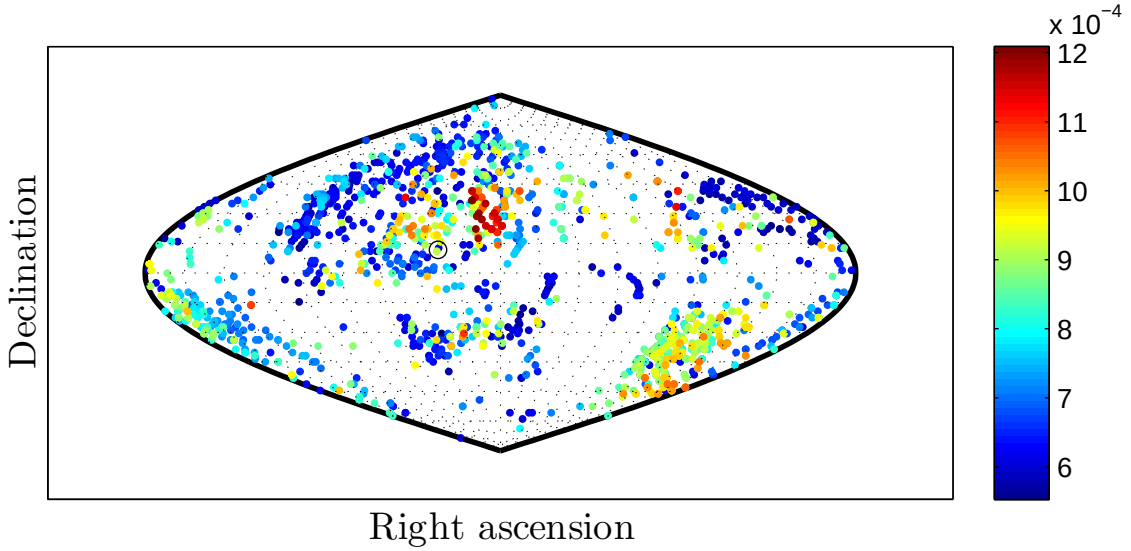

Figure 6.2: Sky map of the candidates' reconstructed strain amplitude found in noise-only data. Red colors indicate a higher amplitude of strain signal while blue colors indicate a lower strain amplitude. The black circle indicates the average position of the Sun during the observation time. Zero hours right ascension is located at the left of the plot, with increasing right ascension as one moves to the right.

(d). The candidates are distributed non-uniformly in frequency (see figure 6.3(b)), with clusters near SFT frequency bins that have noise higher than the typical values in the second Fourier transform. The significant peaks in the distribution of signals in binary orbital period parameter (see figure 6.3(c)) are associated with harmonics of the 12 hour periodic antenna pattern variation, as the detector moves with respect to a particular sky location. A future refinement to the pipeline may include rejection of orbital period harmonics associated with the antenna pattern modulation. Figure 6.3(d) shows a peak at low modulation depths which correspond to modulations of only a few SFT frequency bins. Excess noise in a few SFT frequency bins is more likely to cause such spurious candidates. The remainder of the candidates are randomly distributed in modulation depth.

It is observed that some of the outliers seen in the noise-only data have extremely small false alarm probabilities (see figure 6.3(a)). An uncertainty in the background estimate can have an effect on the calculated false alarm probability that is reported for each candidate if the background is systematically underestimated for the powers in the template. Variations in the logarithmic probability values for the largest outliers have been observed at the level of ± 2 for variations in the parameters used in background estimation. These variations do not, however, fully explain the largest outlier values seen in the simulated noise-only data.

Correlations in the simulated data that are not accounted for in the expected background estimates have not been ruled out as a cause for the extended distribution of outlier values. The noise-only generated data using the Makefakedata program may have residual correlations from SFT overlap, from modulation of the underlying noise envelope by antenna pattern corrections, or from the windowing functions used in the two spectral transformations. These apparent large outliers in random noise are under current investigation.

A future improved version of the TwoSpect pipeline will likely implement a coin-

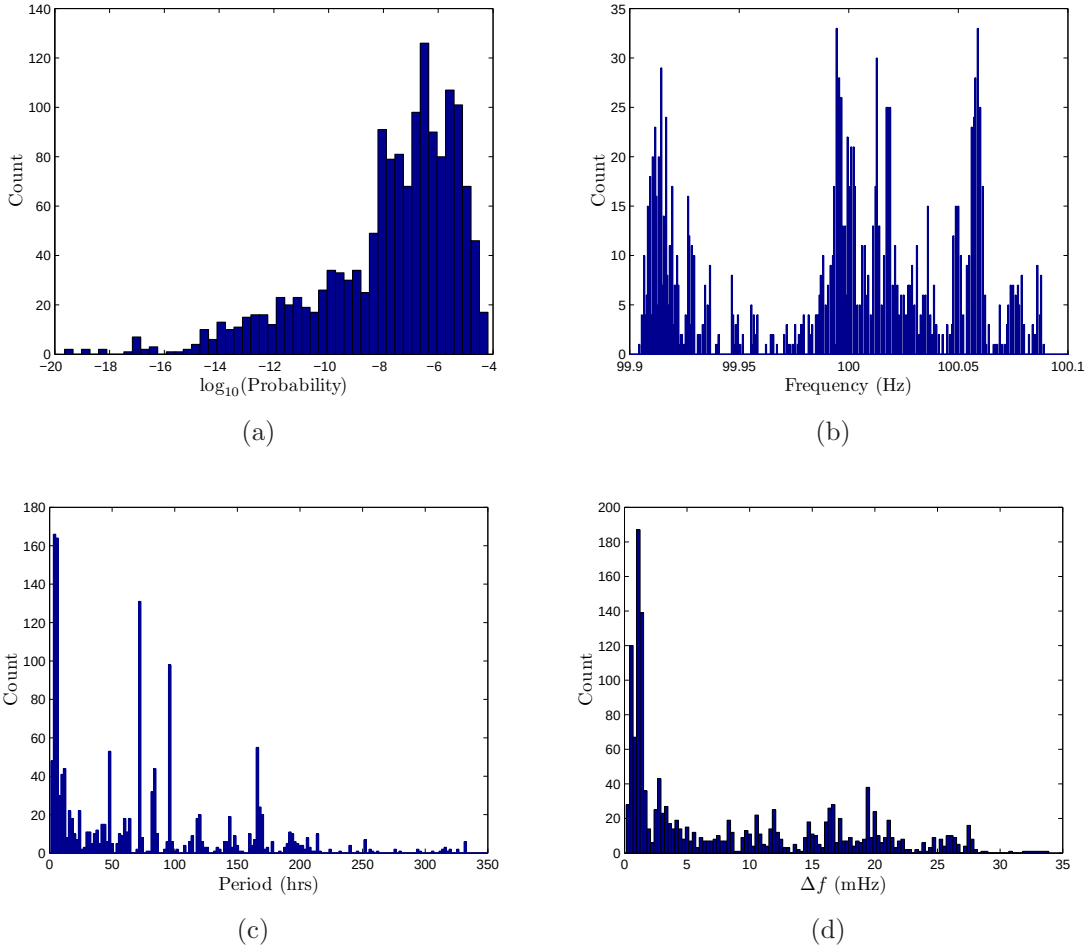

Figure 6.3: Histograms of the candidates found using noise-only data with the IHS false alarm rate set at 0.1% and the template false alarm rate set at 10^{-2}%.

cidence test between the different interferometers in order to remove spurious outliers and keep threshold levels for the pipeline stages low. The criteria for coincidence would be over the signal parameters of each candidate, $(\alpha, \delta, f, P, \Delta f)$, such that to pass the coincidence test, candidates must be found in each detector with parameter values that are nearly the same in each detector. Imposing these constraints should help to eliminate a significant number of outliers in a single detector and allow for a reduction of the threshold levels.

6.2 Simulated signal tests

The TwoSpect analysis program is subjected to various fake signals with random signal parameters and different strain amplitudes, created using the Makefakedata program. Table 6.1 shows the first set of simulated signals and their injection parameters. Test data for pulsar numbers 1 through 10 was generated for the Hanford 4-km interferometer (H1) starting at GPS time 900000000, lasting for 10 weeks of total observation time, with spindown of 0 Hz/s, and cosine of the star's inclination angle $\cos\iota = 1.0$ (yielding circularly polarized waves). The projected semi-major axis was set in each case to provide the Doppler shift indicated, and the orbital eccentricity was set to 0.0. The noise amplitude spectral density, $\sqrt{S_h}$, was set equal to 1.0 $\mathrm{Hz}^{-1/2}$ in every case, with the same noise used in every test by using the same random noise seed value for every simulation.

Table 6.2 shows the corresponding recovered pulsar signal parameters for injections 1 through 10. The TwoSpect algorithm is given the correct sky location of the injection, but no other parameters are given. The search is performed over the entire band with the only restriction on Δf_{rec} given by equation (5.5). Injections 1 through 5 are loud enough that the pipeline correctly identifies them. Injections 6 through 10 are detected with reduced significance ($\log_{10}$(Prob.) nearer to zero) and the parameter estimation is less accurate than the strong signals, and are discussed below. Only the

#	$\sqrt{S_h}$	h_0	f (Hz)	P (hrs)	Δf (mHz)	α (hrs)	δ (deg.)
1	1.0	0.06	100.0000	14.274	3.668	0.0	0.0
2	1.0	0.05	100.0091	5.013	0.808	3.050	-15.59
3	1.0	0.07	100.0815	152.173	10.736	21.921	23.83
4	1.0	0.08	100.0028	91.876	24.775	19.207	-64.46
5	1.0	0.08	99.9504	54.400	6.284	15.121	43.30
6	1.0	0.07	100.0330	312.317	77.020	11.691	-9.29
7	1.0	0.05	99.9670	261.442	27.597	8.750	78.88
8	1.0	0.04	99.9146	10.950	2.435	22.556	18.718
9	1.0	0.06	100.0426	33.509	12.930	21.962	-22.412
10	1.0	0.05	100.0150	117.309	40.961	2.046	-50.373

Table 6.1: Summary of simulated data signals used to test the TwoSpect pipeline.

#	h_{rec}	f_{rec} (Hz)	P_{rec} (hrs)	Δf_{rec} (mHz)	$\log_{10}$(Prob.)
1	0.0622	100.00133	14.270	3.611	-127.6
2	0.0499	100.00917	5.008	0.833	-84.8
3	0.0773	100.08158	151.805	10.556	-146.3
4	0.1036	100.00287	91.974	24.722	-274.0
5	0.1024	99.95035	54.501	6.389	-627.0
6	0.0502	99.94000	311.554	16.667	-20.2
7	0.0594	99.96111	262.315	33.333	-22.4
8	0.0370	99.91556	10.935	3.611	-16.3
9	0.0530	100.04778	33.555	7.222	-41.0
10	0.0571	100.00278	117.887	28.333	-22.9

Table 6.2: Summary of the recovered data signals for pulsars 1 through 10.

most significant candidate for each sky location is listed in table 6.2.

The low-amplitude recovered signals, specifically injection numbers 6 through 10, have inaccurate reconstructions of the true signal. The typical identified parameters that are incorrect are the signal frequency and the frequency modulation depth especially as the signal is spread over more SFT frequency bins with increasing modulation depth. Since the signal is weak, the pipeline has difficulty determining correct values to use for parameter estimation. Injections 6 and 10 have the largest Δf values of the injected signals, and they have the poorest matching reconstructed signal parameters. If only a portion of the Doppler shifted signal is found by TwoSpect, then the frequency and modulation depth are likely to be incorrect while the orbital period is

#	$\sqrt{S_h}$	h_0	f (Hz)	P (hrs)	$a \sin i$ (s)	α (hrs)	δ (deg.)	e
11	1.0	0.07	100.0815	152.173	9.353	21.921	23.83	10^{-4}
12	1.0	0.07	100.0815	152.173	9.353	21.921	23.83	10^{-3}
13	1.0	0.07	100.0815	152.173	9.353	21.921	23.83	10^{-2}
14	1.0	0.07	100.0815	152.173	9.353	21.921	23.83	10^{-1}

Table 6.3: Summary of the low eccentricity orbits simulated data signals used to test the TwoSpect pipeline.

more likely to be accurately identified, at least up to a harmonic factor of the binary orbital period. Also, if a pulsar is at a location in the sky with low antenna pattern values, the value of h_0 must be larger for a confident detection of the signal.

Next, four simulated signals from spinning neutron stars in elliptical orbits were generated. Test data for pulsar numbers 11 through 14 was again created for the H1 detector starting at GPS time 900000000, lasting for 10 weeks of total observation time, with spindown of 0 Hz/s, cosine of the inclination angle $\cos \iota = 1.0$, time of periapsis passage at 900000000.0 (the time of closest approach between the two stars in the Solar System Barycenter frame), argument of periapsis equal to 0.0 radians (this parameter defines the rotation of the elliptical orbit on the sky), and the orbital eccentricity parameter ranging from 10^{-4} to 10^{-1}.

Table 6.4 shows the corresponding recovered pulsar signal parameters from neutron stars 11 through 14 in elliptical orbits. The TwoSpect algorithm is given the correct sky location of the injection, but no other parameters are given. The search is again performed over the entire 0.2 Hz band, with the only restriction on Δf_{rec} given by equation (5.5). Only the most significant candidate for the sky location is listed in table 6.4. Currently, the pipeline does not search over orbital eccentricity of the binary system, so no value of orbital eccentricity is reconstructed. Future versions of the TwoSpect program may be able to search over this parameter.

As shown in table 6.4, the eccentric orbit signals are recovered by the TwoSpect algorithm with nearly the correct frequency, binary orbital period, and reconstructed

#	h_{rec}	f_{rec} (Hz)	P_{rec} (hrs)	Δf_{rec} (mHz)	$\log_{10}$(Prob.)
11	0.0788	100.08152	151.773	10.833	-148.3
12	0.0784	100.08150	150.880	10.833	-160.0
13	0.0788	100.08145	151.800	10.833	-132.7
14	0.0777	100.08045	153.612	10.833	-145.7

Table 6.4: Summary of the recovered data signals for low eccentricity orbits.

strain values. The reconstructed modulation depth is approximately correct for small eccentricity, but for larger eccentricity values, the modulation depth measures only the amplitude of the Doppler shifted frequency. Thus, for modest orbital eccentricity, the TwoSpect algorithm is still able to produce useful results.

6.3 First look at detector data

Disclaimer: the results presented in this section have not been reviewed by the LIGO Scientific Collaboration and do not reflect the scientific opinion of the Collaboration.

The TwoSpect algorithm is applied to a subset of real detector data in order to assess the performance of the pipeline on data which does not necessarily have random, stationary, Gaussian, white noise characteristics. Real detector data often has color to the noise over frequency bands of $\sim$1 Hz and occasional stationary or "wandering" spectral features. Also, the detector is not running the entire time, which creates gaps in the data. These complications must be taken into account for the analysis of detector data. The data analyzed here was taken from the first 20 weeks of the S6 science run from the H1 LIGO interferometer. During times when the detector was offline, or the detector data was corrupted, the SFT powers for that time were set to zero.

The chosen data was the frequency band between 101.1 Hz and 101.3 Hz. Figure 6.4 shows the noise-weighted average of the amplitude spectral density of the H1

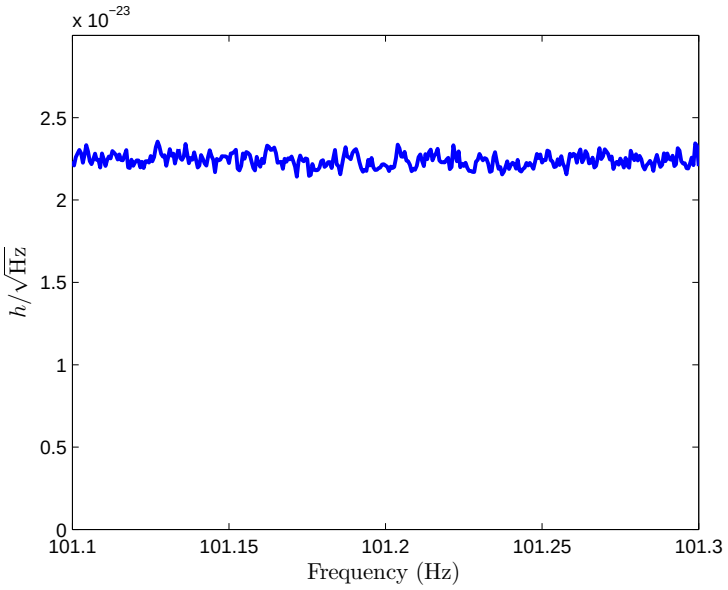

Figure 6.4: The weighted average SFT amplitude spectral density for the first 20 weeks of the S6 science run in the band from 101.1 Hz to 101.3 Hz.

detector in this band using 4109 1800-second Hann-windowed SFTs from the first 20 weeks of S6. Sequential SFTs overlap by 50%. If the detector had been operational during the entire 20-week sample of data, then 13,439 SFTs could have been created. The duty factor of roughly 31% is less than the actual science-mode duty factor, ≈40%, because of the restriction that SFTs must be synchronously started at factors of one-half the coherence time and require continuous stretches of science data longer than 1800 seconds.

Figure 6.5 shows the $\log_{10}$ amplitude spectral density of the first 20 weeks of the S6 SFTs as a function of time (left). The right hand plot shows the $\log_{10}$ normalized power after the second Fourier transform at a particular sky location, following the data weighting and mean-subtraction procedure outlined in section 5.4.2. The normalization of the second Fourier transforms is set such that the mean power is equal to 1.0.

The parameter space of period and frequency modulation depth searched was divided in the same manner as described in section 6.1. The range of parameter values

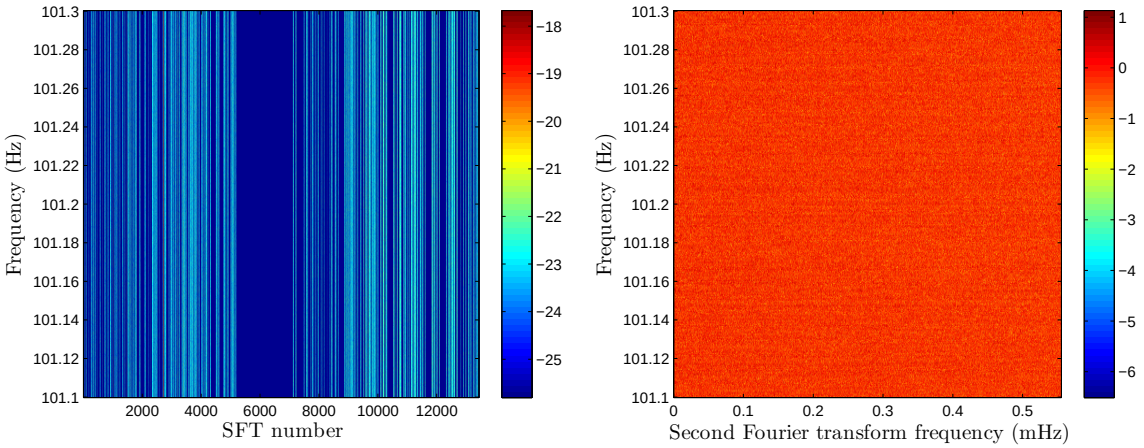

Figure 6.5: Left: The $\log_{10}$ amplitude spectral densities of the S6 SFTs as a function of time. Dark blue colors indicate gaps in the data which are filled with zeros. Right: the second Fourier transform $\log_{10}$ normalized powers for a particular sky location.

of this search was $f_0 = (101.1, 101.3)$ Hz, $P = [2, 672]$ hrs, and $\Delta f = [0.27, 200)$ mHz. The false alarm rate for the IHS step in this run was set at 0.1% while the threshold rate for the template steps was set at 10^{-2}% in order to further reject false signals. In the pipeline, the templates were placed with a mismatch of $\mu = 0.2$.

Figures 6.6 and 6.7 show sky maps of the candidates surviving the threshold cuts used. Figure 6.6 shows the resulting logarithmic false alarm probabilities for each candidate's R value, and figure 6.7 shows each candidates' reconstructed strain amplitude using equation (5.14). Out of roughly 10,000 sky locations, 37 locations had to be rejected due to miscalculation of the background noise estimate. The miscalculation is well understood and will be corrected in future versions of TwoSpect. As one can see from figure 6.7, the amplitude of the strongest candidate observed is $\approx 8 \times 10^{-24}$, indicative of the potential sensitivity of the TwoSpect method.

As shown in figure 6.8(a), the distribution of the candidates' false alarm probabilities passing threshold tests is similar to that expected from tests on noise-only data shown in figure 6.3(a). Since the parameter space is larger, the number of templates

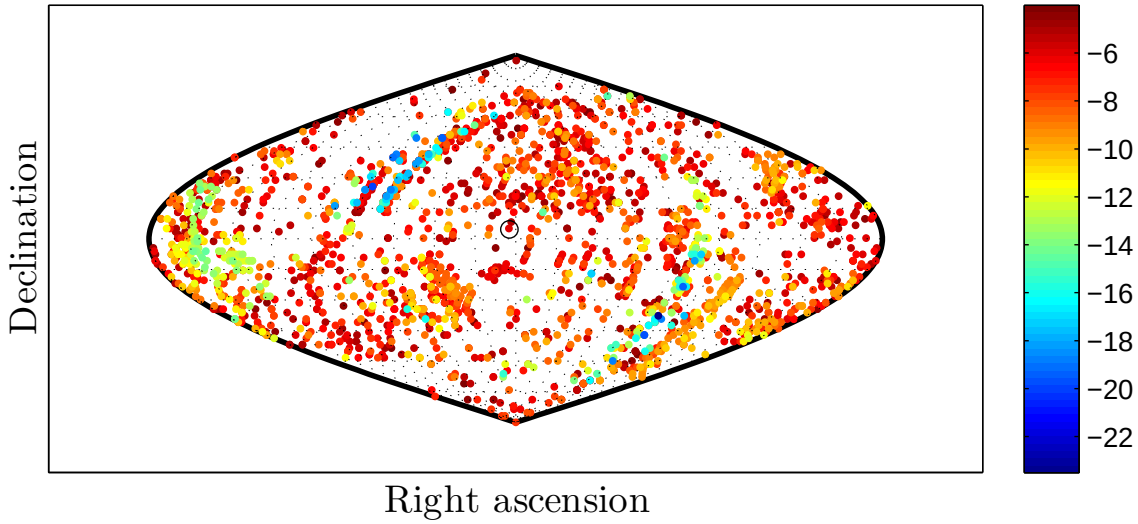

Figure 6.6: Sky map of the candidates' logarithmic likelihood found in S6 data. The color indicates the probability that noise alone could produce a candidate with certain amplitude. Red colors indicate a higher probability of noise alone is producing a candidate while blue colors indicate a smaller probability. The black circle indicates the average position of the Sun during the observation time. Zero hours right ascension is located at the left of the plot, with increasing right ascension as one moves to the right.

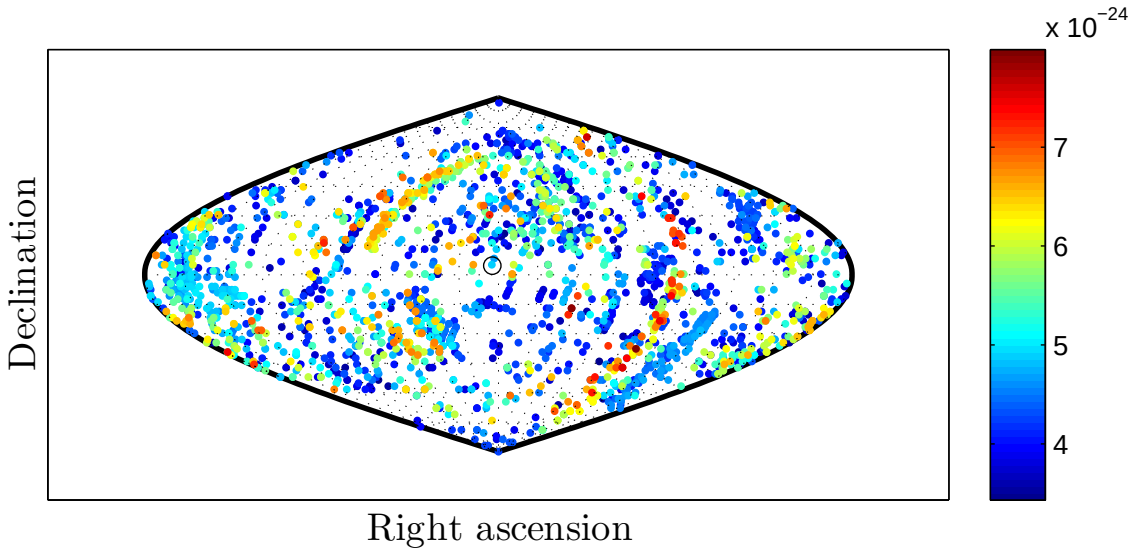

Figure 6.7: Sky map of the candidates' reconstructed strain amplitude found in S6 data. Red colors indicate a higher amplitude of strain signal while blue colors indicate a lower strain amplitude. The black circle indicates the average position of the Sun during the observation time. Zero hours right ascension is located at the left of the plot, with increasing right ascension as one moves to the right.

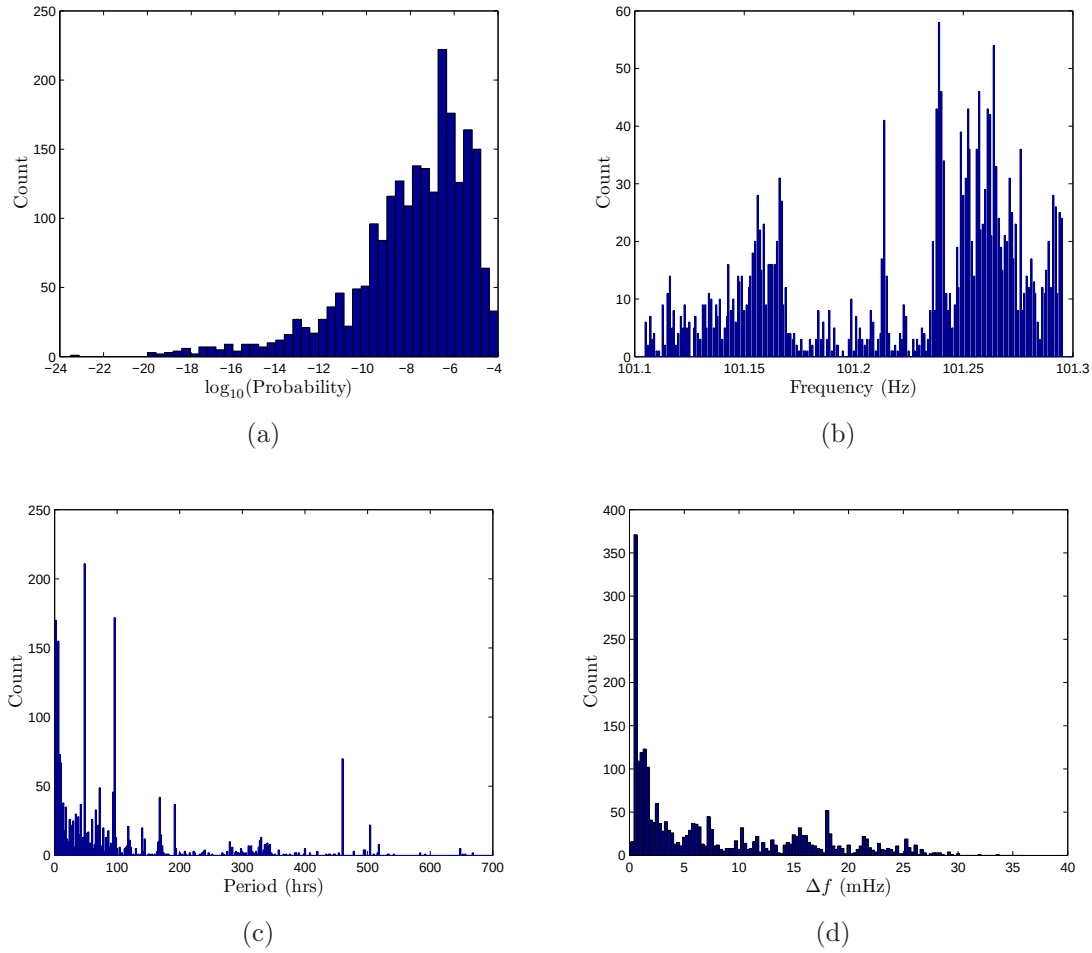

Figure 6.8: Histograms of the candidates found in the first 20 weeks of S6 H1 interferometer data.

would have also increased accordingly, thus causing the false alarm probability of the most significant candidate to decrease, but does not explain the extent of the distribution. Real detector data has spectral artifacts, is not perfectly random, and is non-stationary, all of which could lead to excess outliers. Large excesses of candidates are found with periods corresponding to the antenna pattern variation (see figure 6.8(c)) as is the case in the noise-only simulations. The large peak of candidates with small modulation depths is also expected from the noise-only tests (see figure 6.8(d)).

6.4 Conclusions and outlook

The essential methods used in the TwoSpect algorithm have been validated, and the initial version of the pipeline has been implemented in C code which is now running on LSC computer clusters. End-to-end tests have been conducted using simulated noise-only data, using individual simulated signals from neutron stars in binary systems in noisy data, and with a subset of real detector data from the S6 science run. These tests show that the pipeline is nearly ready to initiate a full search in S6 data. We anticipate that this search will be launched by the end of 2010.

Refinements will be completed on the background estimation method, and further injections will be performed to establish the final sensitivity of the TwoSpect pipeline. Other refinements to the algorithm to reduce memory usage and increase the computational speed may be implemented as well. This work will be undertaken in the coming year, and an internal review of the TwoSpect code will begin.

The TwoSpect algorithm will enable searches for unknown neutron stars in binary systems in gravitational wave detector data. The results of the all-sky analysis may be sensitive enough to begin constraining certain population models of neutron stars. Since more than half of the known pulsars in the LIGO frequency band (assuming gravitational wave emission occurs at twice the rotational frequency of the neutron star) are in binary systems, this method is very useful. A detection of a continuous wave signal would be groundbreaking in the field of gravitational wave physics. Although the search is not as sensitive as other all-sky search methods for isolated neutron stars (e.g. PowerFlux, Einstein@Home), it is the first all-sky algorithm that will search the region of parameter space for quasi-monochromatic gravitational waves emanating from previously unknown neutron stars in binary systems.

CHAPTER VII

Summary

Construction of the Laser Interferometer Gravitational wave Observatory (LIGO) kilometer-scale interferometers in the United States and other gravitational wave detectors around the world, has provided physicists the means to directly detect and measure gravitational waves emitted by astrophysical sources. While no direct observation of these waves has yet been made, upgrades to the existing detectors in the next several years should provide the necessary sensitivity to observe this type of radiation. LIGO and other gravitational wave interferometers operate at the forefront of laser and optics technology, which enables the extraordinarily sensitive measurements of interferometer arm length changes caused by the gravitational waves. In the future, these instruments will permit regular observations of astronomical gravitational waves.

As routine observations of gravitational waves become a reality, the scientific value of interferometers improves if the uncertainties in the detector strain calibration can be reduced to the level of 1%. A key part of the calibration is characterizing the differential-arm length control actuators. Two new actuation calibration procedures have now been developed: the laser frequency modulation technique and photon calibrator method, both of which have calibration uncertainties of $\sim$1%. This is a significant improvement over the traditional actuation calibration technique which

has been the dominant source of detector strain calibration uncertainty in each of the initial LIGO science runs. Additionally, the photon calibrator method can monitor the interferometer response function continuously in the science-mode configuration without the requirement of first characterizing the arm length control actuators in different optical and electronics configurations.

These two new methods have been used to characterize the arm length control actuators and compared with the traditional actuator calibration technique to investigate systematic uncertainties of the three methods. The mean value of the results of each technique from 90 Hz to 1 kHz agree within 2.4% (1σ), well within the uncertainty of the traditional calibration method. In the future, detector calibrations will rely on many techniques to reduce systematic uncertainties. The photon calibrator and the frequency modulation method will continue to play an important role in these efforts.

One class of astrophysical sources of gravitational waves are neutron stars emitting quasi-monochromatic gravitational waves. Observing a gravitational wave signal from these sources (in addition to testing General Relativity) would provide a useful measurement to assist in constraining particular models of neutron star equations of state. A number of searches for particular sources and all-sky searches for unknown isolated neutron stars have been undertaken over the past decade, but no previous search has been made for unknown neutron stars in binary systems. The additional search parameters of the binary system make the methods adapted from the isolated all-sky routines computationally intractable. Therefore, new analysis methods must be used in the search for unknown neutron stars in binary systems.

A new method has now been developed to search for these sources, called TwoSpect, which relies on the periodic Doppler shift of the gravitational wave frequency by the periodic velocity variation of the neutron star emitting the waves. The algorithm computes successive Fourier transformations of the detector strain data and uses a

hierarchical scheme to search the doubly Fourier-transformed data for characteristic patterns corresponding to different source frequencies, different binary orbital periods, and different amplitudes of frequency modulation. In order to make the search possible, this scheme makes the tradeoff of increased computational efficiency at the cost of reduced sensitivity to signals.

The TwoSpect algorithm is beginning to provide the first-ever results of an all-sky search for unknown neutron stars in binary systems in gravitational wave detector data. Due to the computational efficiency of this method, it allows searching a previously unexplored region of parameter space for spinning neutron stars. This method will start to analyze data near the end of 2010 using detector data from the recent science runs of the LIGO and Virgo interferometers.

BIBLIOGRAPHY

BIBLIOGRAPHY

[1] J. Abadie et al. All-sky search for gravitational-wave bursts in the first joint LIGO-GEO-Virgo run. *Phys. Rev. D*, 81(10):102001, May 2010.

[2] J. Abadie et al. Predictions for the rates of compact binary coalescences observable by ground-based gravitational-wave detectors. *Classical and Quantum Gravity*, 27(17):173001, 2010.

[3] B. Abbott et al. Setting upper limits on the strength of periodic gravitational waves from PSR J1939+2134 using the first science data from the GEO 600 and LIGO detectors. *Phys. Rev. D*, 69(8):082004, Apr 2004.

[4] B. Abbott et al. First all-sky upper limits from LIGO on the strength of periodic gravitational waves using the hough transform. *Phys. Rev. D*, 72(10):102004, Nov 2005.

[5] B. Abbott et al. Limits on Gravitational-Wave Emission from Selected Pulsars Using LIGO Data. *Phys. Rev. Lett.*, 94(18):181103, May 2005.

[6] B. Abbott et al. Searches for periodic gravitational waves from unknown isolated sources and Scorpius X-1: Results from the second LIGO science run. *Phys. Rev. D*, 76(8):082001, 2007.

[7] B. Abbott et al. Upper limits on gravitational wave emission from 78 radio pulsars. *Phys. Rev. D*, 76(4):042001, Aug 2007.

[8] B. Abbott et al. All-sky search for periodic gravitational waves in LIGO S4 data. *Phys. Rev. D*, 77(2):022001, Jan 2008.

[9] B. Abbott et al. Beating the spin-down limit on gravitational wave emission from the crab pulsar. *The Astrophysical Journal Letters*, 683(1):L45, 2008.

[10] B. Abbott et al. Einstein@Home search for periodic gravitational waves in LIGO S4 data. *Phys. Rev. D*, 79(2):022001, Jan 2009.

[11] B. P. Abbott et al. All-Sky LIGO Search for Periodic Gravitational Waves in the Early Fifth-Science-Run Data. *Phys. Rev. Lett.*, 102(11):111102, Mar 2009.

[12] B. P. Abbott et al. Einstein@Home search for periodic gravitational waves in early S5 LIGO data. *Phys. Rev. D*, 80(4):042003, Aug 2009.

[13] B. P. Abbott et al. LIGO: the Laser Interferometer Gravitational-Wave Observatory. *Reports on Progress in Physics*, 72(7):076901, 2009.

[14] B. P. Abbott et al. Search for gravitational waves from low mass compact binary coalescence in 186 days of LIGO's fifth science run. *Phys. Rev. D*, 80(4):047101, Aug 2009.

[15] B. P. Abbott et al. Searches for gravitational waves from known pulsars with science run 5 LIGO data. *The Astrophysical Journal*, 713(1):671, 2010.

[16] F. Acernese et al. The Virgo status. *Classical and Quantum Gravity*, 23(19):S635, 2006.

[17] R. Adhikari, P. Fritschel, and S. Waldman. Enhanced LIGO. Technical Report T060156, LIGO, 2006.

[18] R. Adhikari, G. González, M. Landry, and B. O'Reilly (for the LIGO Scientific-Collaboration). Calibration of the LIGO detectors for the first LIGO science run. *Classical and Quantum Gravity*, 20(17):S903, 2003.

[19] M. Afrin Badhan, M. Landry, R. Savage, and P. Willems. Analyzing elastic deformation of test masses in LIGO. Technical Report T0900401, LIGO, 2009.

[20] Y. Aso, E. Goetz, P. Kalmus, L. Matone, S. Márka, J. Myers, B. O'Reilly, R. Savage, P. Schwinberg, X. Siemens, D. Sigg, and N. Smith. Accurate measurement of the time delay in the response of the LIGO gravitational wave detectors. *Classical and Quantum Gravity*, 26(5):055010, 2009.

[21] W. Becker, editor. *Neutron Stars and Pulsars*. Springer-Verlag, 2009.

[22] L. Bildsten. Gravitational Radiation and Rotation of Accreting Neutron Stars. *The Astrophysical Journal Letters*, 501(1):L89, 1998.

[23] J. Bruursema. Calibration of the LIGO interferometer using the recoil of photons. Technical Report T030266, LIGO, 2003.

[24] S. M. Carroll. *Spacetime and Geometry*. Addison Wesley, 2004.

[25] D. A. Clubley, G. P. Newton, K. D. Skeldon, and J. Hough. Calibration of the glasgow 10 m prototype laser interferometric gravitational wave detector using photon pressure. *Physics Letters A*, 283(1-2):85–88, 2001.

[26] LIGO Scientific Collaboration. LALApps repository. www.lsc-group.phys.uwm.edu/daswg/.

[27] The LIGO Scientific Collaboration and The Virgo Collaboration. An upper limit on the stochastic gravitational-wave background of cosmological origin. *Nature*, 460:990–4, Aug 2009.

[28] R. B. Davies. Numerical inversion of a characteristic function. *Biometrika*, 60(2):415–17, August 1973.

[29] R. B. Davies. Algorithm as 155: The distribution of a linear combination of χ^2 random variables. *Applied Statistics*, 29(3):323–33, 1980.

[30] S. V. Dhurandhar and A. Vecchio. Searching for continuous gravitational wave sources in binary systems. *Phys. Rev. D*, 63(12):122001, May 2001.

[31] R. W. P. Drever, J. L. Hall, F. V. Kowalski, J. Hough, G. M. Ford, A. J. Munley, and H. Ward. Laser phase and frequency stabilization using an optical resonator. *Applied Physics B: Lasers and Optics*, 31(2):97–105, June 1983.

[32] S. Erickson. Investigation of variations in the absolute calibration of the laser power sensors for the LIGO photon calibrators. Technical Report T080316, LIGO, 2008.

[33] J. Gil-Pelaez. Note on the inversion theorem. *Biometrika*, 38(3-4):481–482, 1951.

[34] E. Goetz. Commissioning of the photon calibrators. Technical Report T040196, LIGO, 2004.

[35] E. Goetz and R. L. Savage Jr. Calibration of the LIGO displacement actuators via laser frequency modulation. arXiv:1005.3746v2 [gr-qc], July 2010.

[36] E. Goetz, R. L. Savage Jr., J. Garofoli, G. Gonzalez, E. Hirose, P. Kalmus, K. Kawabe, J. Kissel, M. Landry, B. O'Reilly, X. Siemens, A. Stuver, and M. Sung. Accurate calibration of test mass displacement in the LIGO interferometers. *Classical and Quantum Gravity*, 27(8):084024, 2010.

[37] E. Goetz, P. Kalmus, S. Erickson, R. L. Savage Jr., G. Gonzalez, K. Kawabe, M. Landry, S. Marka, B. O'Reilly, K. Riles, D. Sigg, and P. Willems. Precise calibration of LIGO test mass actuators using photon radiation pressure. *Classical and Quantum Gravity*, 26(24):245011, 2009.

[38] J. Hadler et al. NIST report of calibration 42110ca/42111ca. Technical Report T070245, LIGO, 2007.

[39] G. M. Harry and The LIGO Scientific Collaboration. Advanced LIGO: the next generation of gravitational wave detectors. *Classical and Quantum Gravity*, 27(8):084006, 2010.

[40] Y. Hefetz, N. Mavalvala, and D. Sigg. Principles of calculating alignment signals in complex resonant optical interferometers. *J. Opt. Soc. Am. B*, 14(7):1597–1605, 1997.

[41] S. Hild. *Beyond the first generation: extending the science range of the gravitational wave detector GEO 600*. PhD thesis, University of Hannover, 2007.

[42] S. Hild, M. Brinkmann, K. Danzmann, H. Grote, M. Hewitson, J. Hough, H. Lück, I. Martin, K. Mossavi, N. Rainer, S. Reid, J. R. Smith, K. Strain, M. Weinert, P. Willems, B. Willke, and W Winkler. Photon-pressure-induced test mass deformation in gravitational-wave detectors. *Classical and Quantum Gravity*, 24(22):5681, 2007.

[43] C. J. Horowitz and K. Kadau. Breaking strain of neutron star crust and gravitational waves. *Phys. Rev. Lett.*, 102(19):191102, May 2009.

[44] J. P. Imhof. Computing the distribution of quadratic forms in normal variables. *Biometrika*, 48(3/4):419–26, December 1961.

[45] J. D. Jackson. *Classical Electrodynamics*. John Wiley & Sons, Inc., third edition, 1999.

[46] P. Jaranowski, A. Królak, and B. F. Schutz. Data analysis of gravitational-wave signals from spinning neutron stars: The signal and its detection. *Phys. Rev. D*, 58(6):063001, Aug 1998.

[47] D. I. Jones and N. Anderson. Gravitational waves from freely precessing neutron stars. *Mon. Not. R. Astron. Soc.*, 331:203–220, 2002.

[48] R. L. Savage Jr., P. J. King, and S. U. Seel. A Highly Stabilized 10-Watt Nd:YAG Laser for the Laser Interferometer Gravitational Wave Observatory (LIGO). Technical Report P980002, LIGO, 1998.

[49] J. Kissel et al. Calibration of the LIGO instruments for the fifth science run. Technical Report P0900120, LIGO, 2009.

[50] M. Landry and The LIGO Scientific Collaboration. Improvements in strain calibration for the third LIGO science run. *Classical and Quantum Gravity*, 22(18):S985, 2005.

[51] J. M. Lattimer and M. Prakash. The Physics of Neutron Stars. *Science*, 304(5670):536–542, 2004.

[52] L. Lindblom. Optimal calibration accuracy for gravitational-wave detectors. *Phys. Rev. D*, 80(4):042005, Aug 2009.

[53] D. R. Lorimer. Binary and Millisecond Pulsars. *Living Rev. Relativity*, 11(8), 2008. cited 11 Aug 2010.

[54] H. Lück et al. Status of the GEO600 detector. *Classical and Quantum Gravity*, 23(8):S71, 2006.

[55] M. Maggiore. *Gravitational Waves*, volume 1. Oxford University Press, 2008.

[56] R. N. Manchester, G. B. Hobbs, A. Teoh, and M. Hobbs. The Australia Telescope National Facility Pulsar Catalogue. *The Astronomical Journal*, 129(4):1993, 2005.

[57] L. Matone, P. Raffai, S. Márka, R. Grossman, P. Kalmus, Z. Márka, J. Rollins, and V. Sannibale. Benefits of artificially generated gravity gradients for interferometric gravitational-wave detectors. *Classical and Quantum Gravity*, 24(9):2217, 2007.

[58] C. Messenger and G. Woan. A fast search strategy for gravitational waves from low-mass x-ray binaries. *Classical and Quantum Gravity*, 24:S469, October 2007.

[59] S. D. Mohanty. Median based line tracker (MBLT): model independent and transient preserving line removal from interferometric data. *Classical and Quantum Gravity*, 19(7):1513, 2002.

[60] S. D. Mohanty and S. Mukherjee. Towards a data and detector characterization robot for gravitational wave detectors. *Classical and Quantum Gravity*, 19(7):1471, 2002.

[61] E. Morrison, B. J. Meers, D. I. Robertson, and H. Ward. Automatic alignment of optical interferometers. *Appl. Opt.*, 33(22):5041–5049, 1994.

[62] K. Mossavi, M. Hewitson, S. Hild, F. Seifert, U. Weiland, J.R. Smith, H. Lück, H. Grote, B. Willke, and K. Danzmann. A photon pressure calibrator for the GEO 600 gravitational wave detector. *Physics Letters A*, 353(1):1–3, 2006.

[63] B. J. Owen. Maximum Elastic Deformations of Compact Stars with Exotic Equations of State. *Phys. Rev. Lett.*, 95:211101, November 2005.

[64] B. J. Owen. Detectability of periodic gravitational waves by initial interferometers. *Classical and Quantum Gravity*, 23:S1–S7, 2006.

[65] B. J. Owen. How to adapt broad-band gravitational-wave searches for r-modes. arXiv:1006.1994v1 [gr-qc], June 2010.

[66] B. J. Owen, L. Lindblom, C. Cutler, B. F. Schutz, A. Vecchio, and N. Andersson. Gravitational waves from hot young rapidly rotating neutron stars. *Phys. Rev. D*, 58(8):084020, Sep 1998.

[67] J. Papaloizou and J. E. Pringle. Non-radial oscillations of rotating stars and their relevance to the short-period oscillations of cataclysmic variables. *Monthly Newsletter of the Royal Astronomical Society*, 182:423–442, February 1978.

[68] P.M. Saz Parkinson et al. Eight gamma-ray pulsars discovered in blind frequency searches of Fermi LAT data. arXiv:1006.2134v1 [astro-ph.HE], 2010.

[69] M. Rakhmanov. *Dynamics of Laser Interferometric Gravitational Wave Detectors*. PhD thesis, California Institute of Technology, 2000.

[70] M. Rakhmanov, R. L. Savage, D. H. Reitze, and D. B. Tanner. Dynamic resonance of light in Fabry-Perot cavities. *Physics Letters A*, 305(5):239–244, 2002.

[71] S. M. Ransom, J. M. Cordes, and S. S. Eikenberry. A New Search Technique for Short Orbital Period Binary Pulsars. *The Astrophysical Journal*, 589:911–920, June 2003.

[72] S. M. Ransom, S. S. Eikenberry, and J. Middleditch. Fourier techniques for very long astrophysical time-series analysis. *The Astronomical Journal*, 124(3):1788, 2002.

[73] K. U. Ratnatunga and S. van den Bergh. The rate of stellar collapses in the galaxy. *The Astrophysical Journal*, 343:713–717, August 1989.

[74] M. W. Regehr, F. J. Raab, and S. E. Whitcomb. Demonstration of a power-recycled Michelson interferometer with Fabry–Perot arms by frontal modulation. *Opt. Lett.*, 20(13):1507–1509, 1995.

[75] L. Rolland, F. Marion, and B. Mours. Use of photon calibrators for the VSR1 calibration. Technical Report VIR-053A-08, VIRGO, 2008.

[76] D. Sigg. Strain calibration in LIGO. Technical Report T970101, LIGO, 1997.

[77] R. Takahashi and the TAMA Collaboration. Status of TAMA300. *Classical and Quantum Gravity*, 21(5):S403, 2004.

[78] R. V. Wagoner. Gravitational radiation from accreting neutron stars. *The Astrophysical Journal*, 278:345–348, March 1984.

[79] J. M. Weisberg and J. H. Taylor. Relativistic Binary Pulsar B1913+16: Thirty Years of Observations and Analysis. arXiv:astro-ph/0407149v1, July 2004.

[80] P. Willems. Finite element modeling of test mass flexure due to OSEM forces. Technical Report T080190, LIGO, 2008.